

SYNTHESIS OF SIALON CERAMICS WITH MOLECULAR  
PRECURSORS AS ADDITIVES

BY  
KADE A. MCGARRITY

A THESIS  
SUBMITTED TO THE FACULTY OF  
ALFRED UNIVERSITY

IN PARTIAL FULFILLMENT OF THE REQUIREMENTS  
FOR THE DEGREE OF

DOCTOR OF PHILOSOPHY

IN  
MATERIALS SCIENCE AND ENGINEERING

ALFRED, NEW YORK

MAY, 2022

SYNTHESIS OF SIALON CERAMICS WITH MOLECULAR  
PRECURSORS AS ADDITIVES

BY

KADE A. MCGARRITY

B.S. ALFRED UNIVERSITY (2017)

SIGNATURE OF AUTHOR\_\_\_\_\_

APPROVED BY\_\_\_\_\_  
DR. HOLLY SHULMAN, ADVISOR

DR. SCOTT MISTURE, ADVISORY COMMITTEE

DR. KUN WANG, ADVISORY COMMITTEE

DR. JUNJUN DING, ADVISORY COMMITTEE

DR. ALEXIS CLARE, CHAIR, ORAL THESIS DEFENSE

ACCEPTED BY\_\_\_\_\_  
DR. GABRIELLE G. GAUSTAD , DEAN  
KAZUO INAMORI SCHOOL OF ENGINEERING

ACCEPTED BY\_\_\_\_\_  
DR. BETH ANN DOBIE  
PROVOST AND VP FOR ACADEMIC AFFAIRS  
ALFRED UNIVERSITY

Alfred University theses are copyright protected and may be used for education or personal research only. Reproduction or distribution in part or whole is prohibited without written permission from the author.

Signature page may be viewed at Scholes Library,  
New York State College of Ceramics, Alfred University,  
Alfred, New York.

## ACKNOWLEDGMENTS

The work reported herein took place over the course of four and a half years, and for the majority of that time, I never felt truly confident in my ability to complete it. It therefore fell to those around whom I've woven my life to, wittingly or otherwise, lend the unique blend of support, vision, criticism, and sense of purpose that propels one inexorably down an uncertain path. It is futile to show sufficient appreciation. Nevertheless, I will attempt to express my sincere gratitude and trust the reader to translate these words into the fervent sentiment which begot them.

I must first thank my advisor and mentor, Dr. Holly Shulman, who in addition to her many skills and talents exhibits an almost supernatural gift for ideation. The level of trust and responsibility she afforded me during these years terrified me at times and gave me no choice but to be the best version of myself. She is truly invested in creating an atmosphere of support, accountability, and creativity for all her students, and I would certainly be a completely different scientist and person today if not for her guidance.

I must also thank my thesis committee for their insightful discussions and expertise. Dr. Scott Misture provided crucial guidance in the area of X-ray diffraction. Dr. Junjun Ding forced me to be rigorously critical of my work. Dr. Kun Wang, in addition to performing high-resolution electron microscopy and diffraction, displayed a heartening willingness to participate in the realization of this thesis.

I am compelled to express gratitude to Dr. Steven Pilgrim for his support, availability, discussion, and experience throughout this thesis. Dr. Christy George of the Eberly College of Science at Penn State performed and provided valuable insight into the nuclear magnetic resonance experiments expounded upon within. Professor George Quinn of NIST provided valuable expertise and guidance in fractography.

I am deeply grateful to those who seem to have the “magic touch” which keeps every lab on this campus operational. Mr. Fran Williams vaulted each of the myriad of obstacles presented by the hot press with determination. Mr. Jim Thiebaud enthusiastically explored any experimental avenue I could think of. Mr. Dave Greene found a solution for machining my specimens without which my data would have remained locked behind a hard, useless surface.

Finally, I am grateful to my family, who have supported me in moments of doubt and apprehension and were one of the only constants in the past years, and to my friends, who have shared in many of my triumphs, disappointments, and experiences.

The earlier portion of this research was supported by the Empire Innovation Professorship Award granted to Dr. Shulman. The Bernstein Family generously supported some of the most impactful experiences of my academic career by helping to fund travel. Part of this material is based upon work performed on a Raman spectrometer which was supported by the National Science Foundation under Grant No. DMR-1626164. Specimens were prepared for TEM using a FIB which was funded by the NSF under grant 2018306.

# TABLE OF CONTENTS

	<b>Page</b>
<i>Acknowledgments</i> .....	<i>iii</i>
<i>Table of Contents</i> .....	<i>iv</i>
<i>List of Tables</i> .....	<i>vi</i>
<i>List of Figures</i> .....	<i>vii</i>
<i>Abstract</i> .....	<i>xvi</i>
<b>I. INTRODUCTION</b>	<b>1</b>
A. MOTIVATION AND OPPORTUNITY FOR SiAlON CERAMICS .....	1
1. <i>Current internal combustion engine materials</i> .....	2
2. <i>Current structural biomaterials</i> .....	3
B. BACKGROUND ON SILICON NITRIDE .....	5
1. <i>Crystallography of <math>Si_3N_4</math></i> .....	6
2. <i>Sintering, additives, and phase compatibility</i> .....	9
3. <i>Minor SiAlON polytypoids</i> .....	12
4. <i>The role of Al and O in SiAlONs</i> .....	13
5. <i>Effect of additives on SiAlON structural properties</i> .....	14
C. MOLECULAR PRECURSORS TO CERAMICS .....	15
1. <i>Sol-gel synthesis of <math>SiO_2</math> and <math>Al_2O_3</math></i> .....	16
D. SILICON CARBONITRIDE/SILICOBORON CARBONITRIDE/TURBOSTRATIC BN BACKGROUND.....	18
1. <i>Structures of <math>SiCN</math> and <math>SiBCN</math></i> .....	19
2. <i>Thermal decomposition of <math>Si(B)CN</math></i> .....	20
3. <i>The role of BN in <math>SiBCN</math> and other systems</i> .....	20
E. SILICON NITRIDE/BORON NITRIDE POLYCRYSTALLINE NANOCOMPOSITES.....	21
F. THE FRACTOGRAPHIC PROCEDURE.....	22
1. <i>Quantitative fractography and <math>K_{IC}</math></i> .....	24
<b>II. MOLECULAR-LEVEL SINTERING ADDITIVES FOR SYNTHESIS OF OF SiAlON CERAMICS</b>	<b>27</b>
A. INTRODUCTION.....	27
B. MATERIALS AND METHODS.....	28
C. RESULTS AND DISCUSSION .....	32
D. CONCLUSIONS .....	47
<b>III. EXPLORATION OF AN ATOMIC-SCALE BORON ADDITIVE IN SiAlON CERAMICS</b>	<b>49</b>

A.	INTRODUCTION.....	49
B.	MATERIALS AND METHODS.....	50
C.	RESULTS AND DISCUSSION .....	53
D.	CONCLUSIONS .....	66
<b>IV.</b>	<b>FRACTOGRAPHY OF SILICON NITRIDE BASED CERAMICS TO GUIDE PROCESS IMPROVEMENTS</b>	<b>68</b>
A.	INTRODUCTION.....	68
1.	<i>Mathematical treatment of fracture</i> .....	68
2.	<i>Fracture markings</i> .....	72
B.	MATERIALS AND METHODS.....	74
1.	<i>Fractographic procedure</i> .....	76
C.	RESULTS AND DISCUSSION .....	78
D.	CONCLUSIONS .....	89
<b>V.</b>	<b>SUMMARY AND CONCLUSIONS</b>	<b>91</b>
<b>VI.</b>	<b>RECOMMENDATIONS FOR FUTURE WORK</b>	<b>93</b>
<b>VII.</b>	<b>REFERENCES</b>	<b>94</b>
<b>VIII.</b>	<b>APPENDICES</b>	<b>103</b>
A.	RIETVELD REFINEMENT RESULTS .....	103
B.	BEAM THEORY APPROACH TO STRESS AND STRAIN .....	110
C.	PROCEDURE FOR CONVERSION OF LOAD/DISPLACEMENT RAW DATA TO A STRESS/STRAIN CURVE .....	117

## LIST OF TABLES

	<b>Page</b>
Table I. SiAlON Starting Material Specifications (- indicates not reported or applicable).....	29
Table II. SiAlON Powder Blend Compositions with Raw Materials in wt%. Note: ASB denotes aluminum tri <i>sec</i> -butoxide, an Al alkoxide.....	30
Table III. SiAlON Powder Blend Compositions for Boron Incorporation (wt%).....	50
Table IV. SiAlON Powder Blend Compositions for Fractographic Studies with Raw Materials in wt% .....	75
Table V. Maximum failure stresses ( $\sigma$ ), stresses at fracture origins ( $\sigma_f$ ), measured mirror radii (r), calculated mirror constants (A), flaw sizes (c), geometric constants (Y), and toughness ( $K_{IC}$ ) values for samples, wherever possible, from different compositional blends. (NI: Not identifiable) .....	87

## LIST OF FIGURES

	Page
Figure 1. Typical $\text{Si}_3\text{N}_4$ microstructure, wherein long rod-like grains are embedded in a fine-grained matrix. <sup>42</sup> .....	7
Figure 2. $\alpha\text{-Si}_3\text{N}_4$ crystal structure. White lines indicate the unit cell. ....	8
Figure 3. $\beta\text{-Si}_3\text{N}_4$ crystal structure. White lines indicate the unit cell. ....	9
Figure 4. Phase equilibrium diagrams for the $\text{Y}_2\text{O}_3\text{-Al}_2\text{O}_3\text{-SiO}_2$ system at 1300 °C and 1400 °C. Note that a melt forms between these temperatures. Adapted from Kolitsch, <i>et al.</i> , (1999). <sup>52</sup> .....	10
Figure 5. Schematic compositional pyramid for the Si-Al-O-N system. Note that the common starting materials for the synthesis of SiAlONs - $\text{Si}_3\text{N}_4$ , 4(AlN), 2( $\text{Al}_2\text{O}_3$ ), and 3( $\text{SiO}_2$ ) - can be found along four of the edges of the pyramid. ....	11
Figure 6. SiAlON phase diagram, highlighting many SiAlON polytypes.....	11
Figure 7. Jänecke prism summarizing the phase compatibility of the SiAlON system with YN and $\text{Y}_2\text{O}_3$ . ....	12
Figure 8. Molecular structure of tetraethyl orthosilicate (TEOS).....	17
Figure 9. Molecular structure of aluminum tri <i>sec</i> -butoxide (ASB).....	17
Figure 10. Thermogravimetric behavior of SiBCN in comparison to $\text{Si}_3\text{N}_4$ and $\text{SiCN}$ . <sup>93</sup> .....	18
Figure 11. SiBCN nanostructure, highlighting the interfacial region between Si-N tetrahedral domain and layered C/BN domain. Chemical domains are on the order of nanometers. ★-exclusive interfacial tetrahedron. ●-mixed interfacial tetrahedron. ....	20
Figure 12. A general fractographic procedure for a SiAlON flexure specimen, including observation with the naked eye, optical microscopy, electron microscopy, and chemical analysis of the fracture origin (in this case, an inclusion, likely stainless steel).....	23

Figure 13. Schematic of a specimen with a large hole or flaw, subjected to a uniaxial tensile force. Red lines are known as stress flow lines. The schematic illustrates a concentration of stress on either side of the hole.....	24
Figure 14. 1-inch inner diameter graphite die used for uniaxial hot pressing. Dies were lined with graphite foil of 0.005 inch thickness which was spray coated with aerosolized hexagonal boron nitride.....	31
Figure 15. SEM micrographs of a) Al organometallic-containing SiAlON powder blend (0YASB and b) conventional Al <sub>2</sub> O <sub>3</sub> -containing SiAlON powder blend (0YAl <sub>2</sub> O <sub>3</sub> ) with corresponding measured BET specific surface areas. ....	34
Figure 16. SEM micrographs of a) organometallic-containing powder blend (0YASB), and b) conventional Al <sub>2</sub> O <sub>3</sub> -containing powder blend (0YAl <sub>2</sub> O <sub>3</sub> ) after heat treatment. Decomposition of the ASB organometallic reveals discernable particles. ....	35
Figure 17. TGA mass loss curves comparing SiAlON blends containing alumina powder (0YAl <sub>2</sub> O <sub>3</sub> ) and Al alkoxide additive (0YASB). The mass loss of the alumina-containing blend was <1 wt% on heating to 1000 °C, while the ASB-containing blend lost 6.7 wt% mass.....	36
Figure 18. TGA/DTA curves for Al alkoxide additive SiAlON powder blend (0YASB). DTA reveals a broad endothermic region between 20 and ~300 °C, attributed to volatilization of organic species and moisture. No exotherms detected (indicating no crystallization). ....	37
Figure 19. Aluminum EDS maps comparing SiAlON blends containing a) alumina powder (0YAl <sub>2</sub> O <sub>3</sub> ) with b) Al alkoxide additive (0YASB). The alumina-containing powder blend exhibits regions of high Al concentration, attributed to Al <sub>2</sub> O <sub>3</sub> particles; ASB-containing blend exhibits a significantly more homogeneous distribution of Al.....	38
Figure 20. Aluminum EDS map of SiAlON powder blend with Al alkoxide (0YASB) heat treated to 1000 °C for 1 h in flowing UHP N <sub>2</sub> . The distribution of Al appears to remain homogeneous even after the decomposition of the organic precursor.....	39
Figure 21. Secondary electron micrographs of 0YASB at a) room temperature, b) 500 °C, and c) room temperature after cooling from 500 °C. No morphological differences were detected, indicating the lack of widespread Al <sub>2</sub> O <sub>3</sub> crystallization of the ASB on heating to 500 °C.....	40

Figure 22. XRD Patterns of 0YASB powder as-blended, after heating to 500 °C in a vacuum, and after heating to 1000 °C in flowing nitrogen. *: ZrO <sub>2</sub> (PDF 01-079-1763) #: AlN (PDF 00-066-0534) Unlabeled peaks: α-Si <sub>3</sub> N <sub>4</sub> (PDF 04-001-1514).....	41
Figure 23. XRD Slow scan of 0YASB after heat treatment to 500 °C in a vacuum in search of evidence of γ-Al <sub>2</sub> O <sub>3</sub> . No peak at 42.5 °2θ was observed, indicating that this transition alumina is not present in detectable volumes.....	42
Figure 24. Immersion densities of sintered SiAlONs. At 4 wt% Y <sub>2</sub> O <sub>3</sub> , samples converge to the same density. When the Y <sub>2</sub> O <sub>3</sub> concentration is decreased, the ASB sample exhibits a higher density. Error bars represent the statistical uncertainty of the measurement technique, based on the resolution of the instruments used and the number of measurements performed.....	43
Figure 25. Unit cell volumes of β'-SiAlONs sintered with 4 wt% Y <sub>2</sub> O <sub>3</sub> for various dwell times. Unit cell volumes are greater in SiAlONs sintered using ASB than those sintered with Al <sub>2</sub> O <sub>3</sub> , indicating enhanced solid solution of Al and O in the Si <sub>3</sub> N <sub>4</sub> lattice.....	44
Figure 26. Unit cell volumes of ASB- and Al <sub>2</sub> O <sub>3</sub> -containing SiAlONs at 4 wt% Y <sub>2</sub> O <sub>3</sub> (common concentration) and 2 wt% Y <sub>2</sub> O <sub>3</sub> (very low concentration). ASB SiAlONs exhibit higher unit cell volumes for both concentrations. SiAlON unit cell volume decreases with increasing liquid phase additive concentration.....	45
Figure 27. a and c lattice parameters for β'-SiAlON as a function of Y <sub>2</sub> O <sub>3</sub> concentration. Filled and open circles are SiAlONs from the present work, derived from Al <sub>3</sub> O <sub>3</sub> powder and ASB, respectively, while the diamonds correspond to the SiAlONs synthesized by Ekström, <i>et al.</i> <sup>69</sup> Black data points correspond to a lattice parameters, and purple points correspond to c lattice parameters.....	46
Figure 28. Elastic moduli of sintered SiAlONs, showing no statistically significant difference as a function of both Y <sub>2</sub> O <sub>3</sub> concentration and presence of Al <sub>2</sub> O <sub>3</sub> or ASB. Error bars represent the statistical uncertainty of the measurement technique, based on the resolution of the instruments used and the number of measurements performed.....	47
Figure 29. SiAlON sintering profile.....	51

Figure 30. Immersion densities of SiAlONs with increasing boron concentration. Lower-boron SiAlONs B0, B1, B2, and B3. B0-B2 exhibited comparable and high densities, while the 3 wt% H <sub>3</sub> BO <sub>3</sub> -containing SiAlON blend achieved a lower density. Error bars represent the statistical uncertainty of the measurement technique, based on the resolution of the instruments used and the number of measurements performed.....	53
Figure 31. XRD patterns of boron-containing SiAlONs B0-3. Residual α-Si <sub>3</sub> N <sub>4</sub> and other miscellaneous second phase peaks are found in the boron-free SiAlON and show a reduction in intensity until a single-phase β'-SiAlON was achieved in B3. α denotes α-Si <sub>3</sub> N <sub>4</sub> (PDF card 04-001-1514), * denotes Y <sub>10</sub> Si <sub>3</sub> Al <sub>2</sub> O <sub>18</sub> N <sub>4</sub> (PDF card 00-032-1426), # denotes Y <sub>2</sub> AlSiNO <sub>5</sub> (PD card 04-012-5019), and unlabeled peaks are β'-SiAlON (PDF card 04-007-0791). ..	54
Figure 32. Schematic of the in-plane E <sub>2g</sub> symmetric vibrational mode of t-BN and h-BN, which gives rise to a Raman peak at ~1370 cm <sup>-1</sup> .....	55
Figure 33. Raman spectra of boron-containing SiAlONs B0-B3. The peak at approximately 1370 cm <sup>-1</sup> provides evidence of t-BN. Note the peaks related to residual α-Si <sub>3</sub> N <sub>4</sub> in SiAlONs with lower concentration of boron, which disappear with higher dopant concentrations and are consistent with XRD analysis. The inset displays the 1 wt% H <sub>3</sub> BO <sub>3</sub> SiAlON spectrum in the range of 1300 – 1400 cm <sup>-1</sup> . It is evident that a small t-BN peak begins to appear at this dopant level.....	56
Figure 34. <sup>11</sup> B SS MAS-NMR spectrum of boron-rich SiAlON B3, indicating boron in threefold coordination with nitrogen (B[III]). .....	58
Figure 35. Micrographs of etched surfaces of a) a zero-boron SiAlON B0 and b) the most boron-rich SiAlON B3, with random lines drawn for grain size analysis. The imaging plane is perpendicular to the hot pressing direction. ....	59
Figure 36. Average grain sizes of boron-containing SiAlONs B0-B3, indicating comparable grain sizes but reduced standard deviation of grain size. Error bars represent 1 standard deviation. ....	60
Figure 37. Grain size distributions of the four SiAlONs of varying boron concentration, indicating that the distributions become narrower with increasing boron concentration. Each line in the “rug” section on the bottom of the plot indicates a single measurement. ....	61

Figure 38. EDS elemental maps from TEM analysis of the grain boundary region of the high-boron SiAlON B3, showing a grain interior rich in Si and N, with minor concentration of Al and O, and an intergranular glass rich in Y and O, with minor concentration of Si and N. Y does not seem to have entered the $\text{Si}_3\text{N}_4$ lattice. Boron may have a preference for the grain boundary, but low EDS signal makes this difficult to conclude.....	62
Figure 39. Unit cell volumes of $\beta'$ -SiAlON as a function of boron concentration, revealing little to no effect.....	63
Figure 40. Transmission electron micrograph of the grain boundary region of boron-rich SiAlON B3. Accompanying convergent beam electron diffraction (CBED) patterns indicate that grain interiors (dark regions) are crystalline while the intergranular phase (lighter region) is amorphous.....	64
Figure 41. High-magnification STEM image of the grain boundary region of boron-rich SiAlON B3, wherein the lighter region is the matrix crystal phase and the darker region is the glass phase near the grain boundary. The micrograph indicates that the crystal phase is well-ordered throughout, and an amorphous-to-crystalline transitional region is not present between the matrix crystals and the grain boundary.....	64
Figure 42. Hardness and indentation crack resistance of SiAlONs as a function of boron concentration. Hardness decreases linearly with increasing boron content. ICR does not show any strong trend, but B0 appears to exhibit a slightly higher value. Hardness error bars indicate the statistical uncertainty of the measurement technique. ICR error bars indicate standard deviation of the measurements.....	65
Figure 43. Schematic representation of the stresses developed throughout the cross section of a bar in flexure. Maximum compressive stress is located on top, maximum tensile stress on the bottom, and zero stress develops in the center, or neutral axis.....	69
Figure 44. Finite element analysis of a bar in a) three-point bending geometry and b) four point bending geometry. In three-point bending, maximum stress is concentrated at a single point directly below the loading point. In four point bending, a uniform maximum stress region is evolved between the loading points. FEA performed in MOOSE software (Idaho National Laboratory, USA), results visualized in ParaView (Kitware, USA).....	72

Figure 45. Schematics of low-, medium-, and high-energy fracture paths. Arrows indicate fracture origins. Adapted from “Fractography of Ceramics and Glasses”, by George Quinn, Third Edition. <sup>7</sup> Republished courtesy of the National Institute for Standards and Technology.....	73
Figure 46. Some common fracture markings from a brittle fracture. Adapted from “Fractography of Ceramics and Glasses”, Third Edition, by George Quinn. <sup>7</sup> Republished courtesy of the National Institute for Standards and Technology.....	74
Figure 47. Experimental setup for four point ¼-pt flexure experiments. ....	77
Figure 48. Immersion densities of ASB- and Al <sub>2</sub> O <sub>3</sub> -containing SiAlONs with varying boron concentrations. All SiAlONs exhibited high densities, but the lowest density SiAlON was ASB-B3, the most boron-rich ASB-route SiAlON. Error bars represent the statistical uncertainty of the measurement technique. .....	78
Figure 49. Flexural strengths of SiAlONs fabricated using both ASB and Al <sub>2</sub> O <sub>3</sub> . ASB-B3, the most boron-rich SiAlON, exhibited superior flexural strengths to the other SiAlONs fractured. Error bars represent one standard deviation of fracture stress. ....	79
Figure 50. Stress-strain curves for SiAlONs synthesized by either ASB or Al <sub>2</sub> O <sub>3</sub> powder and containing various amounts of boron; a) ASB-B0, b) ASB-B1, c) ASB-B2, d) ASB-B3, e) Al <sub>2</sub> O <sub>3</sub> -B0, and f) Al <sub>2</sub> O <sub>3</sub> -B2. Elastic modulus values are the average of the slopes of the five curves, $\pm 1$ standard deviation. ....	80
Figure 51. Correlation between elastic moduli calculated by the stress-strain curve and pulse echo techniques. Dotted lines represent an interval of $\pm 5\%$ . The pulse echo technique appears to yield slightly higher values for E.....	81
Figure 52. Selected fractured specimens of a) zero-boron SiAlON ASB-B0 (low energy fracture), b) low-boron SiAlON ASB-B1 (medium energy fracture), c) medium-boron SiAlON ASB-B2 (medium-high energy fracture), and c) boron-rich SiAlON ASB-B3 (medium-high energy fracture). Yellow circles indicate the region of crack initiation. Fracture stresses for these particular specimens is included for reference. ....	82
Figure 53. (a) SEM micrograph indicating the fracture origin and mirror boundary (dotted line) for a zero-boron SiAlON ASB-B0 specimen. (b) EDS	

showed that the critical flaw was a (Fe, Cr, Ni)-rich inclusion.	
(c) Fracture origin can also be clearly seen from the optical micrograph. ....	83
 Figure 54. Fracture origin and mirror boundary region for a zero-boron SiAlON Al <sub>2</sub> O <sub>3</sub> -B0 specimen indicated on (a) SEM and (b) optical micrographs. ....	83
 Figure 55. Fracture origin for a low-boron SiAlON ASB-B1 specimen indicated by (a) SEM and (b) optical micrographs. Mirror (dotted circle) region is relatively unclear compared to the cases with foreign inclusions as fracture origins.....	84
 Figure 56. (a) SEM micrograph indicating fracture origin and mirror boundary (dotted line) for a medium-boron SiAlON ASB-B2 specimen. (b) EDS showed that the flaw at fracture origin was an Al-rich inclusion. (c) The fracture origin can also be seen from optical microscopy.....	84
 Figure 57. (a) SEM micrograph indicating fracture origin and mirror boundary (dotted line) for a medium-boron SiAlON Al <sub>2</sub> O <sub>3</sub> -B2 specimen. (b) EDS showed that the flaw at fracture origin was Si-rich inclusion also containing carbon, possibly indicating a SiC grain. (c) Fracture origin clearly identified from optical micrograph.....	85
 Figure 58. (a) Fracture origin (surface flaw) for a high-boron SiAlON ASB-B3 specimen indicated on SEM. (b) Optical micrograph has a subtle surface crack as indicated. (c) Transillumination reveals the crack prominently.....	85
 Figure 59. Example showing measurement of fracture mirror sizes and flaw sizes for a SiAlON synthesized by the ASB route containing zero boron (ASB-B0, Sample 3). Mirror size was taken as the average of radii (R <sub>1</sub> and R <sub>2</sub> ) along the direction of approximately equivalent tensile stress. Flaw size was taken as one-half the axis length of the flaw parallel to the tensile surface for internal flaws, and flaw depth for surface flaws. ....	86
 Figure 60. Fracture stress as a function of flaw size for all samples which exhibited measurable critical flaws. All data fall between within a range defined by $1.69 < K_{IC}/Y < 5.31 \text{ MPa}\cdot\text{m}^{1/2}$ . ....	88
 Figure 61. Fracture stress as a function of mirror radius for all samples which exhibited measurable fracture mirrors. All data fall within a range defined by $6 < A < 12 \text{ MPa}\cdot\text{m}^{1/2}$ .....	89
 Figure 62. Rietveld refinement result for 4YAl <sub>2</sub> O <sub>3</sub> sintered for 60 minutes. ....	104

Figure 63. Rietveld refinement result for 4YAl <sub>2</sub> O <sub>3</sub> sintered for 10 minutes.....	104
Figure 64. Rietveld refinement result for 4YAl <sub>2</sub> O <sub>3</sub> sintered for 1 minute.....	105
Figure 65. Rietveld refinement result for 4YASB sintered for 60 minutes.....	105
Figure 66. Rietveld refinement result for 4YASB sintered for 3 minutes.....	106
Figure 67. Rietveld refinement result for 4YASB sintered for 1 minute.....	106
Figure 68. Rietveld refinement result for 2YAl <sub>2</sub> O <sub>3</sub> sintered for 60 minutes.....	107
Figure 69. Rietveld refinement result for 2YASB sintered for 60 minutes.....	107
Figure 70. Rietveld refinement result for SiAlON B0.....	108
Figure 71. Rietveld refinement result for SiAlON B1.....	108
Figure 72. Rietveld refinement result for SiAlON B2.....	109
Figure 73. Rietveld refinement result for SiAlON B3.....	109
Figure 74. Schematic of a beam in four point ¼-pt flexure. δ is the travel measured by the instrument, but the maximum deflection occurring at the center of the beam is greater than this distance.....	110
Figure 75. Free body diagram for the leftmost region of the four point ¼-pt flexure specimen.....	111
Figure 76. Free body diagram for the region between the two loading points.....	112
Figure 77. Free body diagram for the region between the rightmost loading point and support point.....	112
Figure 78. Shear diagram for four point ¼-pt flexure specimens.....	113
Figure 79. Moment diagram for four point ¼-pt flexure specimens.....	113
Figure 80. Geometry of beam bending.....	114

Figure 81. Small area of a beam in flexure, showing how axial forces induced by bending balance bending moment. ....	114
Figure 82. Machine compliance curve for the testing frame/fixture combination used in this work. The yellow region is the region over which the least-squares fit was performed. ....	118
Figure 83. 1) Slack subtraction (2) and machine compliance correction for experimental load vs displacement data. Note that the curves begin almost at the origin after slack subtraction, and the extension at fracture decreases after correction for machine compliance.....	119

## ABSTRACT

Silicon nitride ( $\text{Si}_3\text{N}_4$ ) and its related materials have been the subjects of research for 70 years and have garnered interest for applications ranging from cutting tools and bearings to turbine blades and spinal implants. The highly covalent nature of  $\text{Si}_3\text{N}_4$  lends it exceptional structural properties such as high strength and hardness, but simultaneously renders it difficult to sinter. A few techniques are employed to ameliorate this challenge. The first is the generation of a solid solution of Al and O in the  $\text{Si}_3\text{N}_4$  lattice, commonly through the use of  $\text{Al}_2\text{O}_3$  powder, thereby reducing the covalency of the system and resulting in what is known as a SiAlON. The second is the incorporation of liquid phase sintering additives which enable a dissolution-reprecipitation sintering mechanism but which reside at the grain boundary after cooling as a relatively low-temperature glass. The present work investigates the incorporation of additives, including Al and O, via molecular-level precursors in order to tailor the sintering, microstructural evolution, and resultant structural properties of SiAlON ceramics.

The first portion of this work demonstrates the incorporation of Al and O atoms with a very fine-scale homogeneous distribution via organometallic precursor aluminum tri *sec*-butoxide (ASB). A combination of chemical mapping, X-ray diffraction, thermogravimetric analysis, and differential thermal analysis was employed to investigate the pyrolytic decomposition of the organometallic precursor. Rietveld refinements were performed to assess the effectiveness of solid solution formation via the molecular precursor route to SiAlONs, in direct comparison to conventional  $\text{Al}_2\text{O}_3$  powder-derived SiAlONs. Homogeneous distribution of Al which persists to at least 1000 °C was achieved by the deposition of the organometallic precursor on starting  $\text{Si}_3\text{N}_4$  powder surfaces, with no evidence of  $\text{Al}_2\text{O}_3$  particle formation. Lattice refinements revealed that for various liquid phase concentrations and dwell times, the Al-organometallic more effectively facilitated the SiAlON solid solution than did  $\text{Al}_2\text{O}_3$  powder.

The second portion of this work investigates the incorporation of boron into the SiAlON system via precursor boric acid ( $\text{H}_3\text{BO}_3$ ). Inspired by ultrahigh temperature polymer-derived ceramic SiBCN, this body of work aims to assess the roles of boron in a powder-route silicon-based ceramic system in the context of bonding, structural development, and ultimate structural properties. It was found through Raman spectroscopy and  $^{11}\text{B}$  SS MAS-NMR that boron exists in threefold coordination with nitrogen in the turbostratic boron nitride (t-BN) structure, similarly to in SiBCN. Increasing boron concentration in resultant SiAlONs results in a decrease in the population of both residual  $\alpha$ - $\text{Si}_3\text{N}_4$  and second phases in the grain boundary, until a single phase  $\beta'$ -SiAlON was obtained at 3 wt%  $\text{H}_3\text{BO}_3$ . The grain size distributions of resultant SiAlONs were significantly narrowed by incorporating boron. Ultimately, fracture strength was increased from ~850 MPa to >1000 MPa by incorporating 3 wt%  $\text{H}_3\text{BO}_3$ . Subsequent in-depth fractographic analysis indicated that fracture origins of low-boron SiAlONs were predominantly inclusions consisting of either native material or foreign material from processing. However, boron-rich SiAlONs tended to fail from more elusive, less severe surface flaws such as machining cracks. It is proposed that the incorporation of boron reduces grain boundary diffusivity, mitigating abnormal grain growth or crystallization of second phases, effectively eliminating the worst flaw population in the present SiAlONs.

## I. INTRODUCTION

### A. Motivation and Opportunity for SiAlON Ceramics

Demands for high-temperature, low-density, chemically favorable, and structurally reliable materials have become more fervent in recent years. The global climate crisis has created the demand for more efficient processes in applications such as automotive and jet engines. The advent of certain additive manufacturing techniques has opened the door to the fabrication of custom biomedical implants, and now advances in materials for such implants are required to fully capitalize on this opportunity. More fundamentally, the growing body of knowledge on the topics of nanomaterials and molecular precursors is illuminating opportunities for the effective synthesis of previously inaccessible materials. While the theoretical properties of some advanced ceramics seem to meet the increasingly stringent demands of the modern age, their susceptibility to catastrophic brittle failure, and their strong dependence on flaw populations, make their implementation in high-risk applications problematic.

In order to increase the efficiency of engine processes, materials must be developed which can sustain extreme environments for extended periods of time. These environments may include high temperatures, corrosive atmospheres, cyclic loads, or large thermal gradients. Engine efficiency may be increased by increasing operating temperatures, retaining engine heat, and decreasing weight by utilizing low-density materials and eliminating cooling systems.<sup>1-2</sup> While advanced ceramics appear to be capable of actualizing these goals, they present a high risk of fracturing under the combination of cyclic loads, impact, and thermal shock presented by the engine service environment.

The area of structural biomaterials is constantly advancing on many fronts. Efforts are being made to incorporate therapeutic agents which can be delivered at controlled rates. The allergies some patients have to current implant materials are being addressed. Failure and rejection rates are constantly being decreased by the development of materials which are bioactive rather than simply bioinert or even biocompatible. Ceramics are generally composed of elements which are more commonly found in the body naturally than are metals.<sup>3</sup> It therefore may often be preferable to utilize a ceramic implant or scaffold than a

metal one for implantation. However, the issue of damage tolerance and brittleness of ceramics has stood in the way of their widespread use for certain types of implants. The nature of the chemical bonding in ceramics is such that they cannot store energy in the form of dislocations or other point defects as metals do, so their “yield stresses” are also their fracture stresses, and plastic deformation is not observed.<sup>4-5</sup>

Ceramic (and glass) fracture is governed by intrinsic and extrinsic flaw populations within the material.<sup>6</sup> Pores, inclusions, and surface flaws introduced by handling or machining can all act as stress concentrators, and potentially, fracture origins.<sup>7</sup> While ceramics are generally more chemically suited to the biological environment than metals are, and are often more chemically resistant in the corrosive environments of engines, they are much more difficult to machine into the complex shapes required for these applications. Moreover, the machining of ceramics often results in surface microcracks which can act as fracture origins. Therefore, the rise in prevalence of additive manufacturing has created the opportunity to print near-net-shape ceramic components and eliminate the necessity of machining.

Additive manufacturing may help eliminate the flaws introduced by classical machining, making ceramics more viable options for structural implants in the body. However, many of the ceramics which are relatively damage tolerant and would be viable for implantation also require pressure assisted sintering techniques, rendering most additive manufacturing techniques inaccessible. This problem is particularly poignant in the case of silicon nitride ( $\text{Si}_3\text{N}_4$ ) and its related materials.  $\text{Si}_3\text{N}_4$  exhibits remarkable biocompatibility, corrosion resistance, fracture toughness, and fracture strength, but its application is still limited by the difficulty in consolidation and grain boundary creep at high temperatures. Therefore, improvements in the sinterability of  $\text{Si}_3\text{N}_4$ -related materials may enable them to i) be produced in complex geometries ii) be sintered without pressure to retain the complex geometry imparted by additive manufacturing, and iii) eliminate the incorporation of surface flaws introduced by machining.

## **1. Current internal combustion engine materials**

Current automotive engine materials include, but are not limited to, materials such as cast iron, aluminum, and compact graphite iron (CGI). Carbon fiber-reinforced polymer composites are also utilized in low-temperature components. CGI is most common in diesel

engines as a cylinder lining material and in some high-performance automotive engines as a cylinder block material. The densities of CGI and cast iron are both in the realm of 7 g/cm<sup>3</sup>, in contrast to aluminum, which has a density of ~2.7 g/cm<sup>3</sup> but much lower elastic modulus and high-temperature fatigue resistance, and higher thermal expansion coefficient.<sup>8</sup>

Jet engine turbines present a more extreme environment than automotive engines, and as such require more exotic materials. Nickel-based superalloys are commonly utilized in these types of internal combustion engines, and actually comprise ~40-50% of the weight of the jet engine. Moreover, costly investment casting methods must be adopted to fabricate turbine blades which accommodate additional cooling systems to keep the blades below their softening temperatures of ~1050-1200 °C.<sup>9</sup> These superalloys are typically characterized by densities on the order of 7.7-9 g/cm<sup>3</sup> and melting temperatures of approx. 1300-1450 °C. Additionally, many later-generation Ni-based superalloys contain expensive alloying constituents such as rhenium and tantalum.

More recent efforts to replace dense, expensive metal alloys and their coolant systems with lower density, higher temperature materials have focused on ceramic matrix composites (CMCs).<sup>10-11</sup> Common CMCs may fall under the categories of SiC/SiC (silicon carbide-reinforced silicon carbide), ox/ox (oxide-reinforced oxide), or carbon-reinforced CMCs (utilizing carbon fibers or nanotubes). Carbon fiber-reinforced polymeric composites possess densities of ~1.5-2.0 g/cm<sup>3</sup>,<sup>12</sup> the densities of SiC/SiC composites are ~2.5-3.0 g/cm<sup>3</sup>,<sup>13</sup> and ox/ox CMCs typically have densities of approx. 2.0-2.5 g/cm<sup>3</sup>.<sup>14</sup> However, particularly in the case of SiC fiber-reinforced materials, processing the fibers into mats which can then be infiltrated with a matrix precursor can be quite difficult. It would therefore be beneficial to fabricate low-density monolithic ceramics which can inherently withstand the corrosive environments, high temperatures, and cyclic loads characteristic of these applications.

## 2. Current structural biomaterials

Another field which would benefit greatly from the efficient densification of advanced structural ceramic monoliths is the field of biomedical implants. Bioimplantation has a long history, dating back to early Egyptian and Chinese cultures. Wood, shells, gold, copper, porcelain, stainless steel, and titanium have been used throughout history to replace

hard tissues in the body, and bioactive glasses are used to deliver therapeutic agents to localized sites in the body, often at controlled rates.<sup>15-16</sup> Currently, the material most commonly utilized as hard tissue replacement (bone/dental implant) is titanium, often with surfaces that have been roughened and/or coated with mineral powders such as hydroxyapatite (HA).<sup>17</sup> Previous stainless steel implants were recognized as foreign objects in the body and would be wrapped in scar-like tissue, a process known as fibrous encapsulation. It was then found by Dr. P. I. Bränemark, *et al.* that bone would actually bond to titanium.<sup>18</sup> Steel implants relied on a very tight mechanical fit to ensure that rejection would not occur. In contrast, bone cells are more likely to proliferate on titanium surfaces, so that a chemical bond may also be formed between the implant and the native tissue rather than a fibrous capsule.

While titanium is still a viable material for implantation in bone, it comes with some drawbacks. Some patients have metal allergies. Further, in some locations in the body, the implant may become visible over time, as with dental implant posts. In this case, a material which is a similar color to native tooth is aesthetically preferable. Most importantly, however, are the surface properties of the implant material. While titanium favors bone cell differentiation and proliferation, the metal itself is dissimilar in chemistry and microstructure from native hard tissue. Consequently, it is biocompatible, but not necessarily *bioactive*. Bioactivity is a dynamic property of a material which allows it to not only coexist with native tissue but work synergistically with it. Minerals like hydroxyapatite ( $\text{Ca}_{10}(\text{PO}_4)_6(\text{OH})_2$ ), which can be synthetically produced, are actually also naturally present in the calcified tissues of the human body.<sup>19</sup> Because of the close similarity between HA and native hard tissue, no cytotoxic effects are seen as a result of implantation.<sup>3</sup> HA can actually be absorbed over time by the body's natural bone remodeling processes and be replaced by native tissue.<sup>20</sup>

In addition to bioactive ceramic material HA,  $\text{ZrO}_2$  is another important bioceramic.<sup>21</sup>  $\text{ZrO}_2$  exhibits excellent strength and toughness, which arises from a crystallographic phase transition induced by a crack itself. This toughening mechanism, called transformation toughening, occurs in  $\text{ZrO}_2$  which has been stabilized in its tetragonal structure, usually by  $\text{Y}_2\text{O}_3$ . The notations “3Y-TZP”, meaning “3 mole % yttria - tetragonal zirconia polycrystals”, or “YSZ”, meaning “yttria-stabilized zirconia”, are often adopted.

When a crack propagates through YSZ, the stress at the crack tip induces a phase transformation from the tetragonal phase to the monoclinic phase, which has a slightly larger volume. This phase transition creates a localized region of compression at the crack tip and helps counteract the “Mode I” crack opening process.<sup>22</sup> This toughening mechanism has enabled the implementation of ZrO<sub>2</sub> in select implants, such as femoral heads in hip implants. ZrO<sub>2</sub> is extremely abrasion resistant, which makes it a good candidate for this application, but it is extremely difficult to machine and polish to sufficient surface finish for the same reason.

Additive manufacturing techniques such as Robocasting<sup>23</sup> have opened the door to the fabrication of near-net-shape ceramic components, and consequently offer alternatives to the difficult and costly ceramic machining paradigm. Further, the increasing use of micro-computed tomography (CT) scanning in medical settings can be coupled with additive manufacturing to fabricate custom implants which are almost perfectly suited to the individual patient, all without the incorporation of surface flaws introduced by machining.<sup>24</sup> However, as previously mentioned, ceramics which require pressure-assisted sintering techniques for densification are not suited for 3D-printed components. It would therefore be greatly beneficial to develop a method for the efficient densification of advanced ceramics without the use of pressure, while still accessing the properties which made them interesting in the first place. Improving the densification capability of covalent ceramics without detriment to their high-temperature properties would help save energy and enable the manufacture of complex-shape, high-temperature, structural ceramic monoliths such as turbine blades and custom hard tissue implants.

## B. Background on Silicon Nitride

The corrosion resistance, strength, and excellent toughness of silicon nitride (Si<sub>3</sub>N<sub>4</sub>)-based ceramics have made them attractive candidate materials for structural monoliths used in extreme environments since the 1970s.<sup>25-28</sup> In fact, this interest has remained relatively consistent ever since, as the global silicon nitride market is expected to grow to \$222 million by 2026, with a compound annual growth rate (CAGR) of 8.92%.<sup>29</sup> It is therefore unsurprising that the structure-property relationships of these materials have been and continue to be extensively studied.<sup>30-31</sup>

Silicon nitride-based ceramics are currently used in applications such as high-temperature bearings and cutting tools, as well as selected engine and turbine components and coatings.  $\text{Si}_3\text{N}_4$  is often thought of as a relatively mature material, but its application space is expanding with innovations in nanomaterials and ceramic precursors, as well as some recent discoveries in biomedical implants, all in the context of the global demand for higher-performance materials.

The potential for silicon nitride biological implants is beginning to be revealed.<sup>32</sup><sup>33</sup> It has recently been discovered that  $\text{Si}_3\text{N}_4$  is simultaneously osteogenic and antimicrobial thanks to its surface chemistry. This tendency to both facilitate human bone cell proliferation and inhibit bacterial and viral proliferation arises from the formation of silanol ( $\text{SiOH}$ ) surface groups and consequent elution of ammonium ( $\text{NH}_3$ ) or ammonia ( $\text{NH}_4^+$ ) ions.<sup>32</sup> A cascade of surface reactions occurs which has been shown to be effective in neutralizing bacteria such as *E. coli* and viruses such as SARS-CoV-2. This phenomenon, coupled with the excellent structural properties of  $\text{Si}_3\text{N}_4$ , makes it very interesting as a bone implant.

Of particular interest is the fracture behavior of silicon nitride ceramics, which can involve a complex combination of synergistic multiscale toughening mechanisms, inter- and transgranular fracture, mixed flaw populations, and appreciable r-curve behavior.<sup>34-37</sup> Sintering additives and second phases surely influence these phenomena, and their atomistic roles and consequential effect on mechanical performance have proven difficult to elucidate. A deep understanding of the changes to bonding and structure of silicon nitride bulk materials induced by additives and second phases would allow for greater control of the fracture behavior of these materials and open the door to multiscale tailoring of structure and mechanical properties.  $\text{Si}_3\text{N}_4$  macrostructures may then be used as substrates on which smaller structures with tailored properties may be printed with the goal of intentionally controlling crack paths and ultimately, failure.<sup>38</sup>

## 1. Crystallography of $\text{Si}_3\text{N}_4$

$\text{Si}_3\text{N}_4$  has been a very interesting engineering ceramic for decades.<sup>39-40</sup> One of the primary reasons for the interest it has garnered is its excellent fracture toughness. As opposed to the toughening mechanism of YSZ, the origin of fracture toughness in  $\text{Si}_3\text{N}_4$  is its microstructural morphology. Silicon nitride can grow high aspect ratio rod-like

crystallites which act to deflect propagating cracks and bridge behind them.<sup>30, 34-35, 41</sup> In this way,  $\text{Si}_3\text{N}_4$  can be thought of as a sort of in-situ fiber-reinforced composite. However, in  $\text{Si}_3\text{N}_4$ , the “fibers” are grown, rather than being added as a starting material, which can present processing issues such as agglomeration of fibers. A bridging grain behind a propagating crack can help counteract the crack opening and reduce the tensile stress at the crack tip. When a bridging grain is pulled out of the matrix, some of the energy of the crack is absorbed in the frictional force between the grain and the surrounding matrix. These toughening mechanisms are known as crack bridging and grain pullout. A typical  $\text{Si}_3\text{N}_4$  microstructure is found in Figure 1, wherein long, rod-like grains are embedded in a fine-grained matrix.<sup>42</sup>

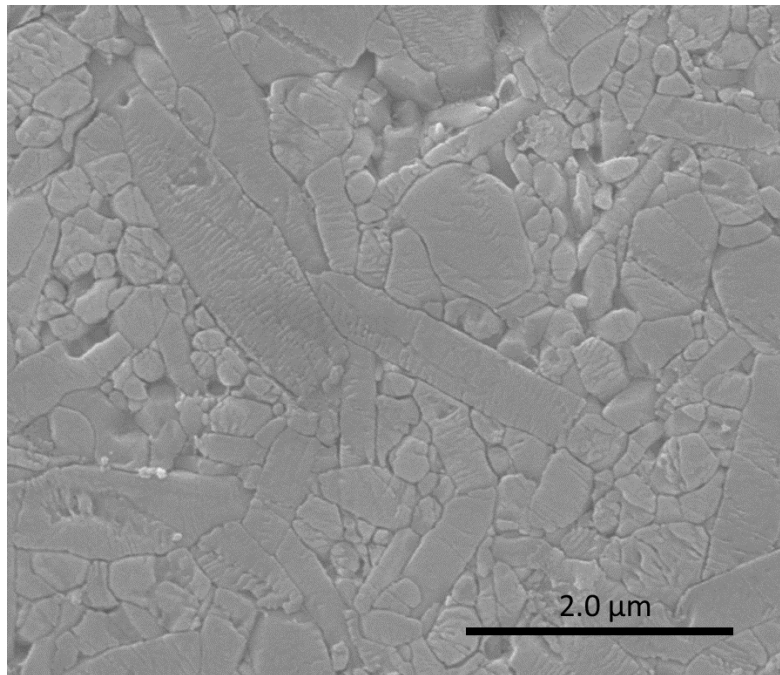


**Figure 1.** Typical  $\text{Si}_3\text{N}_4$  microstructure, wherein long rod-like grains are embedded in a fine-grained matrix.<sup>42</sup>

$\text{Si}_3\text{N}_4$  has two common, technologically important polymorphs, denoted  $\alpha$  and  $\beta$ , both of which have hexagonal symmetry.  $\alpha\text{-Si}_3\text{N}_4$  is assigned to the  $\text{P}3_1\text{c}$  space group with  $a = b = 7.818 \text{ \AA}$  and  $c = 5.591 \text{ \AA}$ , and usually exhibits relatively equiaxed grains.  $\beta\text{-Si}_3\text{N}_4$  is assigned to the  $\text{P}6_3$  space group with  $a = b = 7.595 \text{ \AA}$  and  $c = 2.902 \text{ \AA}$ , and forms the long, needle-like grains which grow along the  $c$ -axis (Figure 1).<sup>25, 43-46</sup>

The atomic arrangements of these two polymorphs can be found in Figure 2 and Figure 3. (Images were generated using CrystalMaker<sup>®</sup>: a crystal and molecular structures program for Mac and Windows. CrystalMaker Software Ltd, Oxford, England ([www.crystalmaker.com](http://www.crystalmaker.com))). Both exhibit a similar layered ring structures consisting of corner-shared SiN<sub>4</sub> tetrahedra, with the main difference being that  $\beta$ -Si<sub>3</sub>N<sub>4</sub> exhibits an ABAB stacking scheme, while  $\alpha$ -Si<sub>3</sub>N<sub>4</sub> exhibits an ABCDABCD stacking scheme.<sup>45, 47</sup> The  $\alpha$  structure essentially consists of alternating layers of  $\beta$ -Si<sub>3</sub>N<sub>4</sub> and its mirror image, accounting for the larger c dimension of its unit cell by about a factor of 2. Consequently,  $\beta$ -Si<sub>3</sub>N<sub>4</sub> exhibits tunnel structures parallel to the c-axis which are interrupted in the  $\alpha$  structure by the action of a c glide plane and become large pockets or interstices.<sup>25, 48</sup> Actually, the growth of  $\beta$ -Si<sub>3</sub>N<sub>4</sub> is often considered to be an abnormal grain growth phenomenon which is energetically favorable due to the large basal plane of the  $\beta$ -Si<sub>3</sub>N<sub>4</sub> structure.<sup>49</sup>

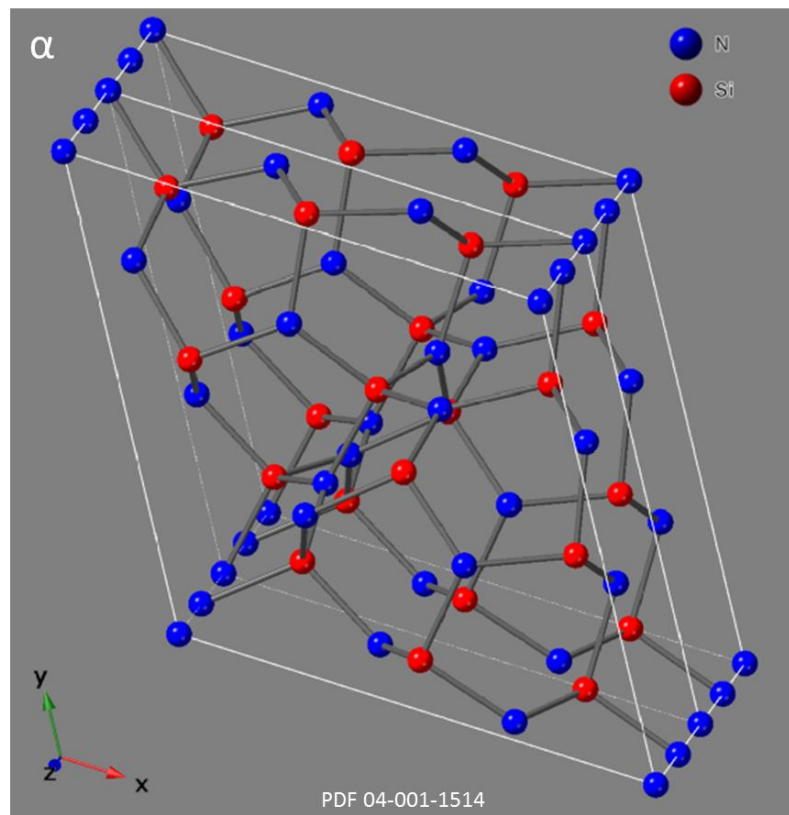


**Figure 2.**  $\alpha$ -Si<sub>3</sub>N<sub>4</sub> crystal structure. White lines indicate the unit cell.

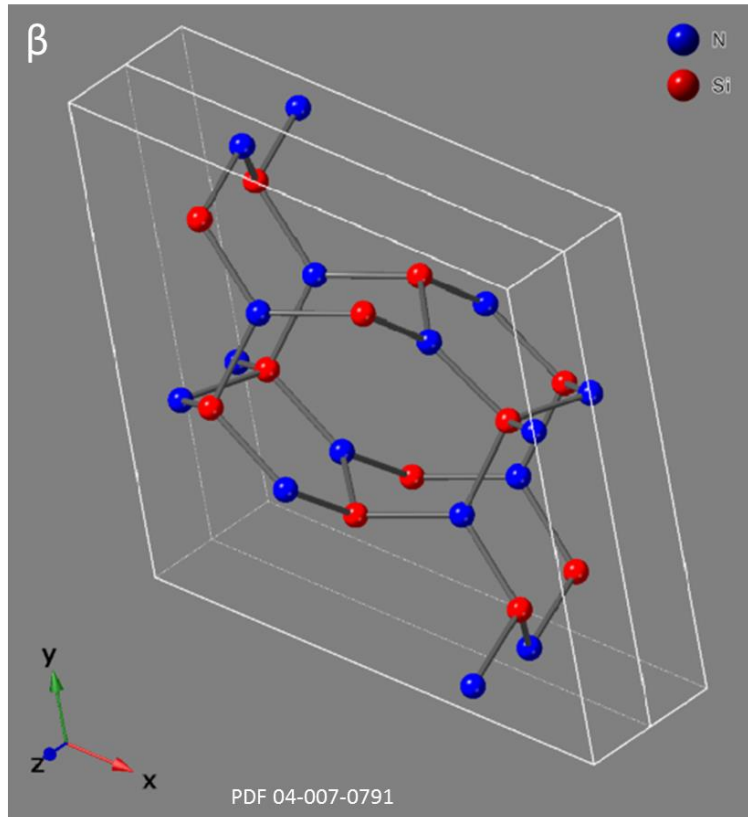


**Figure 3.  $\beta$ - $\text{Si}_3\text{N}_4$  crystal structure. White lines indicate the unit cell.**

## 2. Sintering, additives, and phase compatibility

The densification and structural evolution of  $\text{Si}_3\text{N}_4$  is enabled by a combination of numerous possible sintering additives, commonly  $\text{Al}_2\text{O}_3$ ,  $\text{Y}_2\text{O}_3$ , AlN, and some other alkali earth or rare earth oxides. Sintering additives form a liquid phase at high temperatures and partially reside at the grain boundary after sintering as a glassy or devitrified phase to which much attention has been paid throughout the years.<sup>50</sup> Typical starting powder  $\alpha$ - $\text{Si}_3\text{N}_4$  is converted to the  $\beta$  phase via dissolution and reprecipitation.

The  $\text{Al}_2\text{O}_3$ - $\text{Y}_2\text{O}_3$  additive system is one of the most investigated and successful. Yttria and alumina exhibit a eutectic at 1760 °C.<sup>51</sup> However, silicon nitride starting powder always contains an oxide layer which effectively incorporates  $\text{SiO}_2$  as another pseudo-starting material.<sup>46</sup> The yttria-alumina-silica system exhibits a eutectic at approximately 1370 °C, though there is some debate about the exact temperature.<sup>52-53</sup> This is the lowest-

temperature eutectic possible from any combination of  $\text{Y}_2\text{O}_3$ ,  $\text{Al}_2\text{O}_3$ , or  $\text{SiO}_2$ .<sup>54-55</sup> Phase equilibrium diagrams for the ternary system  $\text{Y}_2\text{O}_3\text{-}\text{Al}_2\text{O}_3\text{-}\text{SiO}_2$  can be found in Figure 4.<sup>52</sup>

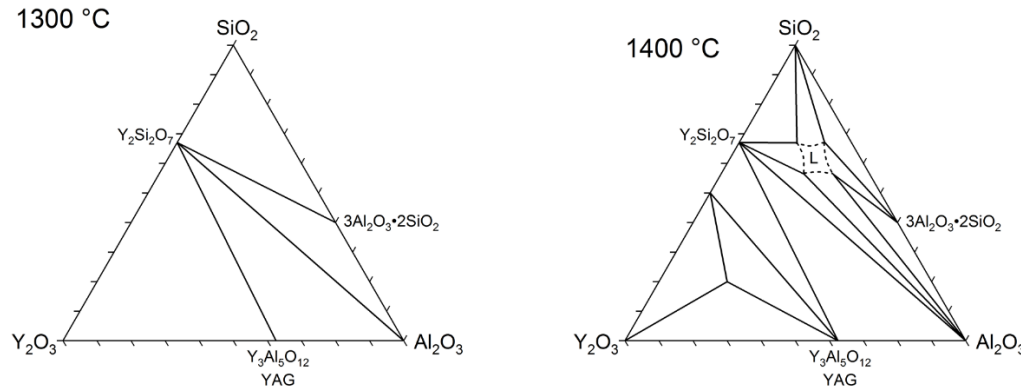
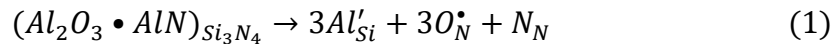


**Figure 4.** Phase equilibrium diagrams for the  $\text{Y}_2\text{O}_3\text{-}\text{Al}_2\text{O}_3\text{-}\text{SiO}_2$  system at 1300 °C and 1400 °C. Note that a melt forms between these temperatures. Adapted from Kolitsch, *et al.*, (1999).<sup>52</sup>

Another major consequence of the addition of additives is a well-documented solid solution of Al and O in the  $\text{Si}_3\text{N}_4$  lattice, where Al substitutes on the Si site and O on the N site.<sup>40</sup> This solid solution works in tandem with the liquid phase sintering additive by increasing the overall ionicity of the structure, thereby increasing the atomic diffusivities necessary for densification. Charge balance is maintained by a 1:1 ratio of Al and O substitutional defects. This is often achieved by incorporating equimolar quantities of  $\text{Al}_2\text{O}_3$  and AlN. (Note that no evidence for a lower eutectic with the incorporation of AlN has been reported.<sup>56</sup>) Al and O tend to cluster and form Al-O bonds, rather than distribute randomly in the silicon nitride lattice.<sup>57-59</sup> The resulting material is referred to as a SiAlON whose major polymorphs,  $\alpha'$ - and  $\beta'$ -SiAlON, are analogous to  $\alpha$ - and  $\beta$ - $\text{Si}_3\text{N}_4$ . It has been reported that the  $\beta$  silicon nitride lattice can accommodate up to 67 mole percent  $\text{Al}_2\text{O}_3$ .<sup>60</sup> The Kröger-Vink defect equation can be found in Equation 1.



From the schematic Si-Al-O-N compositional pyramid presented in Figure 5, a square plane can be drawn with corners corresponding to the common starting materials

for SiAlON synthesis:  $\text{Si}_3\text{N}_4$ , 4(AlN), 2( $\text{Al}_2\text{O}_3$ ), and 3( $\text{SiO}_2$ ).<sup>61</sup> Figure 6 highlights many of the phase relationships in the SiAlON system in this fashion.<sup>61-65</sup>

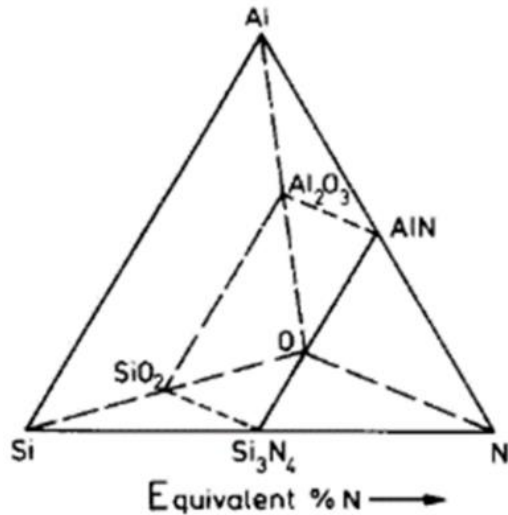


**Figure 5.** Schematic compositional pyramid for the Si-Al-O-N system. Note that the common starting materials for the synthesis of SiAlONs -  $\text{Si}_3\text{N}_4$ , 4(AlN), 2( $\text{Al}_2\text{O}_3$ ), and 3( $\text{SiO}_2$ ) - can be found along four of the edges of the pyramid.

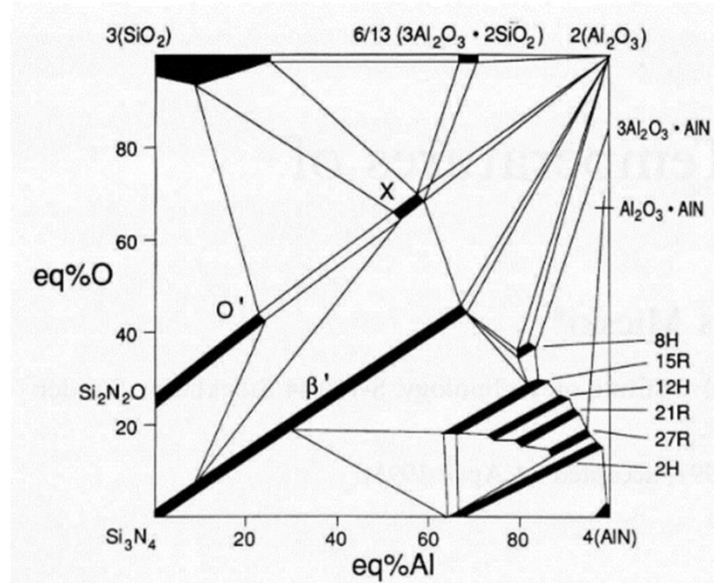


**Figure 6.** SiAlON phase diagram, highlighting many SiAlON polytypes.

The inclusion of yttrium into the system requires additional dimensions. A Jänecke prism detailing many known phases of the Y-Si-Al-O-N system is presented in Figure 7.<sup>66</sup><sup>68</sup> This phase compatibility prism details the yttrium-containing system, but Gd, Dy, Sm, and Er have also been demonstrated in this role. Note that  $\alpha'$ -SiAlON is stabilized by the presence of Y and lies near the  $\text{Si}_3\text{N}_4$  corner of the  $\text{Si}_3\text{N}_4 - \text{YN}:3\text{AlN} - 4/3(\text{Al}_2\text{O}_3:\text{AlN})$  plane. It has the formula  $\text{Y}_x\text{Si}_{3-(3x+n)}\text{Al}_{3x+n}\text{O}_n\text{N}_{4-n}$ , where  $0.08 < x < 0.17$  and  $0.13 < n < 0.31$ .<sup>45</sup>  $\beta'$ -SiAlON lies on the  $\text{Al}_2\text{O}_3:\text{AlN}$  line, making up a large part of the  $\alpha'$  plane border, and has the formula  $\text{Si}_{6-z}\text{Al}_z\text{O}_z\text{N}_{8-z}$ , where  $0 < z < \sim 4.2$ .<sup>69</sup>

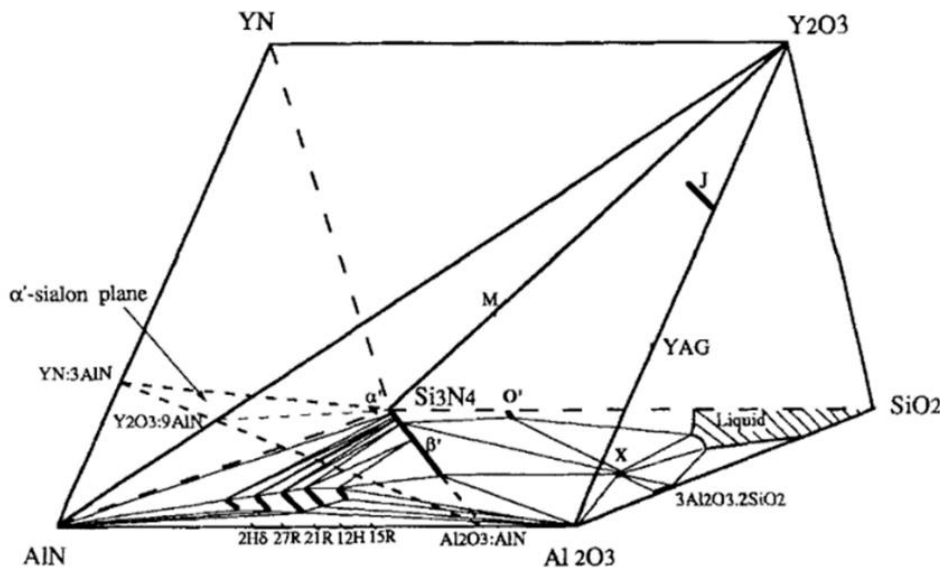


**Figure 7. Jänecke prism summarizing the phase compatibility of the SiAlON system with YN and Y<sub>2</sub>O<sub>3</sub>.**

### 3. Minor SiAlON polytypoids

Several minor polytypoid phases have been identified within the compositional bounds defined above. The five yttrium-free phases 2H, 27R, 21R, 12H, and 15R are structurally related and are based on the wurtzite-type structure of AlN.<sup>45, 48, 70</sup> These phases represent stoichiometric increases in AlN content as the AlN corner of the quaternary phase diagram is approached.<sup>61</sup> “J” denotes a woehlerite phase with the end member  $\text{Y}_4\text{Si}_2\text{O}_7\text{N}_2$  and the ability to dissolve Al and O to form a solid solution  $\text{Y}_{4-x}\text{Al}_x\text{O}_{7+x}\text{N}_{2-x}$  which extends in the direction of pure yttrium aluminum monoclinic (YAM),  $\text{Y}_4\text{Al}_2\text{O}_9$  ( $x = 2$ ).

“M” represents a melilite phase of composition  $\text{Y}_2\text{Si}_3\text{O}_3\text{N}_4$  which, upon dissolution of Al-O, is described by  $\text{Y}_{2-x}\text{Al}_x\text{O}_{3+x}\text{N}_{4-x}$ .<sup>67</sup> These M and J phase solid solutions in yttrium-containing systems are denoted M’(Y) and J’(Y).

Previously, these minerals were considered as undesirable secondary phases in silicon nitride systems because their oxidation and subsequent formation of crystobalite and yttrium disilicate ( $\text{Y}_2\text{Si}_2\text{O}_7$ ) at around 1000 °C were accompanied by an approximate 30% volume expansion, causing failure. However, the replacement of Si-N with Al-O has increased their oxidation resistance, making both melilites and wohlerites viable intergranular phases in SiAlONs. Both are refractory ceramics ( $1750 \text{ }^{\circ}\text{C} < T_{\text{melt}} < 1900 \text{ }^{\circ}\text{C}$ ) which do not form low temperature eutectics with the  $\text{Si}_3\text{N}_4$  matrix.<sup>47, 71-72</sup>

Many studies have compared the phase compatibility and solid solubility of aluminum in M and J phases containing various rare earth elements. It was found that Al and O solubility (x value) decreases with decreasing rare earth ionic radius. Consequently, M’(Y) and J’(Y) phases have exhibited amongst the lowest solubility for Al due to the relatively small ionic radius of yttrium (0.9 Å).<sup>72-74</sup> It has also been shown that J(R) is increasingly stable with decreasing RE ionic radius, meaning that it is most stable in yttrium-containing systems.<sup>71</sup>

#### 4. The role of Al and O in SiAlONs

The dissolution of Al and O in the primary SiAlON phases as well as the minor polytypoids has crystallographic implications as well. Increases in both the a and c lattice parameters with increasing solid solution level in the β'-SiAlON phase were measured by Ekström, *et al.* in diffraction experiments on glass-encapsulated hot isostatically pressed SiAlONs.<sup>69</sup> In a study on oxygen contamination of α- $\text{Si}_3\text{N}_4$ , it was found that its unit cell volume drastically decreases with as little as 0.1 wt% O contamination.<sup>75</sup> The lattices of M’(R) and J’(R) phases were shown to expand with Al dissolution for various rare earth oxide additives.<sup>71, 73, 76-77</sup>

Obviously, Al is contributed by  $\text{Al}_2\text{O}_3$ , but AlN is often included in tandem with alumina to starve the system of oxygen and achieve the 1:1 ratio of Al and O necessitated by the β'-SiAlON formula ( $\text{Al}_2\text{O}_3 \bullet \text{AlN} = \text{Al}_3\text{O}_3\text{N}$ ). Further, O is contributed by alumina, but also by  $\text{Y}_2\text{O}_3$  and even by oxygen adsorbed on the surface of the starting α- $\text{Si}_3\text{N}_4$  powder, which should be accounted for as  $\text{SiO}_2$ . Often, the oxygen contributed by yttria is

assumed to have remained confined to the grain boundary phase. Finally, it is seldom known how much Si, Al, O, and N is confined to the grain boundary phase and how much is included in the  $\text{Si}_3\text{N}_4$  lattice. A few studies on glass systems deemed representative of the grain boundary phase have been performed in order to elucidate their structure, properties, and degree of crystallinity.<sup>50, 55, 78-79</sup>

The full densification of  $\text{Si}_3\text{N}_4$  is often only possible through the incorporation of additives, there is a wide variety of additives which have proven effective to varying degrees, and the additives certainly have marked effects on the ultimate properties of the SiAlON. Therefore, this subtopic of SiAlONs has always attracted much interest and investment. The rare earth oxide used to facilitate the generation of the liquid phase influences the types of second phases at the grain boundary which likely arise, such as the melilites and woehlerites mentioned previously.<sup>71</sup> The concentration of solute atoms in the  $\text{Si}_3\text{N}_4$  lattice (“z” value in  $\beta'$ -SiAlON formula  $\text{Si}_{6-z}\text{Al}_z\text{O}_z\text{N}_{8-z}$ ) dictates the overall covalency or ionicity of the system. The volume of the liquid phase impacts the sinterability microstructure, and fracture behavior of the system. When making high-temperature, high-performance SiAlONs, researchers usually target what are known as “low-z” SiAlONs, meaning SiAlONs with low concentrations of Al and O. They also try to minimize the volume of the glassy grain boundary phase. The idea is then to provide just enough sintering additive to facilitate densification, but no more.

## 5. Effect of additives on SiAlON structural properties

The enigmatic glassy grain boundary film in SiAlONs has been the focus of so many research efforts over the years that it has become its own dedicated field of research. This is because in addition to having implications on the sintering of SiAlONs, the grain boundary is also critical to the high-temperature structural properties of the ceramics. At high temperatures, the grain boundary is prone to softening and can cause thermal creep deformation caused by long-term exposure to moderate cyclic or constant loads. The main mechanisms of creep in SiAlONs are grain sliding and grain boundary cavitation.<sup>27</sup> It is for this reason that the volume of grain boundary glass needs to be minimized. The use of pressure-assisted sintering techniques such as uniaxial hot pressing (HP) and hot isostatic pressing (HIP) allows for further reduction in the glassy phase.

Similarly, the concentration of solute Al and O atoms in the  $\text{Si}_3\text{N}_4$  lattice is kept to the minimum required to facilitate economic densification. As the concentrations of Al and O increase, the covalency of the system decreases, which is why the solid solution aids densification in the first place. However, decreasing covalency also generally comes with a sacrifice to the structural properties like hardness and strength that made silicon nitride interesting in the first place. Therefore, once again only enough Al and O to facilitate densification without severe detriment to structural properties should be incorporated. The goal is to access properties which are as close to those of pure  $\text{Si}_3\text{N}_4$  as possible while still enabling full densification.

Different ratios of  $\alpha'$  and  $\beta'$  phase in the resultant SiAlON have been shown to yield different combinations of toughness, hardness, and strength. For these reasons, the conversion process is often carefully controlled.<sup>45</sup> Because the c-axis of the  $\alpha$  phase is about twice as large as that of the  $\beta$  phase, the Burgers vector for dislocation motion is also much larger and the alpha phase is consequently significantly harder.<sup>80-82</sup> Therefore, there is an inverse relationship between hardness and  $\beta'$  phase concentration (or similarly, degree of  $\alpha' \rightarrow \beta'$  conversion). However, having a more equiaxed morphology,  $\alpha'$  grains do not contribute to the toughness of  $\text{Si}_3\text{N}_4$  nearly as much as  $\beta'$  phase grains do. Often, it seems that a trade off between the two is struck based on the end application.

### C. Molecular Precursors to Ceramics

In contrast to the conventional powder processing route to ceramics, the advent of new molecular precursors to ceramics has opened the door to novel, otherwise inaccessible advanced ceramics.<sup>83</sup> Wet chemical routes have been investigated in the last few decades as pathways to tailor-made ceramics built from the atomic level. Some of these ceramic precursors, or preceramic polymers, have become commercially available, many are soluble in various solvents, and most are used to synthesize fibers, coatings, nanoparticles, or matrix phases in ceramic matrix composites (CMCs). Polymer-derived ceramics (PDCs) typically have compositions such as  $\text{SiC}$ ,  $\text{SiO}_x\text{C}_y$ ,  $\text{SiO}_x\text{N}_y$ ,  $\text{SiC}_x\text{N}_y$ , or  $\text{Si}_3\text{N}_4$ , or are modified with elements such as B, Al, Zr, Hf, or others, depending on the application.<sup>84-85</sup>

Owing to the tailorabile nature of the polymer synthesis procedure, the chemistries of the resulting PDCs are highly tunable, and are not restricted to the stoichiometries of the

crystalline powder starting materials conventionally utilized. Moreover, PDCs often do not contain grain boundaries as they were not synthesized from crystallites. This means that many of the problems with grain boundaries characteristic of polycrystalline high-temperature ceramics are not a factor, such as high temperature creep induced by grain boundary glass softening.<sup>86</sup> Further, most of the polymer-processing techniques, such as spin coating, dip coating, melt forming, injection molding, fiber drawing, and polymer infiltration and pyrolysis (PIP) are available to preceramic polymers, enabling the fabrication of complex-geometry, near-net-shape components.<sup>87</sup> Finally, preceramic polymers are converted to inorganic PDCs at much lower temperatures than in the powder consolidation process (1000 – 1400 °C).<sup>87-88</sup>

### 1. Sol-gel synthesis of SiO<sub>2</sub> and Al<sub>2</sub>O<sub>3</sub>

Some specific PDCs which are relevant to the present thesis, and their classes of precursors, will be discussed momentarily. For the moment we will consider precursors to more ubiquitous ceramics, such as SiO<sub>2</sub> and Al<sub>2</sub>O<sub>3</sub>. Sol-gel synthesis of SiO<sub>2</sub> was first demonstrated in 1844, but widespread research was undertaken within the last 50 years.<sup>89</sup> Tetraethyl orthosilicate (tetraethoxysilane, TEOS, Figure 8) is commonly used as a precursor to SiO<sub>2</sub>.<sup>90</sup> The general process for the precipitation of nanoparticles from TEOS and other alkoxides is known as hydrolysis and polycondensation. This process is initiated by water (in the presence of a catalyst such as HCl or NH<sub>3</sub>), such that one of the OC<sub>2</sub>H<sub>5</sub> groups is removed from the Si tetrahedron, being replaced with a silanol (Si-OH) group and liberating C<sub>2</sub>H<sub>5</sub>OH. Then, two adjacent Si-OH groups react to form Si-O-Si bonds, such as are found in SiO<sub>2</sub>, and a water molecule. The liberation of a water molecule from this process essentially means that hydrolysis and polycondensation of TEOS can be considered a self-propagating cascade of reactions. These reactions are schematically represented in Equations 2, 3, and 4. Reaction 2 represents the hydrolysis of TEOS, reaction 3 represents condensation of Si-O-Si bonds by the evolution of water, and reaction 4 represents condensation by liberation of ethanol.<sup>91</sup>

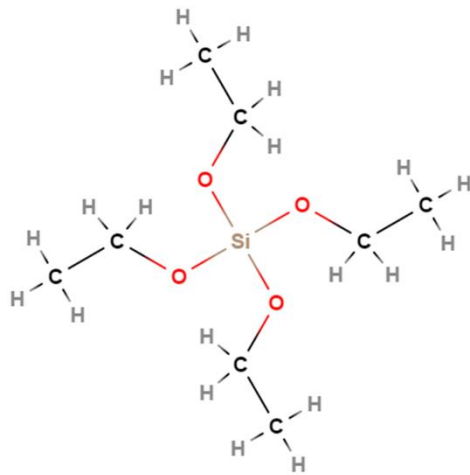
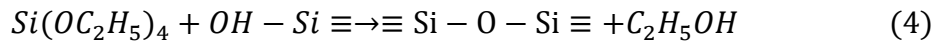
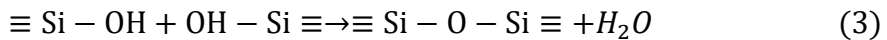
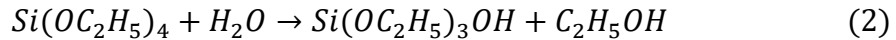


**Figure 8. Molecular structure of tetraethyl orthosilicate (TEOS).**



Similar reactions can be observed in other metal-alkoxides, such as aluminum tri *sec*-butoxide (ASB, Figure 9), where the  $CH_3CO^-$  groups are replaced by Al-OH bonds, which further condense into Al-O-Al bonds with concomitant release of water.<sup>92</sup> ASB has been used to synthesize high-purity  $Al_2O_3$  powders and mesoporous  $Al_2O_3$ .<sup>92</sup>

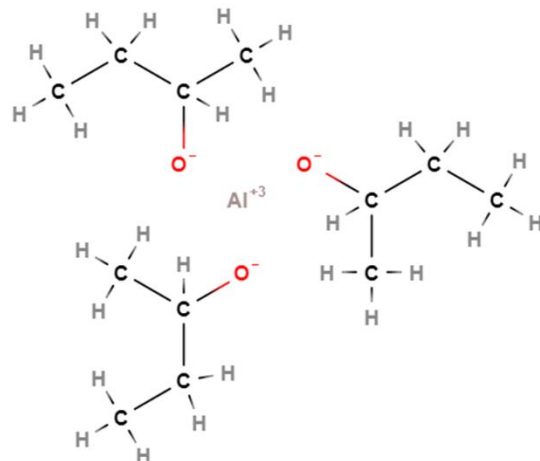


**Figure 9. Molecular structure of aluminum tri *sec*-butoxide (ASB).**

These hydrolysis-polycondensation reactions must be carefully monitored to control the particle size of the precipitates, but this route is widely recognized as a method for the synthesis of highly pure oxide powders, coatings, or fibers. Learnings in the field of wet chemical synthesis of inorganic materials, and their subsequent heat treatments, helped pave the way for the synthesis of many other polymer-derived ceramics, particularly ultra-high temperature (UHT) silicon-based polymer-derived ceramics.

#### D. Silicon Carbonitride/Silicoboron Carbonitride/Turbostratic BN Background

Silicoboron carbonitride (SiBCN) encompasses a family of X-ray amorphous polymer-derived ceramics (PDCs) which have been of great technical interest for the past 30 years.<sup>88, 93-95</sup> These materials exhibit high-temperature stability, strength, creep resistance, hardness, and oxidation resistance which can largely be attributed to their covalent bonding and complex nanostructures. Pure SiBCN materials derived from precursors synthesized in extremely dry, oxygen-free environments have been shown by TGA to resist thermal decomposition up to temperatures of 2000 °C.<sup>93</sup> This is in contrast to boron-free SiCN, which exhibits temperature resistance to only ~1500 °C.<sup>93</sup> The thermogravimetric behavior of these materials is illustrated in Figure 10. These nuances in thermal stability, among other phenomena, ultimately arise from the nature of the polymer processing route.

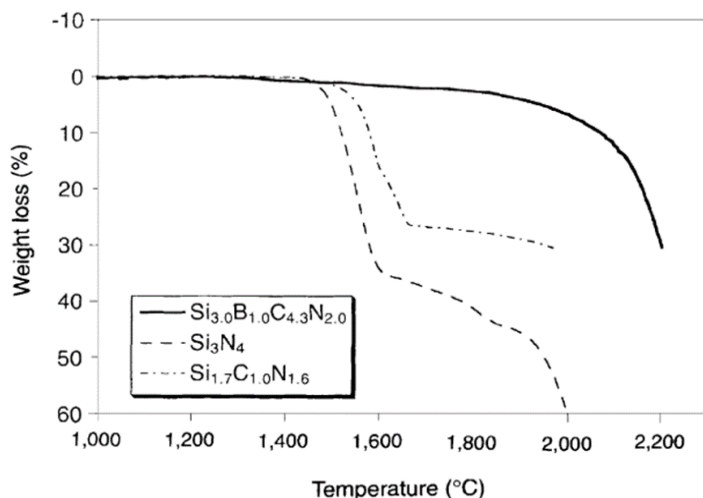
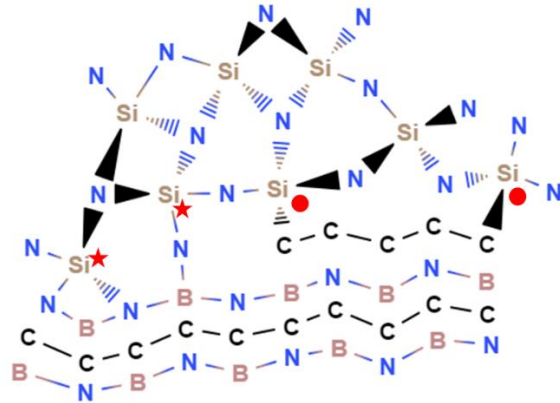


Figure 10. Thermogravimetric behavior of SiBCN in comparison to  $\text{Si}_3\text{N}_4$  and  $\text{SiCN}$ .<sup>93</sup>

The molecular-level tailorability of the polymer precursor structure allows for enhanced control of chemistry and bonding when compared with powder processing techniques. Thus, one may build high-temperature ceramics from the atomic level. Additionally, strong covalent bonding in powder alternatives  $\text{Si}_3\text{N}_4$ ,  $\text{SiC}$ ,  $\text{B}_4\text{C}$ , and  $\text{BN}$  inhibits diffusivity, making these materials difficult to sinter.<sup>96</sup> Finally, the PDCs do not contain significant grain boundaries, which are known to cause creep and failure in certain systems through softening at elevated temperatures, approximately 1500 °C for crystalline silicon nitride.<sup>27, 97</sup>

### 1. Structures of SiCN and SiBCN

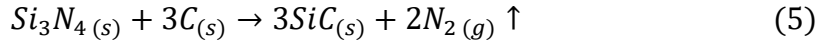
The structures of SiCN and SiBCN are comprised of nano-sized chemical domains of silicon-based tetrahedra which are “wrapped” in layers of disordered 6-fold rings. Naturally, these domains have some interfacial region between them, highlighted in Figure 11.<sup>98</sup> Owing to the highly tailorable nature of the polymer route to ceramics, it has been found that even the bonding in this interfacial region can be controlled. It was reported by Widgeon and coworkers that the use of more linear polymeric precursors to SiCN yields ceramics in which the Si at the domain interfaces is bonded fairly exclusively with N, and carbon is predominantly found in its graphitic layered form. In contrast, the use of more branched precursors yields SiCN which exhibits “mixed”  $\text{SiN}_{4-x}\text{C}_x$  ( $0 \leq x \leq 4$ ) tetrahedra at the domain interfaces.<sup>99</sup> A paper revealing a similar trend was published a year later, where the group found that in SiBCN ceramics derived from a linear polysilylcarbodiimide (PSCD), Si was primarily coordinated with N, which was then bonded to either B or C as the interfacial motif. On the other hand, SiBCN derived from a more branched polysilazane (PSZ) exhibited domain interfaces rich in mixed Si tetrahedra.<sup>100</sup> The consequences of these bonding schemes will be discussed in the following section (pg. 20).



**Figure 11.** SiBCN nanostructure, highlighting the interfacial region between Si-N tetrahedral domain and layered C/BN domain. Chemical domains are on the order of nanometers. ★-exclusive interfacial tetrahedron. ●-mixed interfacial tetrahedron.

## 2. Thermal decomposition of Si(B)CN

In SiCN and SiBCN systems,  $\text{Si}_3\text{N}_4$  begins to crystallize within the Si-N domains at elevated temperatures. This initiates the proposed thermal decomposition mechanism found in Equation 5.



where silicon nitride is attacked by free carbon in the structure and converted to SiC, with subsequent offgassing of nitrogen.<sup>84, 101</sup> SiCN derived from linear precursors and therefore having more exclusive  $\text{SiN}_4$  interfacial tetrahedra have been shown to exhibit greater stability against crystallization at high temperatures than SiCN derived from branched precursors.<sup>84, 102</sup>

## 3. The role of BN in SiBCN and other systems

The incorporation of boron has a marked effect on the stability of Si-based polymer-derived ceramics against crystallization and thermal decomposition. SiBCN can withstand temperatures approximately 500 °C greater than its boron-free counterpart without significant mass loss.<sup>93</sup> It was found by Tavakoli, *et al.* through kinetic analysis of experimental data that the increase in B concentration in SiBCN from ~4 at% to ~9 at%

increases the activation energy for crystallization of  $\beta$ - $\text{Si}_3\text{N}_4$  from  $7.8 \pm 0.4$  eV to  $11.5 \pm 0.6$  eV.<sup>98</sup>

It is clear that the BN layers are of critical importance to the thermal stability of SiBCN. The layered BN structure displayed in Figure 11, known as “turbostratic boron nitride” (t-BN), is quite similar to the crystallographic modification hexagonal boron nitride (h-BN) in that it is comprised of 6-fold rings of alternating B and N which stack on top of one another, similarly to graphite. However, it differs from h-BN in that it exhibits rotational asymmetry in the c direction, rendering it not entirely crystalline.<sup>103-104</sup> t-BN can however be crystallized into h-BN.<sup>103</sup>

The marked differences in the crystallization behavior and thermal decomposition of SiCN and SiBCN leads researchers to consider the t-BN as a diffusion barrier in the SiBCN structure.<sup>95, 105-107</sup> The suppression of the procedure of reaction 5 implies that the t-BN phase confines C to its graphite-like structure, rather than permitting it to access the  $\text{SiN}_4$  tetrahedral domains.

The idea of BN as a diffusion barrier is not unique to the topic of SiBCN. Amorphous BN coatings have been deposited on Si/SiGe wafers to allow for the deposition of transition metal dichalcogenides.<sup>108</sup> Hexagonal BN is being investigated as a diffusion barrier to copper in semiconductor interconnects.<sup>109</sup> In fact, uniaxial hot pressing is often performed using graphite dies which are coated in h-BN powder to prevent reaction between the graphite and the sample.<sup>62, 110-111</sup> It is clear that the various forms of hexagonal boron nitride (including t-BN) present unique opportunities in the control of various properties of ceramics.

## E. Silicon Nitride/Boron Nitride Polycrystalline Nanocomposites

In addition to the interesting diffusional effects of BN which are being illuminated, boron nitride also presents an opportunity in the field of fracture. Hexagonal boron nitride nanoplatelets (BNNPs) are of interest to impart multiscale toughening mechanisms to the already tough silicon nitride structure.<sup>112-113</sup> The incorporation of these low-density nanoplatelets at the grain boundaries of  $\text{Si}_3\text{N}_4$  or  $\text{SiAlON}$  may access nanoscale toughening mechanisms, while the characteristic microstructure of  $\text{SiAlONs}$  themselves concomitantly provide the microscale toughening mechanisms mentioned previously (pg. 7).

It was found by Kusunose and coworkers that the chemical synthesis of h-BNNPs from precursors boric acid and urea in a Si<sub>3</sub>N<sub>4</sub> powder blend was possible.<sup>114</sup> The precursors were deposited on the starting powder particle surfaces, reduced for 8 hours in hydrogen, and then heated under nitrogen for 6 hours to produce a blend of α-Si<sub>3</sub>N<sub>4</sub> and t-BN powder. Powder blends were then hot pressed at 1750 °C under 30 MPa of pressure for 1-3 hours. Fourier transform infrared spectroscopy (FTIR) and X-ray diffraction (XRD) revealed that t-BN was converted to h-BN during hot pressing. Resultant samples exhibited an inverse relationship between BN content and elastic modulus, and a slight initial increase in fracture strength at 5 vol% BN followed by a decrease.

Another paper from 2016 reported improvement of fracture toughness, strength, and tribological properties by incorporating exfoliated BNNP powder into the Si<sub>3</sub>N<sub>4</sub> microstructure via a series of planetary ball milling processes.<sup>115</sup> However, the researchers did find evidence of residual porosity due to grain boundary pinning and agglomerated BNNPs in the resultant nanocomposites.

## F. The Fractographic Procedure

Fractography is in essence the study of fracture. It generally consists of a combination of many techniques, including but not limited to observation with the naked eye, optical microscopy, electron microscopy, chemical analysis, CT scanning, and modeling. The goal of the fractographer is to elucidate the cause of the failure of a fractured specimen.<sup>7, 42, 116</sup> Fractography may be performed on specimens fractured in any number of loading configurations and various environments. An illustration of a typical fractographic procedure is found in Figure 12.

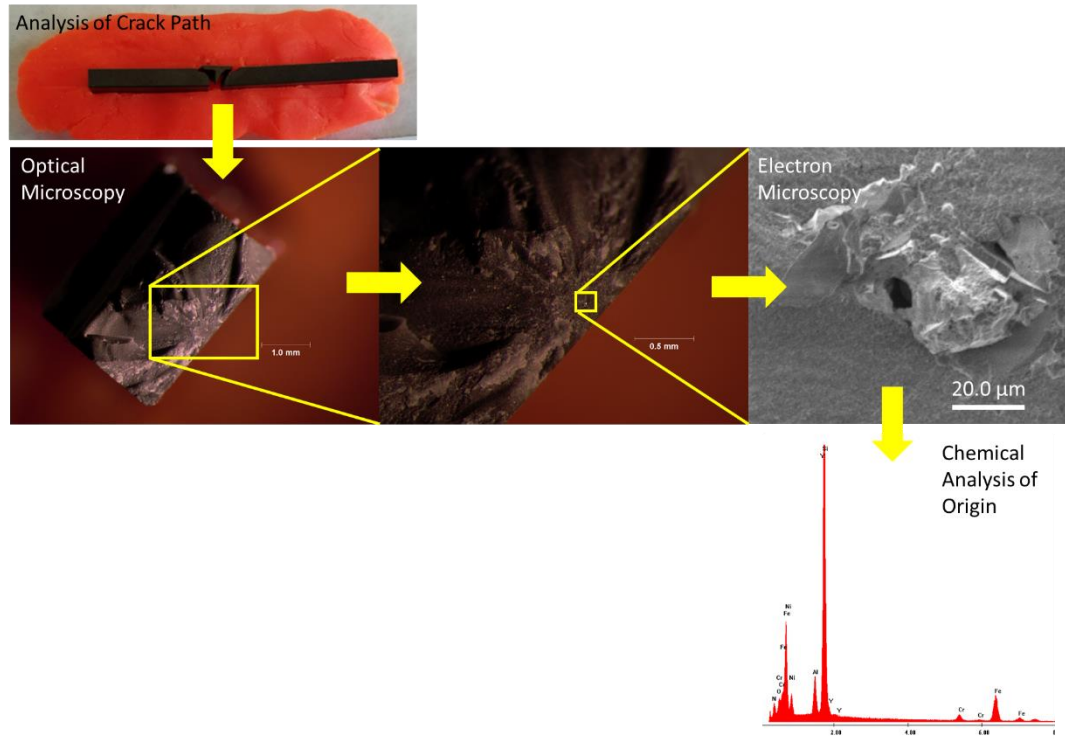


**Figure 12.** A general fractographic procedure for a SiAlON flexure specimen, including observation with the naked eye, optical microscopy, electron microscopy, and chemical analysis of the fracture origin (in this case, an inclusion, likely stainless steel).

The ultimate goal of most fractographic analyses is the elucidation of the fracture origin with the aim to eliminate that flaw population. According to weakest link theory, the linear elastic material will begin to fracture at the weakest point in the sample, or equivalently, at the region of greatest stress concentration. Flaws act as stress concentrators, as is schematically shown in Figure 13, wherein a uniaxial tensile load is being applied to a specimen with a large hole in its center. This flaw induces stress concentration to its left and right.<sup>117-119</sup> If a sufficient stress concentration is developed, fracture will initiate. In brittle materials, crack propagation will proceed very quickly, leading to what is known as “brittle fracture”.

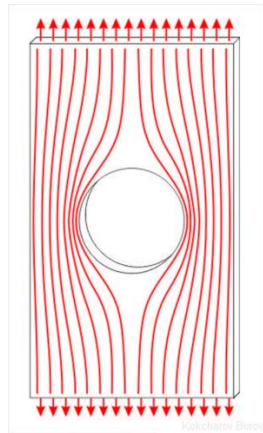


**Figure 13.** Schematic of a specimen with a large hole or flaw, subjected to a uniaxial tensile force. Red lines are known as stress flow lines. The schematic illustrates a concentration of stress on either side of the hole.

If the most severe flaw population is eliminated, then the specimen will exhibit fracture originating at the second-worst flaw, which induces slightly less stress concentration, and consequently, failure stress would increase.<sup>120</sup> As such, fractography is an iterative, investigative process.

### 1. Quantitative fractography and $K_{IC}$

Fractography provides an opportunity to gather quantitative data about the fracture as well, such as the flaw size, fracture mirror size, and critical stress intensity factor ( $K_C$ ). Microscopic methods may be used to measure critical flaw size, which may then be correlated with stress intensity factor by Equation 6:

$$K_{IC} = Y\sigma_f\sqrt{c} \quad (6)$$

where  $K_{IC}$  is the critical stress intensity factor in Mode I crack opening geometry,  $Y$  is a unitless factor accounting for the shape of the flaw (usually between 1 and 2),  $\sigma_f$  is the failure stress, and  $c$  is the flaw size.<sup>7, 121-122</sup> This sort of analysis may allow for the building of databases for specific materials, which can then be used to approach failure in a more predictive, controlled way.

$K_{IC}$  is a very important but elusive parameter of materials. It represents the degree of stress concentration required for crack propagation. High  $K_{IC}$  indicates high resistance to crack propagation, or high “toughness”. For glasses and fine ceramics,  $K_{IC} \approx 1 - 4$

$\text{MPa}\cdot\text{m}^{1/2}$ . The typical toughness range for  $\text{Si}_3\text{N}_4/\text{SiAlON}$  is  $\sim 5 - 8 \text{ MPa}\cdot\text{m}^{1/2}$ . Cast iron has  $K_{IC} \approx 35 - 40 \text{ MPa}\cdot\text{m}^{1/2}$ .<sup>7</sup>

$K_{IC}$  is quite difficult to measure. Several techniques are employed, such as the single-edge notched beam (SENB), single-edge precracked beam (SEPB) experiment, or chevron-notched beam (CNB) experiments. Each of these techniques involves the fabrication of specimens into which controlled flaws have been introduced in order to act as stress concentrators.

The SENB technique involves the formation of a “notch” in the material by the very careful use of a razor blade and diamond paste. However, it had been observed that this technique quite often does not generate a flaw of adequate sharpness or consistency to yield accurate values of  $K_{IC}$  in ceramics.<sup>123-124</sup> Deviations in the notch tip shape or sharpness are observed, and specimens are prone to microcracking in front of the notch tip. SEPB experiments are performed by introducing a crack in the flexure specimen surface, either by indenting in Knoop geometry at low loads (to avoid large complex subsurface damage zones) or by compressing a scratched specimen over a gap. The latter method, which utilizes a “bridge precracker”, allows the Poisson effect to induce small tensile loads on the surface of the sample directly over the gap, or “bridge”.<sup>125</sup> This initiates a small, sharp crack. Crack depths may be measured by die penetration or *post-mortem* fractographic analysis. However, care must be taken that the indentation method does not cause complex microcracking in a large, subsurface damage zone, and the bridge precracker method requires careful monitoring of the precracking procedure using a stethoscope in order to hear when the precrack occurs.<sup>125</sup> Finally, the chevron notch technique requires special specimens to be machined, and low loading rates are typically utilized. If stress-induced corrosion is a concern for the material in question, then the slow loading rate test could be a problem.

For these reasons, there was great interest in the development of a fracture toughness experiment using the lateral cracks induced by a Vickers impression.<sup>126</sup> However, the measurement of the corner crack lengths, the microstructure of the sample, and the equation used to calculate  $K_{IC}$ , of which there have been numerous proposed, all may affect the final result. It is for this reason that the result of an indentation fracture toughness experiment must be described as “indentation crack resistance (ICR)” or

“indentation fracture resistance (IFR)”.<sup>126</sup> For the remainder of this thesis, where ICR values are reported, it is with the understanding that the values are meant to be comparative amongst samples confined to this study, and should not be taken to be true fracture toughness. Procedures for the generation of the Vickers impressions and the measurement of resultant fractures were carefully performed by a single investigator using the same indenter tip each time.

The equation put forth by Niihara, et al. was selected as appropriate for the measurement of silicon nitride ICR under relatively high indentation loads.<sup>127</sup> The relation is found in Equation 7

$$K_C = 0.0421 \frac{E^{0.4} P^{0.6} a^{0.8}}{C^{1.5}} \quad (7)$$

where  $K_C$  is the critical stress intensity factor, E is the elastic modulus, P is the load applied during indentation, a is the half diagonal length of the Vickers impression, and C is the corner crack length *plus* the half diagonal length (a). This can be rewritten as Equation 8

$$\frac{K_{IC}\phi}{H\sqrt{a}} \left( \frac{H}{E\phi} \right)^{0.4} = 0.129 \left( \frac{c}{a} \right)^{-3/2} \quad (8)$$

where H is hardness and  $\phi$  is a constraint factor which is approximately equal to 3. This treatment is limited to the case where the subsurface cracks are median, or “half penny” cracks, extending under the impression from one corner crack tip to the opposite. Niihara points out discrepancy between this equation and experimental data for low C/a ratio (short corner cracks, C/a < ~2), so higher indentation loads are commonly used when performing these experiments to ensure adequately long corner cracks.

## II. MOLECULAR-LEVEL SINTERING ADDITIVES FOR SYNTHESIS OF SIALON CERAMICS

### A. Introduction

The goal of this work was to explore the hypothesis that molecular level additives would enhance the sinterability of silicon nitride-based ceramics. The organometallic precursor aluminum tri *sec*-butoxide was downselected as an Al additive source with the potential to obtain a sub-nanoscale coating on silicon nitride particles. A thorough description of the relevant background information was given previously (pgs 5-15) with a brief summary here.

SiAlONs, as liquid-phase sintered materials, are limited in their high-temperature structural properties by the softening of a residual glassy grain boundary phase which results from the incorporation of liquid-phase sintering additives.<sup>128</sup> As mentioned previously, it is therefore common to reduce the sintering additive volume as much as possible while still facilitating full densification. The advent of nanomaterials and the recent learnings in the field of molecular precursors and polymer-derived ceramics are opening doors to the application of novel sintering additives, which must be as comprehensively understood as are the conventional powder additives.<sup>129</sup>

As highly covalent ceramics, the self-diffusivity in  $\text{Si}_3\text{N}_4$  is very low, and temperatures in the range of 1850 °C are required to facilitate atomic diffusion. However, in this temperature range, pure  $\text{Si}_3\text{N}_4$  will decompose into its constituent elements.<sup>39, 47</sup> Therefore, it is necessary to increase atomic diffusion at temperatures below the decomposition temperature. This is commonly accomplished by introducing solute atoms into the  $\text{Si}_3\text{N}_4$  lattice which decrease the covalency of the system. Common additives are  $\text{Al}_2\text{O}_3$  and  $\text{AlN}$  powders, the incorporation of which results in what is known as a SiAlON. In SiAlONs, Al substitutes on the Si site and O on the N site in a 1:1 ratio, requiring that these solute atoms are incorporated in such a ratio. However, solid solution via these powder additives is associated with relatively long diffusion lengths by virtue of their particulate nature.

It would be highly beneficial to distribute solute atoms as finely as possible throughout the nanoscale powder blends. Finely distributed additives such as nanoparticles

are thought to be more reactive, owing to their small size and consequent high surface-to-volume ratios.<sup>130-131</sup> Additionally, very small particles distributed in a coarser-grained matrix would inherently present shorter diffusion lengths between themselves and the matrix particles. In the extreme case, individual solute atoms distributed over the surfaces of the silicon nitride particles would present the least stable case with the shortest possible diffusion lengths. The molecular route to fine-scale distribution is also more promising and feasible than the nanoparticle route because nanoparticles tend to agglomerate due to their high surface-to-volume ratio, which makes their uniform distribution a challenge.

This work demonstrates the successful implementation of an organometallic precursor for the incorporation of Al and O in the Si<sub>3</sub>N<sub>4</sub> lattice and subsequent synthesis of SiAlON ceramics.<sup>132</sup> X-ray diffraction (XRD), thermogravimetric analysis (TGA), differential thermal analysis (DTA), surface area measurements, energy dispersive spectroscopy (EDS), and high-temperature scanning electron microscopy (HTSEM) are utilized in order to elucidate the nature of the decomposition of the organometallic precursor. The solid solution of Al and O in the Si<sub>3</sub>N<sub>4</sub> lattice is evaluated by Rietveld refinements.

## B. Materials and Methods

Two SiAlON powder blends were generated using starting materials  $\alpha$ -silicon nitride (UBE SNE-10, <5 wt%  $\beta$  phase, UBE, Japan), aluminum nitride ( $D_{50} = 8 \mu\text{m}$ , Alfa Aesar, USA), aluminum oxide (A-16 SG, Almatis GMBH, Germany), aluminum tri *sec*-butoxide (97%, Sigma Aldrich, USA), and yttrium oxide (99.99%, 18-38 nm, Nanografi Nanotechnology, Turkey). Information on impurities can be found in Table I.

**Table I. SiAlON Starting Material Specifications (- indicates not reported or applicable)**

Material	Si <sub>3</sub> N <sub>4</sub>	AlN	Al <sub>2</sub> O <sub>3</sub>	ASB	Y <sub>2</sub> O <sub>3</sub>
Manufacturer	UBE	Alfa Aesar	Almatis	Millipore	Nanografi
Product	SN-E10	11546	A 16 SG	201073	NG04SO3701
d <sub>10</sub> , d <sub>50</sub> , d <sub>90</sub> (μm)	0.3, 0.7, 1.75	0.9, 8, 20	-, 0.5, 2	NA	18-38 nm
Purity	α phase > 95 wt%	N 32.0% min	99.8%	97%	99.99%
O	< 2.0 wt%	0.7 wt%	-	-	-
C	0.1 wt%	-	-	-	-
Fe	10 ppm	0.001 wt%	-	-	-
Cl	< 100 ppm	-	-	-	-
Ca	< 1 ppm	-	-	-	-
Al	1 ppm	-	-	10.9 wt%	-
Na <sub>2</sub> O	-	-	0.07 wt%	-	-
Fe <sub>2</sub> O <sub>3</sub>	-	-	0.02 wt%	-	< 13 ppm
MgO	-	-	0.05 wt%	-	-
SiO <sub>2</sub>	-	-	0.03 wt%	-	< 23 ppm
CaO	-	-	0.02 wt%	-	< 12 ppm
B <sub>2</sub> O <sub>3</sub>	-	-	<0.005 wt%	-	-

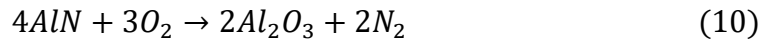
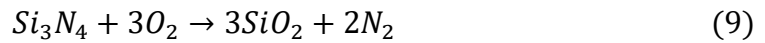
The liquid organometallic precursor ASB was extracted in a glove box under continuously purified high-purity N<sub>2</sub>, sealed, and removed from the glovebox. It was then quickly dissolved in anhydrous isopropanol suspension medium (99.5%, Sigma Aldrich, USA) to shield it from the atmosphere directly before incorporating powder constituents. The goal is to prevent the hydrolysis and polycondensation reactions discussed previously (pg. 16) and retain the fine-scale molecular network containing Al and O.

Powders were ball milled in anhydrous isopropanol using 1 L high-density polyethylene jars charged with approximately 1.5 kg of ZrO<sub>2</sub> spheres (YTZ, 10 mm diameter, Tosoh, Japan) for 24 hours. The base compositions are tabulated in Table I. Powder blends are identified by their yttria level added *on top of* the base composition (Si<sub>3</sub>N<sub>4</sub>, AlN, and either Al<sub>2</sub>O<sub>3</sub> or ASB) as well as whether they contained alumina powder or ASB. For example, 2YASB indicates that the blend contains Y<sub>2</sub>O<sub>3</sub> in a concentration of 2 wt% on top of the base composition and ASB rather than Al<sub>2</sub>O<sub>3</sub>. 0, 2 and 4 wt% Y<sub>2</sub>O<sub>3</sub> concentrations were investigated.

**Table II. SiAlON Powder Blend Compositions with Raw Materials in wt%. Note: ASB denotes aluminum tri *sec*-butoxide, an Al alkoxide**

	<b>Si<sub>3</sub>N<sub>4</sub></b>	<b>AlN</b>	<b>Al<sub>2</sub>O<sub>3</sub></b>	<b>ASB</b>
<b>Al<sub>2</sub>O<sub>3</sub> Blends</b>	92.13	5.05	2.82	0
<b>ASB Blends</b>	83.15	4.55	0	12.30

The calculation of a SiAlON powder blend must account for oxygen incorporated (and nitrogen lost) by the oxidation of  $\alpha$ -Si<sub>3</sub>N<sub>4</sub> and AlN powders. The oxidation reactions for these two materials can be found in Equations 9<sup>133</sup> and 10<sup>134</sup>.



From these oxidation reactions, it can be seen that the exchange of N for O does not occur in a 1:1 ratio. Therefore, the Si<sub>3</sub>N<sub>4</sub> and AlN starting materials in a SiAlON blend can in fact be considered to be Si<sub>3</sub>O<sub>x</sub>N<sub>4-(2/3)x</sub> and AlO<sub>y</sub>N<sub>1-(2/3)y</sub>. Results of this oxidation analysis for  $\beta'$ -SiAlON (Si<sub>6-Z</sub>Al<sub>Z</sub>O<sub>Z</sub>N<sub>8-Z</sub>) are given in Equations 11, 12, 13, and 14. For a targeted Z value and a known (or assumed) concentration of O in the Si<sub>3</sub>N<sub>4</sub> and AlN powders (x and y, respectively), the appropriate molar ratios of silicon nitride, aluminum nitride, and aluminum oxide can be calculated using Equations 11, 12, and 13.

$$Si_3O_xN_{4-(2/3)x} Powder: 2 - (1/3)Z \quad (11)$$

$$AlO_yN_{1-(2/3)y} Powder: \frac{2x(Z-6)-3Z}{6y-9} \quad (12)$$

$$Al_2O_3 Powder: \frac{1}{2}Z - \frac{2x(Z-6)-3Z}{12y-18} \quad (13)$$

The sum of O will always be Z, as per the  $\beta'$ -SiAlON formula. If Al<sub>2</sub>O<sub>3</sub> is replaced by ASB, the expressions for silicon nitride and aluminum nitride may remain unchanged, while the expression for ASB will simply be twice that for Al<sub>2</sub>O<sub>3</sub> powder, as demonstrated by Equation 14.

$$ASB: Z - \frac{2x(Z-6)-3Z}{6y-9} \quad (14)$$

This treatment omits any oxygen scavenged from the atmosphere by the ASB during batching. Note that ASB blends will be slightly oxygen-rich, owing to the 3:1 ratio of O to Al in the ASB molecule, in comparison to the 3:2 ratio of O and Al in Al<sub>2</sub>O<sub>3</sub>. However, as

the defect equation (Eq. 1) for  $\beta'$ -SiAlON requires a 1:1 ratio of Al and O in the  $\text{Si}_3\text{N}_4$  lattice, it is assumed that excess O remains in the grain boundary. In this work, it was assumed that  $\text{Si}_3\text{N}_4$  contains 3 wt%  $\text{SiO}_2$  and AlN contains 2 wt%  $\text{Al}_2\text{O}_3$  based on literature values.<sup>69</sup>

Milled suspensions were dried at 80 °C in a Buchi R-300 rotoevaporator. Densification was carried out in a Thermal Technology uniaxial hot press (HP50, Thermal Technology, USA) in 1 inch diameter boron nitride-lined graphite dies (see Figure 14) at 1760 °C under a pressure of 20 MPa. The temperature range 20-500 °C was traversed under vacuum ( $\sim 5 \times 10^{-4} - 5 \times 10^{-5}$  torr), and a static charge of approximately 780-800 torr of nitrogen was introduced into the chamber at 500 °C.



**Figure 14. 1-inch inner diameter graphite die used for uniaxial hot pressing. Dies were lined with graphite foil of 0.005 inch thickness which was spray coated with aerosolized hexagonal boron nitride.**

Hot pressed specimens were machined using a vertical end mill and diamond tool before analysis in order to remove any surface reaction layer. Machining was carried out with a target cut depth of 0.003 inches per pass, a feed rate of 3 inches per minute, and a final pass rotational speed of 5000 rpm.

Specific surface area was measured by the 11-point BET nitrogen adsorption method in a Micromeritics Gemini VII Surface Area Analyzer (Micromeritics, USA). BET powder samples were heat treated at 150 °C for 12 h in a Centurion Q50 dental furnace in alumina crucibles under flowing ultrahigh purity nitrogen (UHP N<sub>2</sub>) before being degassed at 150 °C for 90 min in a Micromeritics FlowPrep 060 Sample Degas System. This 2-step degas procedure was adopted due to the observation that ASB blends tended to contain a significant amount of moisture, which clung to the sides of the BET sample tube during a conventional 90-minute degassing procedure.

Density was measured via the immersion method in deionized water at room temperature under the guidance of ASTM C-830.<sup>135</sup> “Zero-strain” elastic modulus was measured by the pulse echo technique.<sup>136</sup> Thermogravimetric analysis (TGA) was performed using a TA Instruments Q-600 STA Thermal Analyzer in alumina crucibles under flowing UHP N<sub>2</sub> with a flow rate of 30 mL/min. Energy Dispersive Spectroscopy (EDS) mapping was carried out on a JEOL JSM-6010PLUS/LA Scanning Electron Microscope, and high-temperature scanning electron microscopy (SEM) was conducted on a JEOL JSM-7800F Field Emission Scanning Electron Microscope. Special powder blends without AlN were prepared for EDS mapping and high-temperature SEM so that the Al from ASB could be detected without additional response from Al in AlN.

Powder samples were taken for heat treatment, which was performed in an alumina tube furnace under flowing UHP N<sub>2</sub> in quartz crucibles. X-ray diffraction (XRD) of densified SiAlONs was performed on a Bruker D2 Phaser benchtop diffractometer (Bruker, USA) with Cu $\alpha$  radiation (1.5406 Å) on surfaces polished to 1 μm. Phase identification was performed using the program Diffrac.Eva, and Rietveld refinements were performed in the program Topas (V6, Bruker, USA).

### C. Results and Discussion

It was important in this work to determine if the treatment with ASB provided a molecular or nanoscale addition of Al and to observe the distribution of Al in the powder blends. Y<sub>2</sub>O<sub>3</sub>-free powder blends were characterized by BET in order to compare specific surface areas of SiAlON blends containing ASB and Al<sub>2</sub>O<sub>3</sub>. It was found that the baseline SiAlON blend (0YAl<sub>2</sub>O<sub>3</sub>) had a specific surface area of 12.90 ± 0.05 m<sup>2</sup>/g, while a BET

surface area of  $30.6 \pm 0.2 \text{ m}^2/\text{g}$  was measured for the experimental alkoxide SiAlON blend (0YASB). This significant increase in specific surface area of 137% is an indication that the organometallic additive was finely distributed, likely as a low-density coating on the  $\text{Si}_3\text{N}_4$  particles. SEM micrographs of the two parent powder blends can be found in Figure 15. The cloudy, non-particulate appearance of the ASB-containing sample (Figure 15a) can be compared to the non-ASB treated sample (Figure 15b). This corroborates the BET data indicating high surface area for ASB-containing powders.

After heating to 500 °C under vacuum, the specific surface area of 0YASB was reduced to  $15.06 \pm 0.07 \text{ m}^2/\text{g}$ . This may be attributed to the thermal decomposition and loss of alkyl groups from the organometallic precursor. There are reports which indicate that the pyrolytic decomposition of aluminum alkoxides results in the production of olefins, which are unsaturated hydrocarbons, though alternative reaction pathways have been proposed.<sup>137-138</sup>

Micrographs of the powder blends after heat treatment are found in Figure 16. The ASB-SiAlON powder blend exhibits distinct particles, in contrast to its morphology before heat treatment (Fig. 15a). The observed particles are from the original powders ( $\text{Si}_3\text{N}_4$ , AlN). The following TGA/DTA, EDS and XRD analysis confirm that the ASB derived Al did not form particulates.

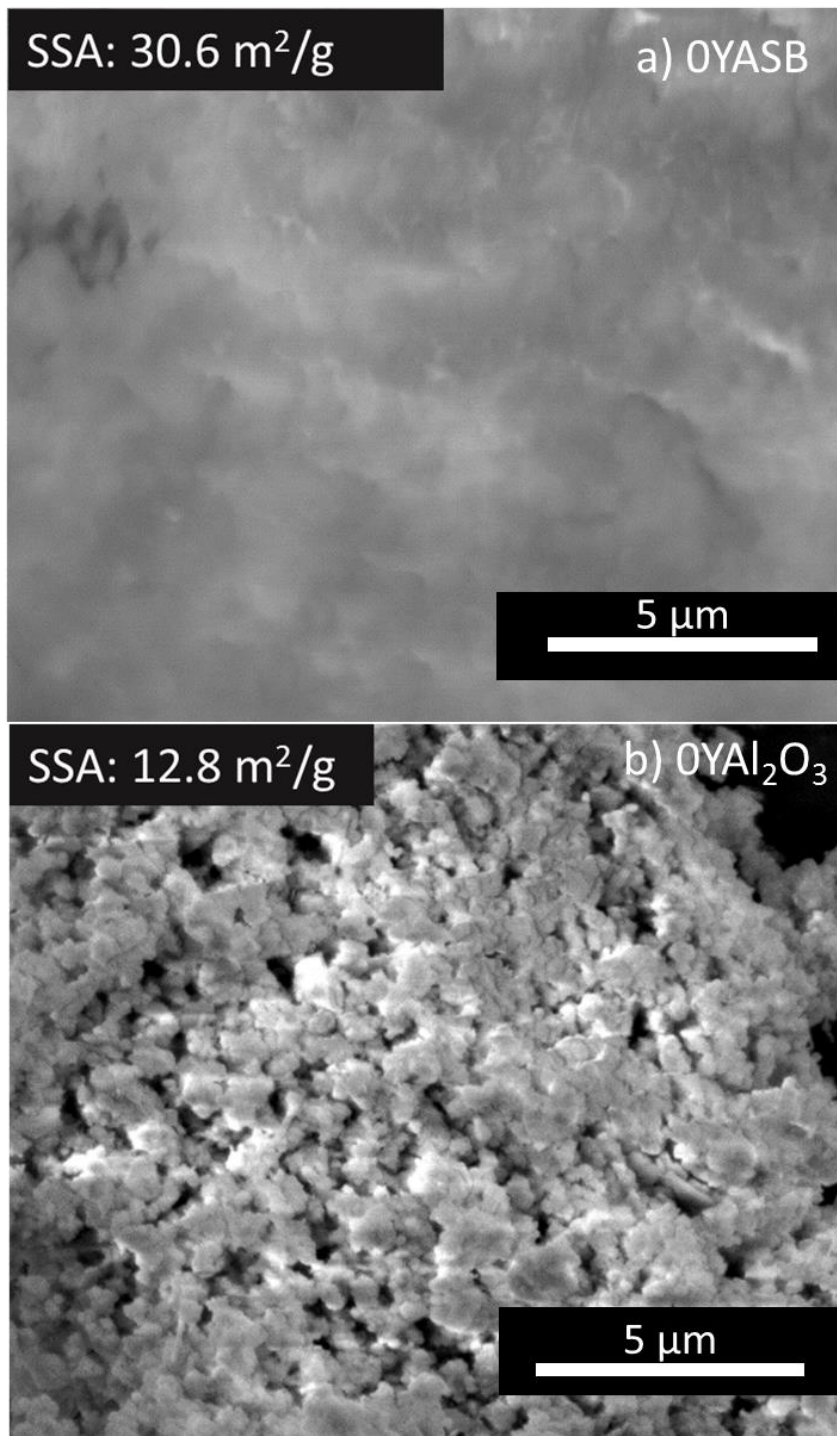


**Figure 15.** SEM micrographs of a) Al organometallic-containing SiAlON powder blend (OYASB and b) conventional Al<sub>2</sub>O<sub>3</sub>-containing SiAlON powder blend (OYAl<sub>2</sub>O<sub>3</sub>) with corresponding measured BET specific surface areas.

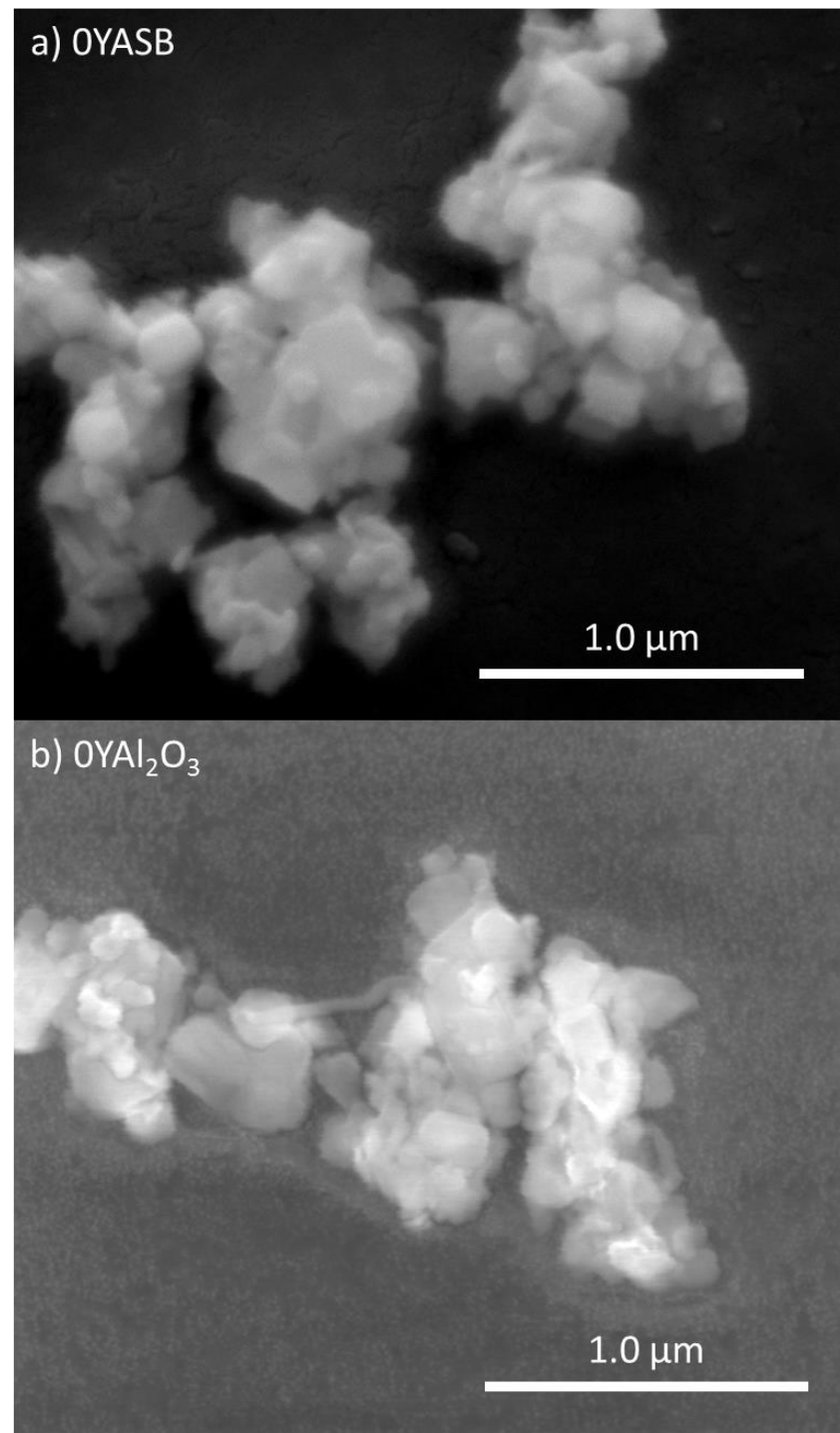


**Figure 16.** SEM micrographs of a) organometallic-containing powder blend (0YASB), and b) conventional Al<sub>2</sub>O<sub>3</sub>-containing powder blend (0YAl<sub>2</sub>O<sub>3</sub>) after heat treatment. Decomposition of the ASB organometallic reveals discernable particles.

Thermogravimetric analysis (TGA) was performed up to 1000 °C to explore the thermal decomposition of the organic precursor during the sintering cycle. Figure 17 compares the mass loss of SiAlON powder blends with the organometallic precursor (0YASB) and with Al<sub>2</sub>O<sub>3</sub> (0YAl<sub>2</sub>O<sub>3</sub>). The organometallic sample 0YASB exhibited 6.7 wt% loss compared to <1 wt% for the alumina-containing blend.

If one assumes that during pyrolytic decomposition of ASB ( $C_{12}H_{27}AlO_3$ ) in the SiAlON blend, i) all C and H are removed, ii) all Al and O remain in the system, and iii) there is no other mechanism for mass loss, then one should expect a mass loss of ~8.6%. Worthy of note are previous reports of the evolution of oxygen-bearing pyrolytic byproducts during thermal decomposition of vaporous ASB, such as 2-butanol and 2-butanone, in chemical vapor deposition (CVD) experiments.<sup>139</sup>

The mass loss of the ASB-containing SiAlON blend 0YASB was ~7%, somewhat less than the 8.6% expected from removal of alkyl groups only. It is likely that the more volatile byproducts of ASB decomposition were removed during drying of the milled suspension at 80 °C.

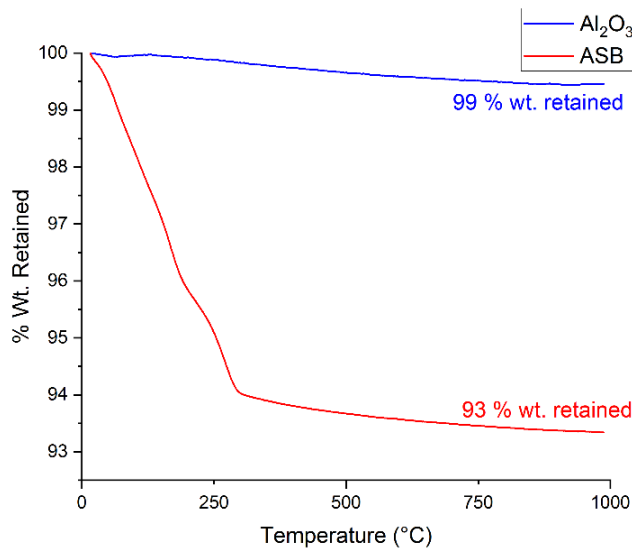


**Figure 17.** TGA mass loss curves comparing SiAlON blends containing alumina powder (0YAl<sub>2</sub>O<sub>3</sub>) and Al alkoxide additive (0YASB). The mass loss of the alumina-containing blend was <1 wt% on heating to 1000 °C, while the ASB-containing blend lost 6.7 wt% mass.

The differential thermal analysis (DTA) for the above ASB-SiAlON blend is found in Figure 18. This analysis shows a broad endothermic region between room temperature and approximately 300 °C, attributed to volatilization of organic species. No significant exotherms are detected, indicating that there are no crystallization events. This implies that the ASB loses alkyl groups, but does not crystallize up to 1000 °C.

The important combination of DTA and EDS data provides preliminary indication that a molecular level Al-containing additive may have been effectively applied to the particle surfaces.

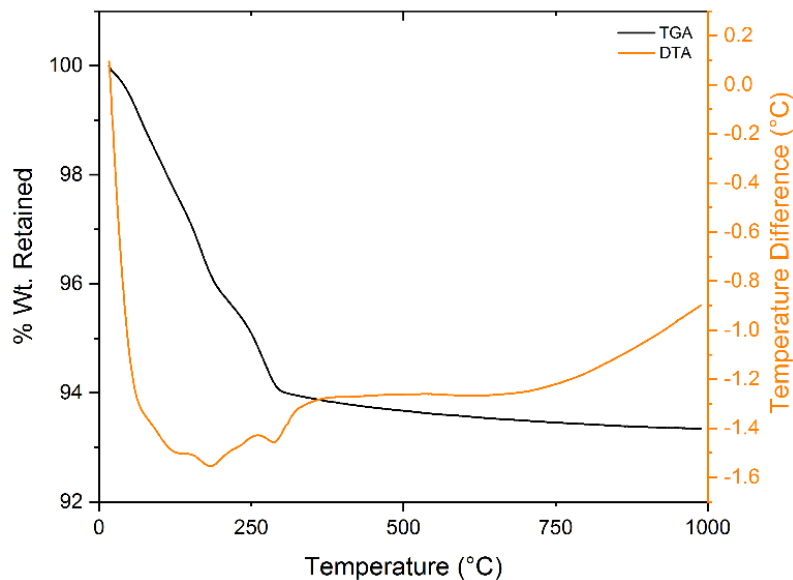


**Figure 18. TGA/DTA curves for Al alkoxide additive SiAlON powder blend (0YASB).**  
**DTA reveals a broad endothermic region between 20 and ~300 °C,**  
**attributed to volatilization of organic species and moisture. No exotherms**  
**detected (indicating no crystallization).**

As previously mentioned (pg. 32), EDS mapping was performed on powder blends which did not contain AlN so that the Al from the ASB or Al<sub>2</sub>O<sub>3</sub> was not confused with the Al from AlN. Figure 19 highlights two representative Al EDS maps, one from the Al<sub>2</sub>O<sub>3</sub> blend and one from the ASB blend. As expected, the Al<sub>2</sub>O<sub>3</sub> map shows evidence of discrete alumina particles. In contrast, the ASB map appears to show a homogeneous distribution of Al across the silicon nitride particles. Further, EDS mapping of the same ASB powder

blend heated to 1000 °C in a quartz crucible under flowing UHP N<sub>2</sub> exhibits similarly homogeneous Al distribution, as can be seen in Figure 20. This indicates successful retention of an extremely fine-scale, homogeneous distribution of solute atoms Al and O, supporting the conclusion that a molecular level additive can be applied by avoiding hydrolysis and polycondensation of the alkoxide and instead inducing thermal decomposition.

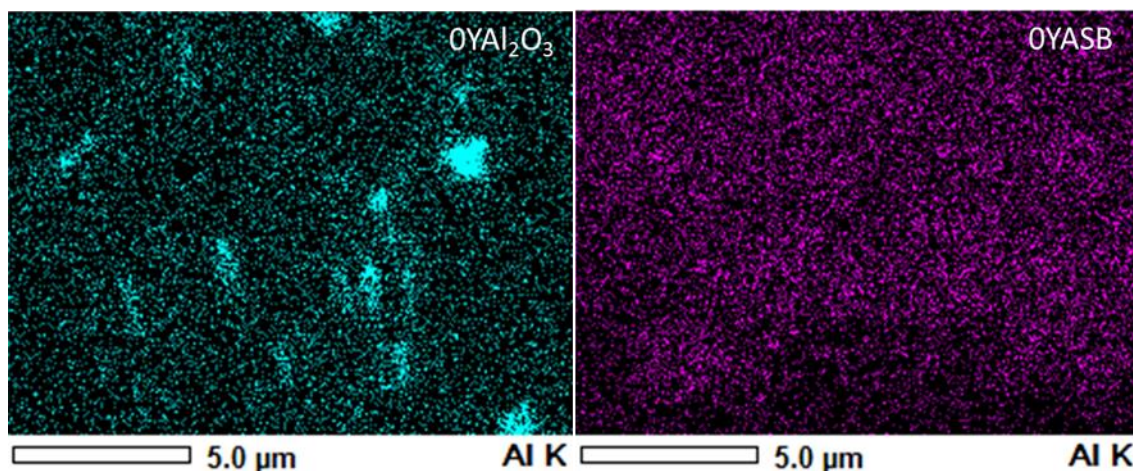


**Figure 19.** Aluminum EDS maps comparing SiAlON blends containing a) alumina powder (0YAl<sub>2</sub>O<sub>3</sub>) with b) Al alkoxide additive (0YASB). The alumina-containing powder blend exhibits regions of high Al concentration, attributed to Al<sub>2</sub>O<sub>3</sub> particles; ASB-containing blend exhibits a significantly more homogeneous distribution of Al.

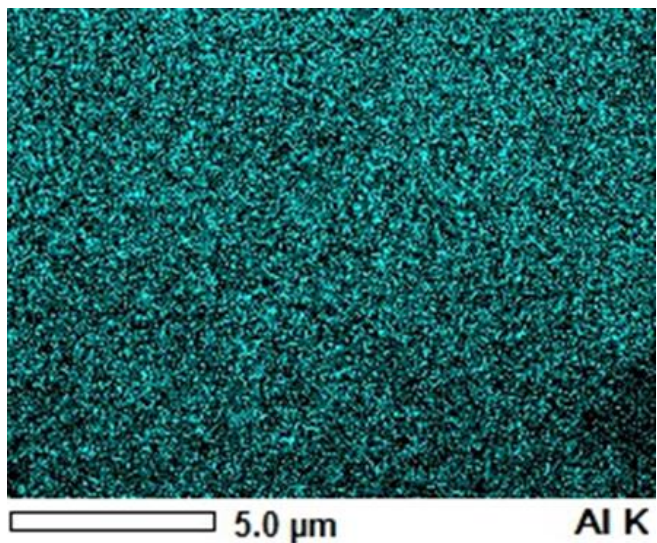


**Figure 20.** Aluminum EDS map of SiAlON powder blend with Al alkoxide (0YASB) heat treated to 1000 °C for 1 h in flowing UHP N<sub>2</sub>. The distribution of Al appears to remain homogeneous even after the decomposition of the organic precursor.

Heating to 500 °C in an SEM yielded no discernable morphological changes, as can be seen in Figure 21, in which micrographs before heating, at 500 °C, and after cooling are presented. This result, combined with the EDS map supporting a homogeneous distribution of Al even after heating to 1000 °C and the lack of exotherms detected by DTA, is strong evidence that formation of Al<sub>2</sub>O<sub>3</sub> crystallites on heating the ASB blends does not occur. The measured decrease in specific surface area from 30.6 to 15.1 m<sup>2</sup>/g (Figure 15a and Figure 16) is therefore attributed to the loss of high surface area organic material on the Si<sub>3</sub>N<sub>4</sub> particles.

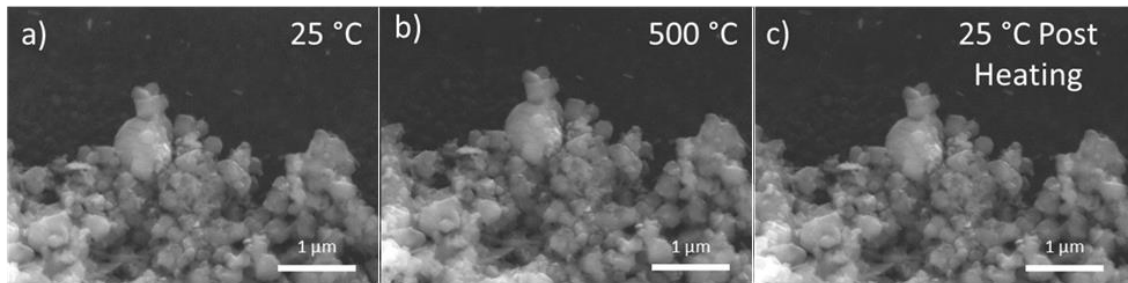


**Figure 21.** Secondary electron micrographs of 0YASB at a) room temperature, b) 500 °C, and c) room temperature after cooling from 500 °C. No morphological differences were detected, indicating the lack of widespread  $\text{Al}_2\text{O}_3$  crystallization of the ASB on heating to 500 °C.

XRD analysis also corroborates the lack of crystallization of  $\text{Al}_2\text{O}_3$  in the organometallic powder blend 0YASB. Figure 22 shows the XRD patterns for 0YASB as-blended, after 500 °C heat treatment in vacuum, and after 1000 °C under flowing UHP N<sub>2</sub>. The only difference in the diffraction patterns of these three is the increased relative intensity of the  $\text{ZrO}_2$  peak near 30 °2θ, which arises from impurities introduced by ball milling.

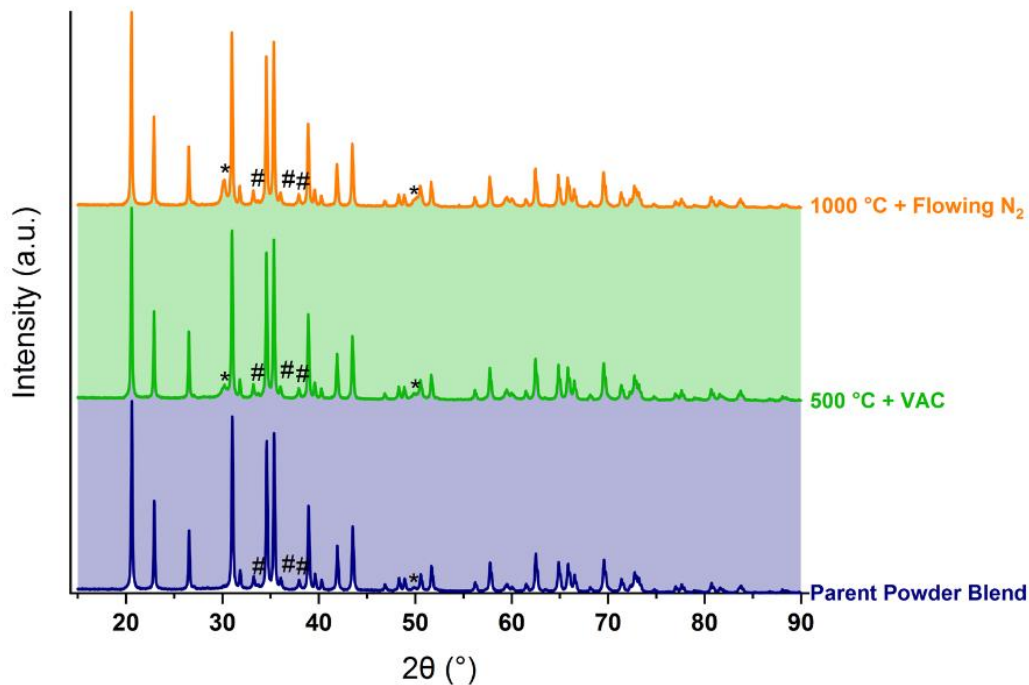


**Figure 22.** XRD Patterns of 0YASB powder as-blended, after heating to 500 °C in a vacuum, and after heating to 1000 °C in flowing nitrogen. \*: ZrO<sub>2</sub> (PDF 01-079-1763) #: AlN (PDF 00-066-0534) Unlabeled peaks:  $\alpha$ -Si<sub>3</sub>N<sub>4</sub> (PDF 04-001-1514)

There is evidence in the literature of the formation of alumina structures known as “transition aluminas” through hydrothermal synthesis involving many different Al-containing organometallics.<sup>138</sup> Specifically, aluminum tri *sec*-butoxide and aluminum isopropoxide have been shown to yield  $\gamma$ -Al<sub>2</sub>O<sub>3</sub> by hydrothermal synthesis at 300 °C. This alumina structure is characterized by a sharp XRD peak at approximately 42.5 °2θ. However, a slow scan across the 2θ range of 40-45 °2θ did not indicate the presence of this phase in organometallic-bearing 0YASB heat treated at 500 °C in vacuum. The resultant diffraction pattern is presented in Figure 23, in which the only phase indicated is  $\alpha$ -Si<sub>3</sub>N<sub>4</sub>.

The cumulation of these analyses provides substantial evidence that the thermal decomposition of an Al organometallic precursor in the absence of water (preventing

hydrolysis and polycondensation) is an effective method of applying a uniform molecular level or sub-nanoscale additive to silicon nitride powder.

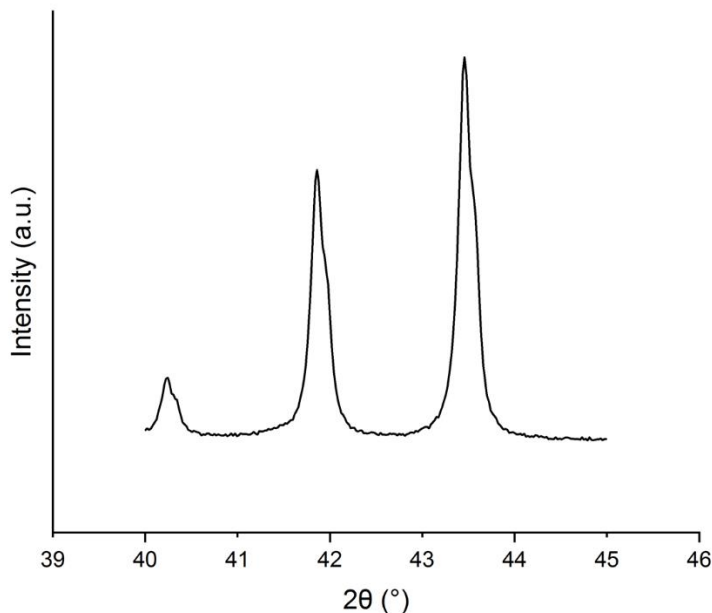


**Figure 23.** XRD Slow scan of 0YASB after heat treatment to 500 °C in a vacuum in search of evidence of  $\chi$ -Al<sub>2</sub>O<sub>3</sub>. No peak at 42.5 °2θ was observed, indicating that this transition alumina is not present in detectable volumes.

The final densities of the hot pressed powder blends are summarized in Figure 24. It was found that the density of the ASB-SiAlON was comparable to that of the Al<sub>2</sub>O<sub>3</sub> sample at moderate (4 wt%) Y<sub>2</sub>O<sub>3</sub> concentrations. However, when the system was starved of Y<sub>2</sub>O<sub>3</sub>, the ASB sample exhibited higher density than Al<sub>2</sub>O<sub>3</sub> samples. The Al and O solid solution results in an overall increase in the ionicity of the system and is described as “lattice softening”.<sup>140</sup> This effect acts in tandem with the liquid phase to facilitate densification. This supports the original hypothesis that the molecular level or sub-nanoscale, homogeneous distribution of solute atoms in ASB blends enhances the dissolution of Al and O in the Si<sub>3</sub>N<sub>4</sub> lattice. This is extremely significant for the fabrication of high-temperature creep-resistant SiAlON ceramics with lower levels of liquid phase sintering additives (e.g. lower Y<sub>2</sub>O<sub>3</sub> concentrations).

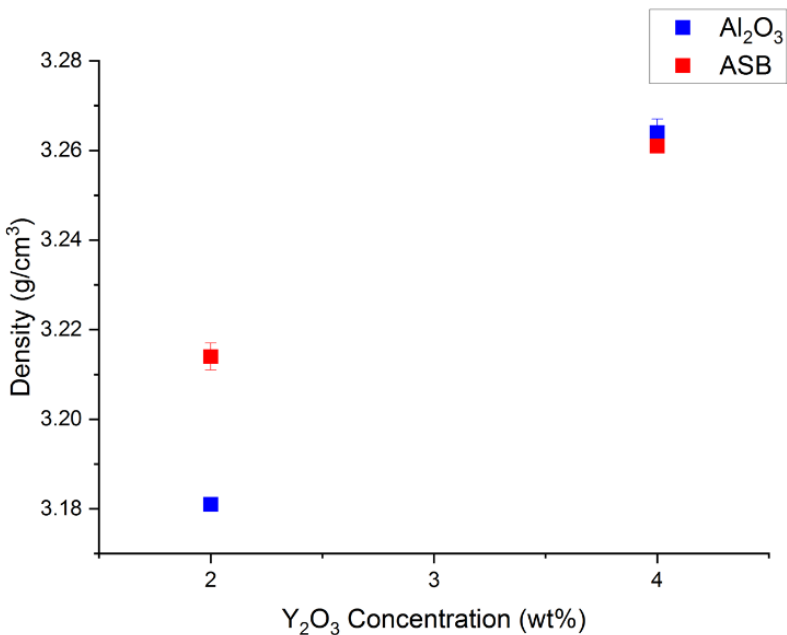


**Figure 24.** Immersion densities of sintered SiAlONs. At 4 wt%  $\text{Y}_2\text{O}_3$ , samples converge to the same density. When the  $\text{Y}_2\text{O}_3$  concentration is decreased, the ASB sample exhibits a higher density. Error bars represent the statistical uncertainty of the measurement technique, based on the resolution of the instruments used and the number of measurements performed.

It has been well-documented that the SiAlON solid solution is accompanied by a lattice expansion.<sup>69</sup> Rietveld refinements of a series of samples sintered using varying dwell times were performed as a way to investigate the degree of solid solution of Al and O in the  $\text{Si}_3\text{N}_4$  lattice. Results seem to indicate higher unit cell volumes in SiAlONs sintered using ASB than in conventional  $\text{Al}_2\text{O}_3$  SiAlONs for all dwell times. Interestingly, both types of SiAlONs exhibit a general trend of decreasing unit cell volume with increasing dwell time. These results are summarized in Figure 25, and indicate that even at very low dwell times, ASB may be facilitating more effective solid solution of Al and O in the  $\text{Si}_3\text{N}_4$  lattice.

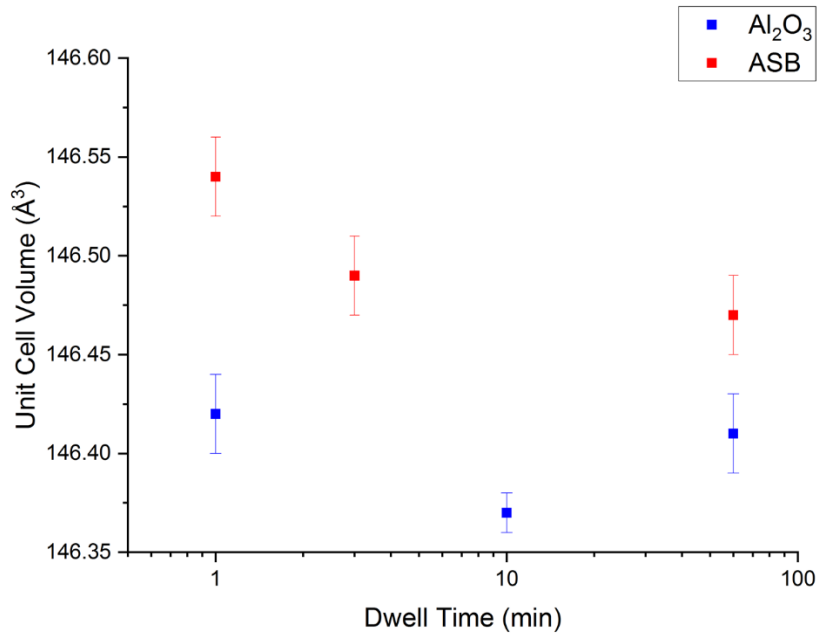


**Figure 25.** Unit cell volumes of  $\beta'$ -SiAlONs sintered with 4 wt%  $\text{Y}_2\text{O}_3$  for various dwell times. Unit cell volumes are greater in SiAlONs sintered using ASB than those sintered with  $\text{Al}_2\text{O}_3$ , indicating enhanced solid solution of Al and O in the  $\text{Si}_3\text{N}_4$  lattice.

Lattice refinements were also performed for the SiAlONs sintered with very low concentrations of  $\text{Y}_2\text{O}_3$  (2 wt%) sintering additive. These results can be found in Figure 26. For both  $\text{Y}_2\text{O}_3$  concentrations the ASB specimen yielded greater unit cell volume. Interestingly, unit cell volume for both types of SiAlONs decreased with increasing liquid phase volume. This may be tentatively explained from the standpoint of Al and O solubility in the glassy phase generated by  $\text{Y}_2\text{O}_3$ . A greater volume of glass would be able to dissolve a greater volume of Al and O, rather than those solute atoms entering the  $\text{Si}_3\text{N}_4$  lattice.

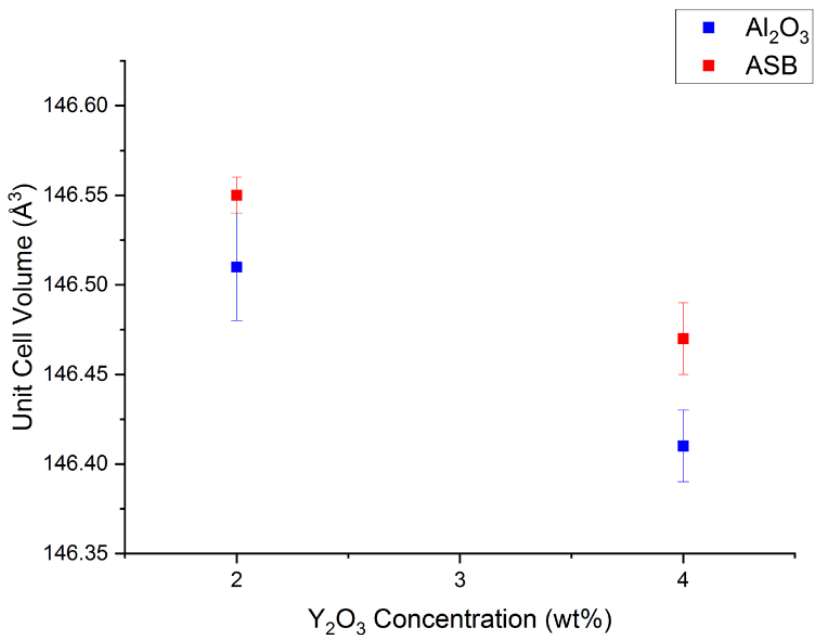


**Figure 26.** Unit cell volumes of ASB- and  $\text{Al}_2\text{O}_3$ -containing SiAlONs at 4 wt%  $\text{Y}_2\text{O}_3$  (common concentration) and 2 wt%  $\text{Y}_2\text{O}_3$  (very low concentration). ASB SiAlONs exhibit higher unit cell volumes for both concentrations. SiAlON unit cell volume decreases with increasing liquid phase additive concentration.

Finally, lattice parameters for both  $\text{Al}_2\text{O}_3$ - and ASB-derived SiAlONs were compared with literature values for hot isostatically pressed (HIP) SiAlONs.<sup>69</sup> These results can be found in Figure 27. It was observed that the lattice parameters decrease with increasing  $\text{Y}_2\text{O}_3$  concentration, which provides further evidence that the glassy grain boundary phase dissolves some of the Al and O rather than allowing it to enter the  $\text{Si}_3\text{N}_4$  lattice. Consequently,  $\text{Si}_{5.5}\text{Al}_{0.5}\text{O}_{0.5}\text{N}_{7.5}$  actually has slightly different stoichiometry for SiAlONs synthesized via both the powder additive route as well as the liquid organometallic route if a liquid phase sintering additive is incorporated. Overall, the lattice parameters of SiAlONs in the present work appear to be relatively consistent with literature values, and follow a similar trend as a function of liquid phase sintering additive concentration.

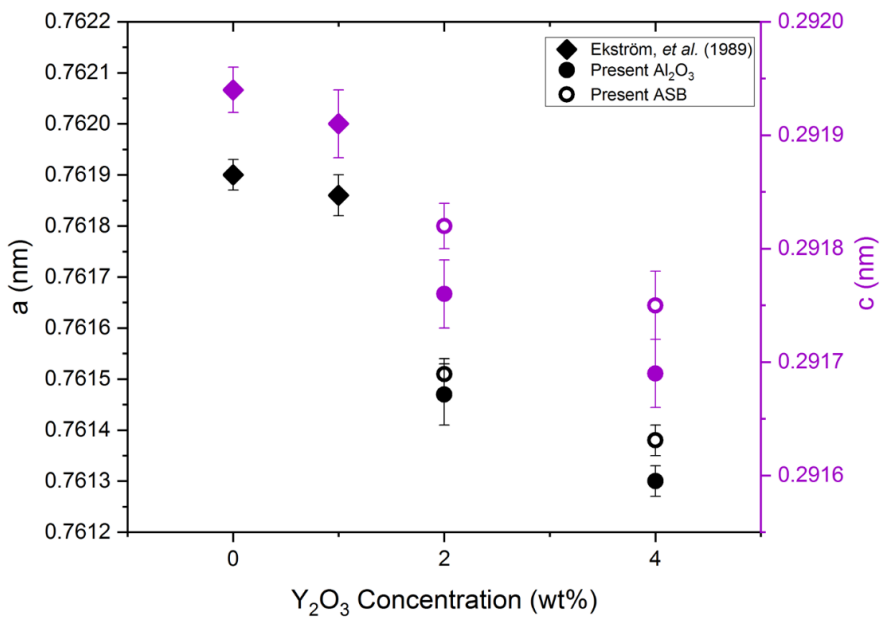


**Figure 27.**  $a$  and  $c$  lattice parameters for  $\beta'$ -SiAlON as a function of  $\text{Y}_2\text{O}_3$  concentration. Filled and open circles are SiAlONs from the present work, derived from  $\text{Al}_2\text{O}_3$  powder and ASB, respectively, while the diamonds correspond to the SiAlONs synthesized by Ekström, *et al.*<sup>69</sup> Black data points correspond to  $a$  lattice parameters, and purple points correspond to  $c$  lattice parameters.

The pulse echo technique is a nondestructive method for assessing the zero-strain elastic modulus of materials. In this work, it appears that there was no significant difference between the elastic moduli of SiAlONs sintered using  $\text{Al}_2\text{O}_3$  and ASB. This is illustrated in Figure 28, in which the error bars represent the statistical measurement uncertainty of the technique. Note that elastic modulus did in fact decrease slightly with decreasing  $\text{Y}_2\text{O}_3$  content, which may largely be attributed to the lower density, or higher porosity, of  $\text{Y}_2\text{O}_3$ -deficient samples.

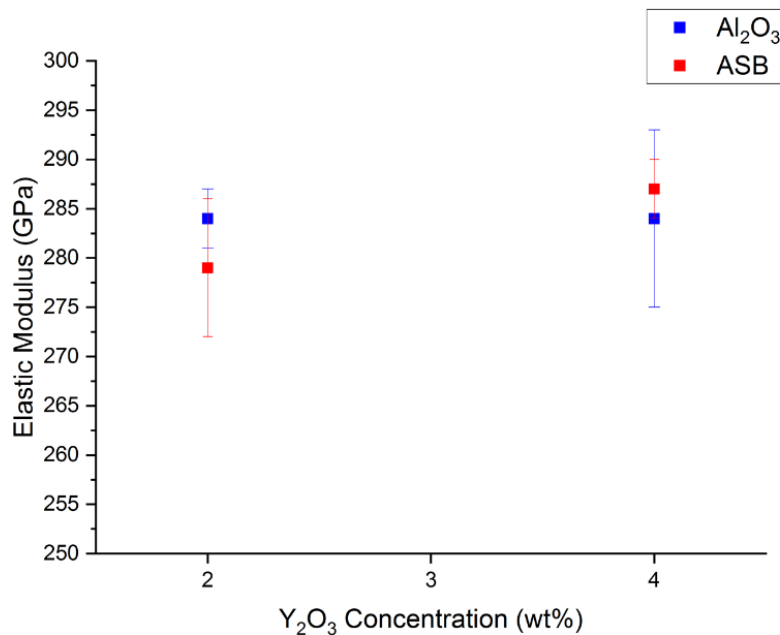


**Figure 28.** Elastic moduli of sintered SiAlONs, showing no statistically significant difference as a function of both  $\text{Y}_2\text{O}_3$  concentration and presence of  $\text{Al}_2\text{O}_3$  or ASB. Error bars represent the statistical uncertainty of the measurement technique, based on the resolution of the instruments used and the number of measurements performed.

#### D. Conclusions

In this work, conventional sintering additive  $\text{Al}_2\text{O}_3$  powder was replaced by an aluminum-containing liquid alkoxide, aluminum tri *sec*-butoxide (ASB), for the synthesis of SiAlON ceramics. It was hypothesized that the molecular-level distribution of Al and O over the  $\text{Si}_3\text{N}_4$  particle surfaces would favor the dissolution of Al and O in the lattice over the incorporation of Al and O via  $\text{Al}_2\text{O}_3$  powder, thereby enhancing densification. The ultimate goal is to minimize the volume of residual glassy grain boundary phase, mitigating high-temperature creep in SiAlONs and increasing the effective operating temperatures. A further benefit would be the reduction of reliance on rare earth oxides.

It was found that Al distribution remained homogeneous after heating to 1000 °C for alkoxide-bearing powder blends. SiAlONs synthesized using ASB exhibited comparable densities to those sintered using  $\text{Al}_2\text{O}_3$  at common dwell times and concentrations of  $\text{Y}_2\text{O}_3$ . However, when the system was starved of yttria, the ASB sample exhibited higher density than its  $\text{Al}_2\text{O}_3$ -containing counterpart. It also appears that some

SiAlONs fabricated with ASB have higher  $\beta$ -phase unit cell volumes than those generated via  $\text{Al}_2\text{O}_3$  powder. There was no evidence of crystalline  $\text{Al}_2\text{O}_3$  phases being generated during the sintering cycles of SiAlON powder blends containing ASB by SEM, EDS, DTA, or XRD of the powders. Elastic moduli of the two types of SiAlONs were comparable at each  $\text{Y}_2\text{O}_3$  concentration.

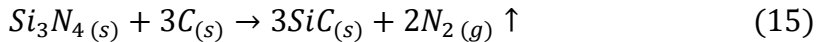
Ultimately, this work indicates that the use of molecular precursors as sintering aids may provide the opportunity to decrease the volume of liquid phase required for SiAlON densification, while still achieving high density. This may open the door to higher operating temperatures for SiAlONs and as such, increase the efficiency of advanced combustion engines.

### III. EXPLORATION OF AN ATOMIC-SCALE BORON ADDITIVE IN SIALON CERAMICS

#### A. Introduction

The goal of this work was to explore the effect of an atomic scale boron additive in silicon nitride and SiAlON ceramics, based on literature reports of enhanced thermal stability when boron is added to polymer-derived SiCN ceramics.<sup>93</sup> There are no known studies on the effects of boron in  $\text{Si}_3\text{N}_4$  or SiAlON ceramics.

The motivation for the addition of boron includes evidence from the literature concerning silicoboron carbonitride (SiBCN) in comparison to boron-free silicon carbonitride (SiCN). As such, a discussion of the causes for improved thermal stability in SiBCN are relevant here. The disordered turbostratic boron nitride (t-BN) structure develops in this ultrahigh temperature polymer-derived ceramic (PDC).<sup>101, 141</sup> This structure consists of layers of 6-fold B-N rings which exhibit rotational disorder in the c (stacking) direction.<sup>103</sup> The X-ray amorphous PDC SiBCN exhibits chemical inhomogeneity on the nanoscale in the form of domains of Si-N tetrahedra surrounded by layers of free carbon and t-BN. These BN layers are thought to confine the free carbon, reducing its reactivity with the Si-N domains and forestalling the decomposition reaction found in Equation 15.<sup>84, 105, 142</sup>



Effectively, both  $\text{Si}_3\text{N}_4$  and SiC are prevented from nucleating with the addition of boron to the PDC. Boron has been shown to increase the activation energy for  $\text{Si}_3\text{N}_4$  crystallization in SiBCN from 7.8 eV at 3.7 atomic % B to 11.5 eV at 8.3 atomic % B.<sup>98</sup>

This chapter focuses on processing and analysis of SiAlON with atomic scale boron additions. Background on  $\text{Si}_3\text{N}_4$  and SiAlON ceramics is given in Chapter I, pgs. 5-15. Further analysis of fracture origins and the effects of boron on dense SiAlON is given in Chapter IV. The effects of boron doping of SiAlONs on their microstructures, phase compositions, and resultant structural properties are reported here for the first time. This study aims to elucidate the effects of boron in a crystalline system of similar chemistry to SiBCN.

## B. Materials and Methods

In this work, a single industrially-relevant  $\beta'$ -SiAlON stoichiometry was targeted ( $\text{Si}_{6-z}\text{Al}_z\text{O}_z\text{N}_{8-z}$ ,  $Z = 0.5$ ) through the use of the liquid organometallic precursor aluminum tri *sec*-butoxide (ASB) investigated in the previous chapter.<sup>132</sup> This starting powder blend was then modified by varying concentrations of boric acid ( $\text{H}_3\text{BO}_3$ ), which was incorporated as a boron-containing molecular precursor. The composition of the powder blends can be found in Table III. Note that liquid phase sintering additive  $\text{Y}_2\text{O}_3$  (38 nm, Nanografi Nanotechnology, Turkey) and  $\text{H}_3\text{BO}_3$  dopant (technical grade, Rose Mill Co., USA) were added as a *percentage of the base blend*, which consists solely of  $\text{Si}_3\text{N}_4$  (UBE SNE-10, >95 wt%  $\alpha$  phase, UBE, Japan), AlN ( $D_{50} = 8 \mu\text{m}$ , Alfa Aesar, USA), and ASB (97%, Sigma Aldrich, USA). Boric acid purity was confirmed via TGA, in which  $\text{H}_3\text{BO}_3$  powder retained 56.62 % of its mass on heating to 400 °C. Based on the reaction in Equation 16, the theoretical mass of  $\text{H}_3\text{BO}_3$  retained on conversion to  $\text{B}_2\text{O}_3$  is 56.31 %.



**Table III. SiAlON Powder Blend Compositions for Boron Incorporation (wt%)**

<b>Sample</b>	<b>Base Composition</b>			<b>Additives</b>		<b>Eq. Boron Concentration (at%)</b>
	<b>Designation</b>	<b><math>\text{Si}_3\text{N}_4</math></b>	<b>AlN</b>	<b>ASB</b>	<b><math>\text{Y}_2\text{O}_3</math></b>	<b><math>\text{H}_3\text{BO}_3</math></b>
<b>B0</b>	81.03	3.49	15.48	4.1	0.00	0
<b>B1</b>	81.03	3.49	15.48	4.1	0.04	0.014
<b>B2</b>	81.03	3.49	15.48	4.1	1.00	0.35
<b>B3</b>	81.03	3.49	15.48	4.1	3.00	1.03

Powder blends were mixed in anhydrous isopropanol (99.5%, Sigma Aldrich, USA) and mixed by rotary ball milling at a rotational speed of 70 rpm in high-density polyethylene jars charged with approximately 1.5 kg of spherical  $\text{ZrO}_2$  milling media (YTZ, 10 mm diameter, Tosoh, Japan) for 24 hours. Milled suspensions were dried in a Buchi R-300 rotoevaporator equipped with a peristaltic vacuum pump and a water bath held at 80 °C. Densification was carried out in a uniaxial hot press equipped with a graphite interior and graphite resistive heating elements. Powders were encased in graphite dies lined with boron nitride which had a cross section of 1.5" x 2". A previously optimized

multi-step pressure and temperature profile was employed, as described in Figure 29. Final sintering temperature was 1760 °C, and final load applied was 14 US customary tons, resulting in a pressure of ~64 MPa. Sintering took place under vacuum until 1400 °C, then a static charge of ultrahigh purity nitrogen (UHP N<sub>2</sub>) was introduced into the chamber for the remainder of the profile.

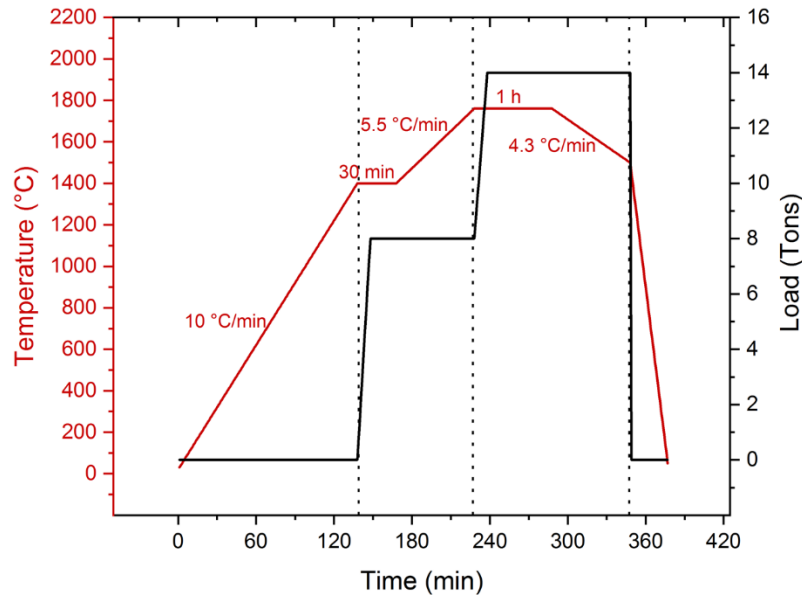


**Figure 29. SiAlON sintering profile.**

Four point ¼-pt flexure experiments were performed on ASTM B bars (500 grit surface finish, as-machined) using an Instron 5566 loading frame, fully articulating fixtures, and a loading rate of 0.5 mm/min.<sup>143</sup> Densities of the flexure specimens before fracture were measured via the immersion technique in deionized water at room temperature under the guidance of ASTM C-830.<sup>135</sup> Hardness was measured by Vickers indentation on surfaces polished to 1 µm using a LECO V-100-A2 Hardness Tester. Optical microscopy was performed on a Reichert-Jung Polyvar Met Light Microscope with a Plan Fluor 20x/0.40 objective. Optical images were captured by a SPOT Insight 4 color digital camera. Indentation crack resistance (ICR) was calculated using the lengths of the cracks emanating from the corners of the Vickers impressions.<sup>126-127</sup>

Many formulas have been proposed for the calculation of ICR, but this work utilized the relation put forth by Niihara and coworkers in 1982, which can be found in Equation 17.<sup>127</sup>

$$K_C = 0.0421 \frac{E^{0.4} P^{0.6} a^{0.8}}{C^{1.5}} \quad (17)$$

$K_C$  is the critical stress intensity factor, E is the elastic modulus, P is the load applied during indentation, a is the half diagonal length of the Vickers impression, and C is the corner crack length *plus* the half diagonal length (a). In this work, C is measured from the intersection of the impression diagonals (center of the impression) to the tip of the corner crack, as a single value. a is ½ the average of the measured diagonal lengths.

X-ray diffraction (XRD) was performed on a Bruker D2 Phaser benchtop diffractometer (Bruker, USA) with Cuk $\alpha$  radiation (1.5406 Å). Phase identification was carried out in the program Diffrac.Eva. Raman spectroscopy was performed on a WITec Alpha 300RA spectrometer (WITec GmbH, Germany) using a variable power 488 nm laser and Nikon 50X/0.55 objective. Laser power was set to 30 mW, and a 600 grooves/mm grating with accompanying spectral center of 700 cm<sup>-1</sup> was utilized. The <sup>11</sup>B nucleus was further probed by solid-state magic angle spinning nuclear magnetic resonance (<sup>11</sup>B SS MAS-NMR) using a Bruker Advance 300 MHz spectrometer (Bruker, USA) with a field strength of 7.05 T with a magic angle spinning frequency of 12 KHz. Single-pulse excitation experiments were carried out with a pulse angle of approximately 30°.

Scanning electron microscopy (SEM) was performed on an FEI Quanta 200 Environmental Scanning Electron Microscope (Thermo Fisher Scientific, USA). Grain size of sintered SiAlONs was measured by the average grain intercept technique, wherein ten random lines were drawn on each of five micrographs within the same sample and grain size is calculated by dividing the length of the line by the number of grain boundaries it intersects.<sup>144</sup> Imaged surfaces were first etched for 5 minutes at 400 °C in a molten salt solution of KOH and KNO<sub>3</sub> in a weight ratio of 1:9.<sup>145</sup> Scanning transmission electron microscope (STEM) and EDX elemental analysis were performed using an FEI Talos F200X (Thermo Fisher Scientific) equipped with 4 in-column SDD Super-X detectors. The TEM was operated at 200 kV. TEM specimens were prepared using a FEI Scios 2 DualBeam (Thermo Fisher Scientific) ultra-high-resolution analytical FIB-SEM system.

### C. Results and Discussion

The apparent densities of B0, B1, B2, and B3 can be found in Figure 30.  $H_3BO_3$  dopant levels ranging from 0 to 1 wt% do not seem to affect the density of resultant SiAlONs, while 3 wt% boric acid addition results in a sharp decrease in density. However, for all SiAlONs, the average saturated weights from the immersion density experiment did not exceed 0.03% of the dry weights. In particular, the average saturated weight of B3 was only 0.018% greater than the average dry weight. This is an indication of very low porosity, since whatever open pores which absorb water and contribute to the greater saturated weight than dry weight were once closed pores before machining into the flexure specimens. As such, it is believed that B3 simply has a lower theoretical density than the others, owing to the greater concentration of  $H_3BO_3$  additive.

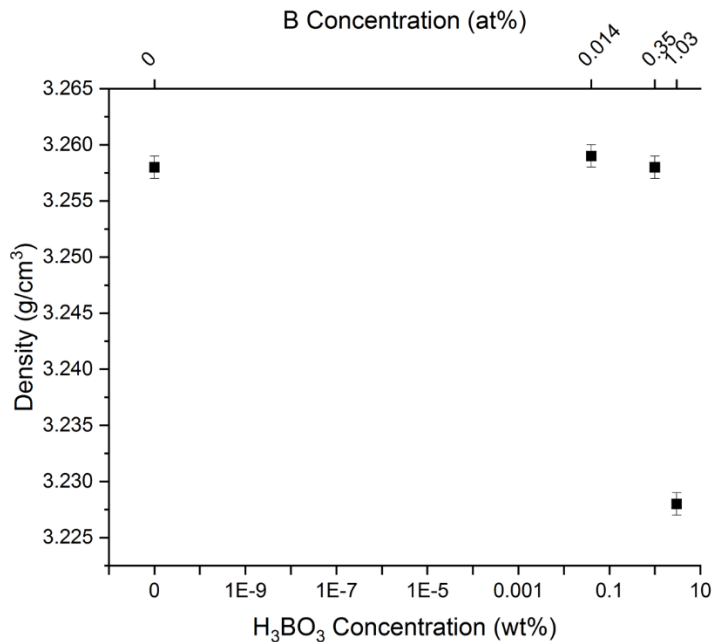


**Figure 30. Immersion densities of SiAlONs with increasing boron concentration.**

Lower-boron SiAlONs B0, B1, B2, and B3. B0-B2 exhibited comparable and high densities, while the 3 wt%  $H_3BO_3$ -containing SiAlON blend achieved a lower density. Error bars represent the statistical uncertainty of the measurement technique, based on the resolution of the instruments used and the number of measurements performed.

The XRD analysis of B0-B3 can be found in Figure 31. Second phases such as yttrium silicates and residual  $\alpha$ - $\text{Si}_3\text{N}_4$  are found in low-B samples, and are not uncommon in SiAlONs. However, at 3 wt%  $\text{H}_3\text{BO}_3$  addition (or equivalently ~1.03 at% boron), B3 is a pure, single-phase  $\beta'$ -SiAlON. The XRD peak intensities for all second phases decrease gradually with increasing boron content. This phenomenon is evidence that the addition of boron reduces the crystallization of second phases in the grain boundary and may enhance the  $\alpha \rightarrow \beta$  conversion.

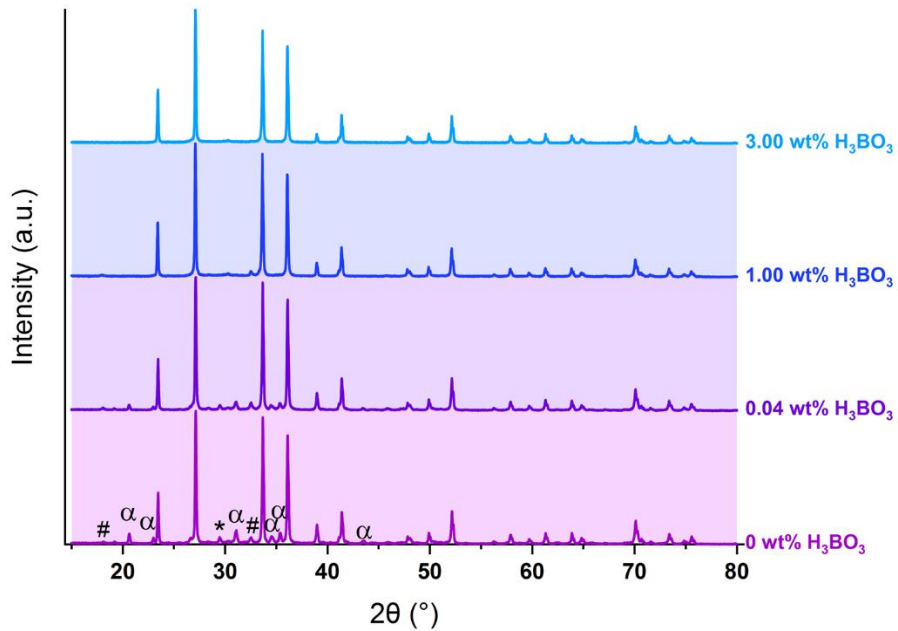


**Figure 31. XRD patterns of boron-containing SiAlONs B0-3.** Residual  $\alpha$ - $\text{Si}_3\text{N}_4$  and other miscellaneous second phase peaks are found in the boron-free SiAlON and show a reduction in intensity until a single-phase  $\beta'$ -SiAlON was achieved in B3.  $\alpha$  denotes  $\alpha$ - $\text{Si}_3\text{N}_4$  (PDF card 04-001-1514), \* denotes  $\text{Y}_{10}\text{Si}_3\text{Al}_2\text{O}_{18}\text{N}_4$  (PDF card 00-032-1426), # denotes  $\text{Y}_2\text{AlSiNO}_5$  (PDF card 04-012-5019), and unlabeled peaks are  $\beta'$ -SiAlON (PDF card 04-007-0791).

Raman spectroscopy revealed that boron exists in a turbostratic structure. The Raman peak at approximately  $1370 \text{ cm}^{-1}$  is assigned to the in-plane  $E_{2g}$  symmetric vibrational mode of t-BN, which is schematically explained in Figure 32.<sup>104, 146-147</sup> Raman spectra can be found in Figure 33. The band indicating t-BN ( $1370 \text{ cm}^{-1}$ ) appears to increase in relative intensity with increasing boron content, which implies the increasing prevalence

of t-BN.<sup>103-104</sup> The band is also present in the 1 wt% H<sub>3</sub>BO<sub>3</sub>-SiAlON, though it is small and was only observable by plotting that spectrum independently and zooming in (see inset). The absence of a peak at 806 cm<sup>-1</sup> indicates that B<sub>2</sub>O<sub>3</sub> is not favored.<sup>148</sup> This is important, as B<sub>2</sub>O<sub>3</sub> would likely promote an undesirably low-melting temperature grain boundary glass.

Note the presence of residual  $\alpha$ -Si<sub>3</sub>N<sub>4</sub> peaks in the Raman spectra of low-B samples (Figure 33), which is consistent with XRD analysis (Figure 31).<sup>149-150</sup> These results confirm that the t-BN bonding condition is produced in SiAlONs to which H<sub>3</sub>BO<sub>3</sub> has been added.

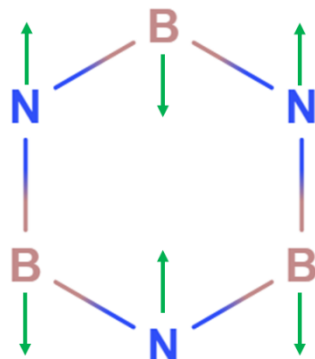


**Figure 32.** Schematic of the in-plane E<sub>2g</sub> symmetric vibrational mode of t-BN and h-BN, which gives rise to a Raman peak at  $\sim$ 1370 cm<sup>-1</sup>.

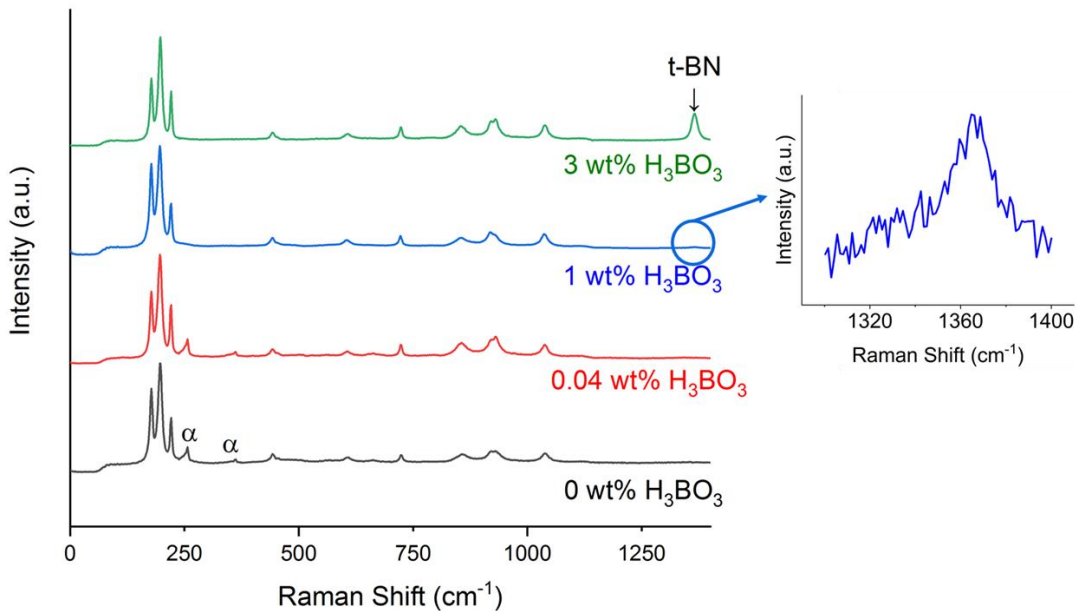


**Figure 33.** Raman spectra of boron-containing SiAlONs B0-B3. The peak at approximately  $1370\text{ cm}^{-1}$  provides evidence of t-BN. Note the peaks related to residual  $\alpha\text{-Si}_3\text{N}_4$  in SiAlONs with lower concentration of boron, which disappear with higher dopant concentrations and are consistent with XRD analysis. The inset displays the 1 wt%  $\text{H}_3\text{BO}_3$  SiAlON spectrum in the range of  $1300 - 1400\text{ cm}^{-1}$ . It is evident that a small t-BN peak begins to appear at this dopant level.

The successful addition of boron to produce t-BN in an industrially relevant low-Z SiAlON composition has important implications. Composite research on the addition of BN particle reinforcement in  $\text{Si}_3\text{N}_4$  has indicated improvements in toughness, however blending of powders often leads to flaws, resulting in decreased strength.<sup>115</sup> This work demonstrates for the first time that boron nitride compounds can be generated from the molecular scale in situ during densification of SiAlON ceramics. This suggests that there may be a path towards in situ nucleation and growth of BN for toughening and prevention of high temperature creep.

Further confirmation of the bonding conditions of the boron in the SiAlON structure was achieved with NMR. This was to assure that any non-Raman active boron coordination could be ruled out.  $^{11}\text{B}$  SS MAS-NMR was performed on the most boron-rich SiAlON, B3, to compliment Raman results. The resultant NMR spectrum is presented in

Figure 34, which shows broad peaks centered between approximately 20 and -3 ppm. This spectrum is representative of the hexagonal boron nitride (h-BN) structure, which exhibits boron in threefold coordination with nitrogen in a layered configuration structurally and chemically similar to t-BN.<sup>151-152</sup> In fact, <sup>11</sup>B SS NMR studies of SiBCN polymer-derived ceramics have yielded remarkably similar spectra.<sup>153-154</sup> In this work, the measured NMR spectrum of B3 exhibits a slight perturbation between the prominent isotropic shift peaks. This may be tentative evidence of some four-coordinated boron (B[IV])<sup>155</sup>, but if it is present, it is far less prevalent than B[III].

The <sup>11</sup>B nucleus has spin-3/2 and is therefore known as a quadrupolar nucleus, exhibiting lower symmetry than a spin-1/2 nucleus such as <sup>1</sup>H (proton). Consequently, the peaks resulting from an NMR experiment are characteristically broad and exhibit prominent tails. However, both the breadths and the positions of the peaks in the present B3 sample are consistent with previously documented spectra of boron in trigonal planar coordination.<sup>151-152</sup> It appears that no boron bonding condition other than t-BN is generated in these boron-modified SiAlONs.

The two peaks in the spectrum presented in this work (Figure 34) are actually a doublet arising from heteronuclear spin-spin coupling of the boron nucleus with the spin-1/2 <sup>15</sup>N nucleus. This N nucleus has two degenerate energy states which align either antiparallel or parallel to the applied magnetic field during the NMR experiment, respectively shielding or deshielding the <sup>11</sup>B nucleus. Shielded <sup>11</sup>B nuclei give rise to upfield-shifted signal (lower chemical shift) and deshielded <sup>11</sup>B nuclei give rise to downfield-shifted signal (higher chemical shift). Therefore, in the absence of this spin-spin coupling, one might expect the <sup>11</sup>B signal to appear around 5 ppm. Additionally, the presence of a simple doublet rather than complex “doublets of doublets” (dd) indicates that there is only one nucleus which is splitting the <sup>11</sup>B nucleus. Complex coupling would imply the presence of multiple boron coordinations.<sup>156</sup> Note that spinning sidebands around 150 and -150 ppm are experimental artefacts arise from the modulation of the magnetic field at the frequency of spinning in the MAS-NMR experiment.<sup>157</sup> This NMR analysis is consistent with previous Raman results concluding that boron exists in 3-fold coordination as t-BN.

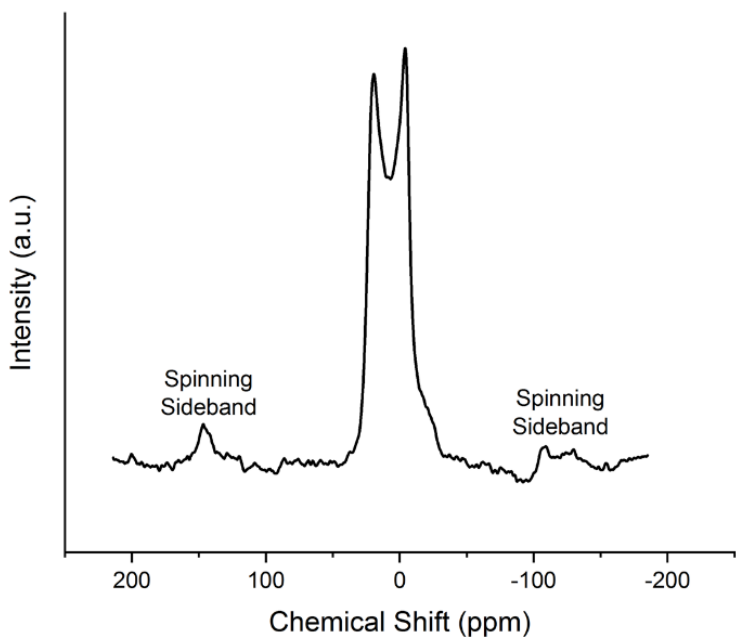


**Figure 34.**  $^{11}\text{B}$  SS MAS-NMR spectrum of boron-rich SiAlON B3, indicating boron in threefold coordination with nitrogen (B[III]).

A notable result of the present work was the superior strength of B3, containing 3 wt%  $\text{H}_3\text{BO}_3$ , which exhibits an average flexural strength of 1016 MPa, 23% higher than boron-free B0. Details of strength testing and full fractographic analysis of these specimens is reported in Chapter IV, and B0, B1, and B2 exhibited many inclusions as fracture origins, while B3 only exhibited subtle surface flaws such as machining cracks as fracture origins.<sup>42</sup> Also noteworthy is that B0, B1, and B2 all exhibited comparable flexure strengths, and it was only at 3 wt%  $\text{H}_3\text{BO}_3$  concentration that an increase in strength was observed. Recall that it was only at this relatively high boron content that a phase-pure  $\beta'$ -SiAlON was achieved. These XRD, strength, and fractographic data in concert are consistent with weakest link theory in that the presence of even a single severe flaw in the localized region of high tensile stress would cause failure, even if the population of this flaw was reduced. It is not until the most severe flaw population is eliminated entirely that the fracture becomes dictated by a less severe flaw population.

Examples of grain size measurements are presented in Figure 35, and the average grain sizes for all SiAlONs are illustrated in Figure 36. Figure 37 details the grain size distributions of each SiAlON. Each grain size measurement consisted of 10 random lines drawn on each of 5 random micrographs. Each line intercepted approximately 5-15 grains. It was found that the SiAlON containing high boron content (3 wt%  $H_3BO_3$ ) exhibited similar average grain sizes to the boron-free SiAlON, but the standard deviation of grain size was greatly reduced with the incorporation of boron, indicating that the grain size distribution is narrower in these doped SiAlONs. The refinement of matrix grain size by the incorporation of hexagonal boron nitride nanoplatelets (h-BNNPS) has been reported in previous work, but it was attributed to grain boundary pinning by the BN nanoparticles and consequent porosity.<sup>114</sup> This work provides no evidence of the existence of crystalline BN nanoparticles, so it appears that the grain size refinement is a chemical effect. Since abnormally large grains may act as inclusions and therefore, fracture origins, the narrowing of the grain size distribution may benefit the overall strength and reliability of SiAlONs. This is particularly impactful in the SiAlON system because the growth of  $\beta'$ -SiAlON grains is often considered an exaggerated grain growth phenomenon.

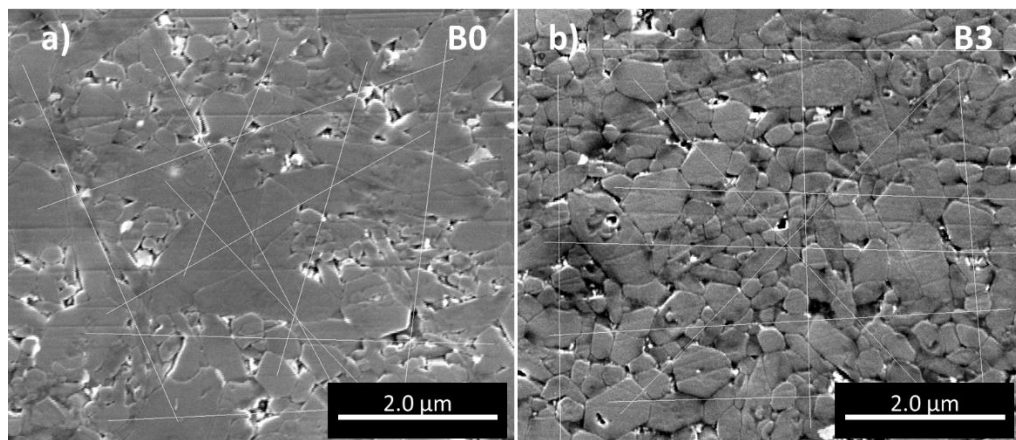


**Figure 35.** Micrographs of etched surfaces of a) a zero-boron SiAlON B0 and b) the most boron-rich SiAlON B3, with random lines drawn for grain size analysis. The imaging plane is perpendicular to the hot pressing direction.

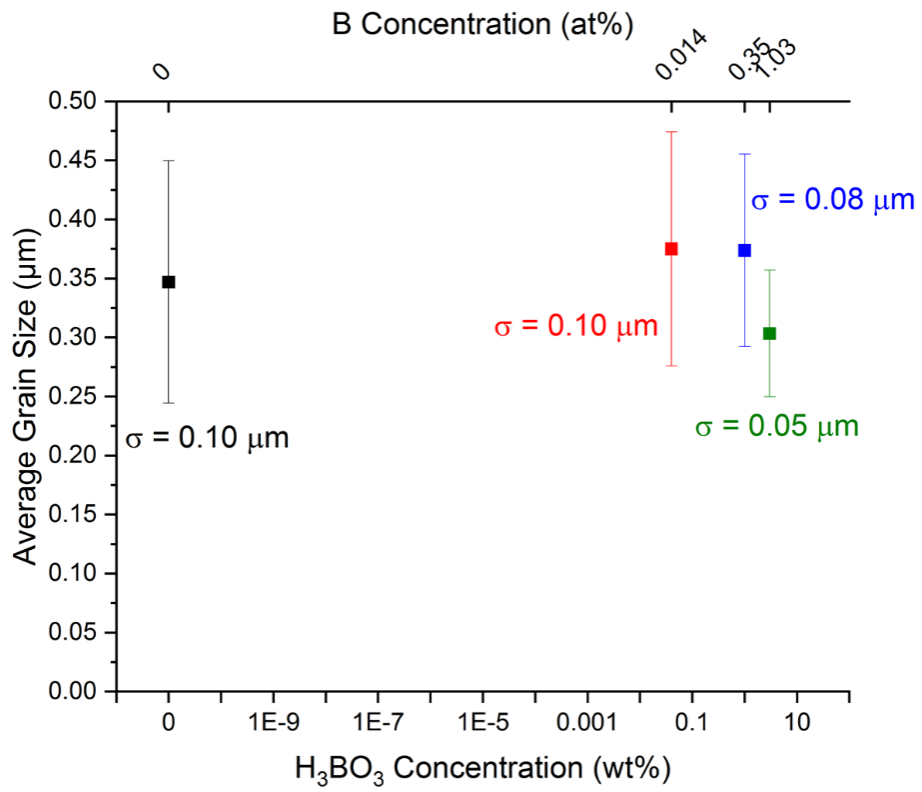


**Figure 36.** Average grain sizes of boron-containing SiAlONs B0-B3, indicating comparable grain sizes but reduced standard deviation of grain size. Error bars represent 1 standard deviation.

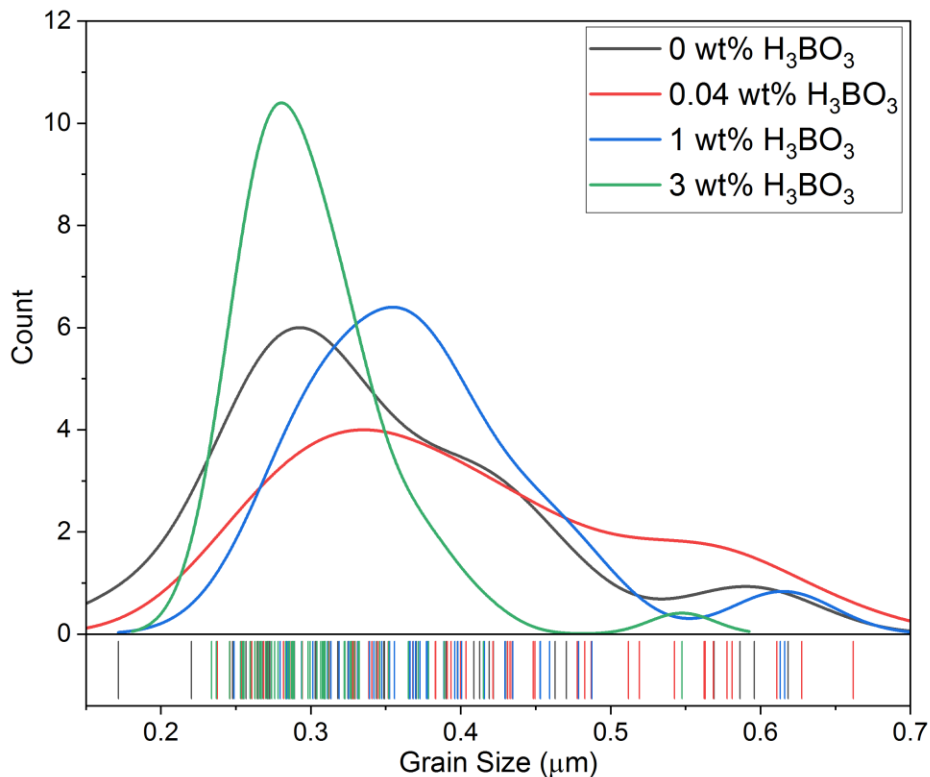


**Figure 37.** Grain size distributions of the four SiAlONs of varying boron concentration, indicating that the distributions become narrower with increasing boron concentration. Each line in the “rug” section on the bottom of the plot indicates a single measurement.

STEM coupled with EDS mapping was performed to further understand the chemistry of the grain boundary glassy phase. The STEM EDS mapping results presented in Figure 38 highlight the grain boundary phase of B3, the most boron-rich SiAlON in the present work. From these chemical maps, it can be discerned that the SiAlON matrix grain regions (labelled “Grain”) are primarily rich in Si and N, with lower concentrations of Al and O, in accordance with the  $\beta'$ -SiAlON formula ( $\text{Si}_{6-z}\text{Al}_z\text{O}_z\text{N}_{8-z}$ ,  $Z = 0.5$ ). The region between them is the intergranular glass (labelled “IGG”) and is richer in Al and O than the grain interior. It appears that all of the yttrium is confined to the grain boundary glass. In fact, it appears that the grain boundary phase consists of Si, Al, O, N, Y, and B. The EDS signal from boron is always very low, so it is difficult to confidently determine whether or not it enters the lattice. However, when taken in tandem with the Raman and NMR

spectroscopic data, it can be reasonably posited that boron does not favor the tetrahedral coordination of silicon in the  $\text{Si}_3\text{N}_4$  structure, and is most likely bonded in the turbostratic BN (t-BN) structure in the grain boundary glass. This is further supported by Rietveld refinements of the  $\beta'$ -SiAlON structures, which reveal that the unit cell volume of the  $\beta'$ -SiAlON is not significantly affected by any boron concentration. These unit cell volume results can be found in Figure 39.

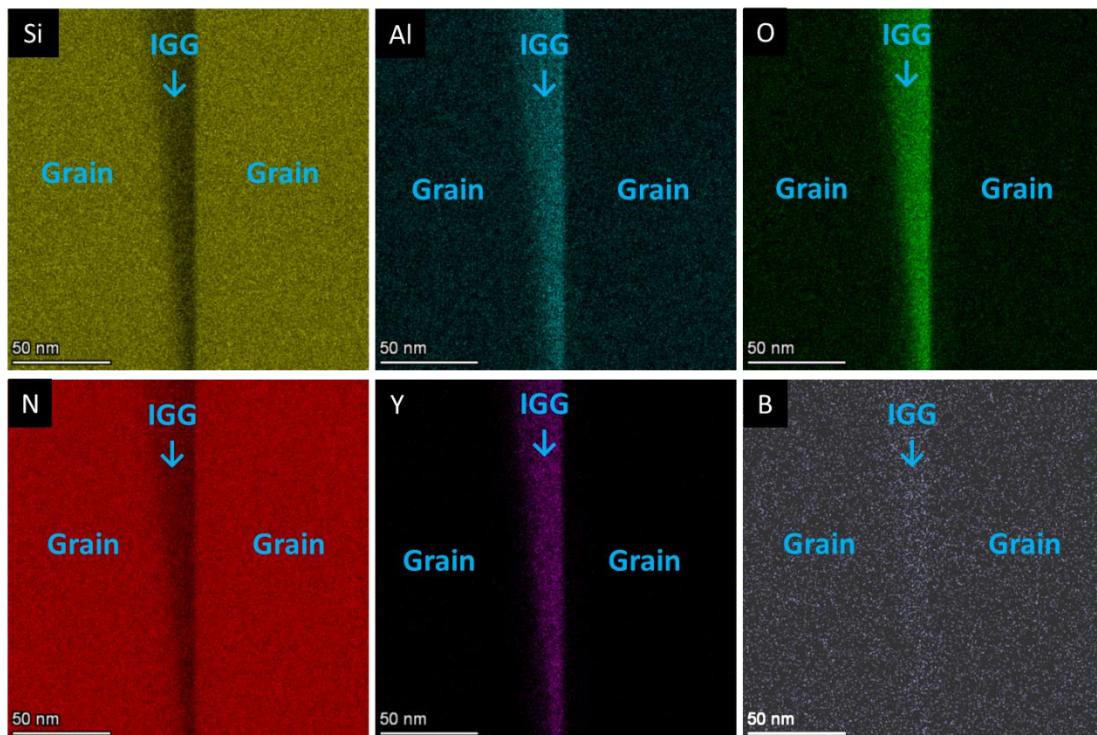


**Figure 38.** EDS elemental maps from TEM analysis of the grain boundary region of the high-boron SiAlON B3, showing a grain interior rich in Si and N, with minor concentration of Al and O, and an intergranular glass rich in Y and O, with minor concentration of Si and N. Y does not seem to have entered the  $\text{Si}_3\text{N}_4$  lattice. Boron may have a preference for the grain boundary, but low EDS signal makes this difficult to conclude.

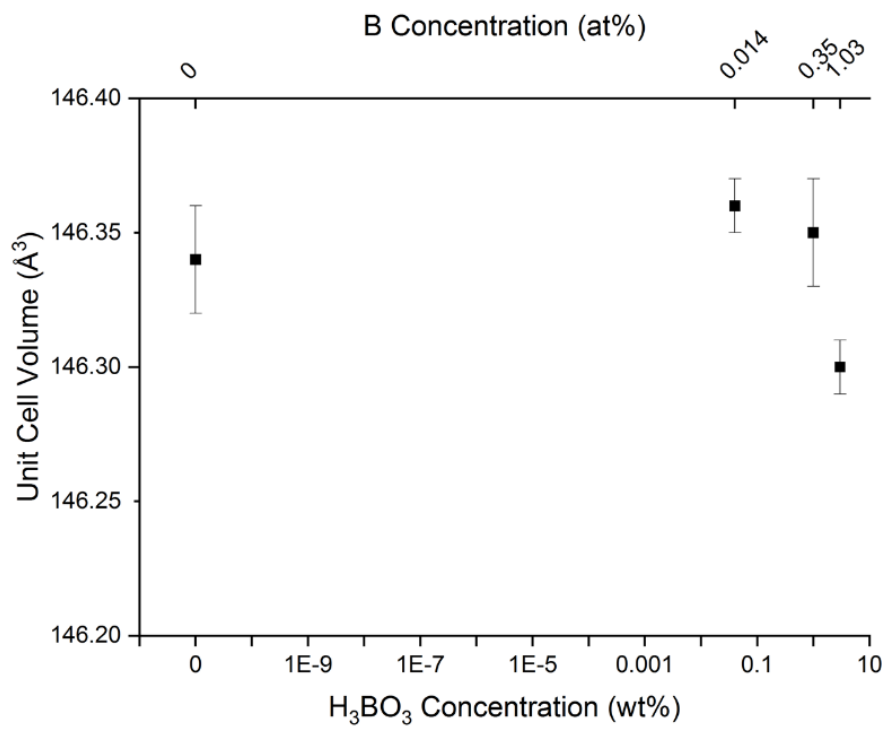


**Figure 39.** Unit cell volumes of  $\beta'$ -SiAlON as a function of boron concentration, revealing little to no effect.

Electron diffraction revealed that the grain boundary phase of the boron-rich SiAlON B3 is indeed amorphous. Figure 40 illustrates a STEM-high angle annular dark field (HAADF) micrograph with accompanying convergent beam electron diffraction (CBED) patterns, which allow for the interrogation of small volumes. It is clear that the dark regions, which represent the SiAlON matrix grain, are crystalline, while the grain boundary phase, shown as the white regions of the micrograph, is amorphous. This is evidence that crystallization in this phase, either of various Y-SiAlON phases or of hexagonal boron nitride nanoparticles, does not occur. Further, Figure 41 shows a higher magnification STEM-low angle annular dark field (LAADF) image of the same grain boundary region, where the atomic rows of the matrix phase can be seen in the rightmost grain (lighter region). It appears that the interface between the crystalline phase (rightmost region) and glass phase near the grain boundary (leftmost region) is quite definitive, and that the specimen does not undergo an amorphous-to-crystalline transition from the grain boundary glass to the matrix crystal phase.

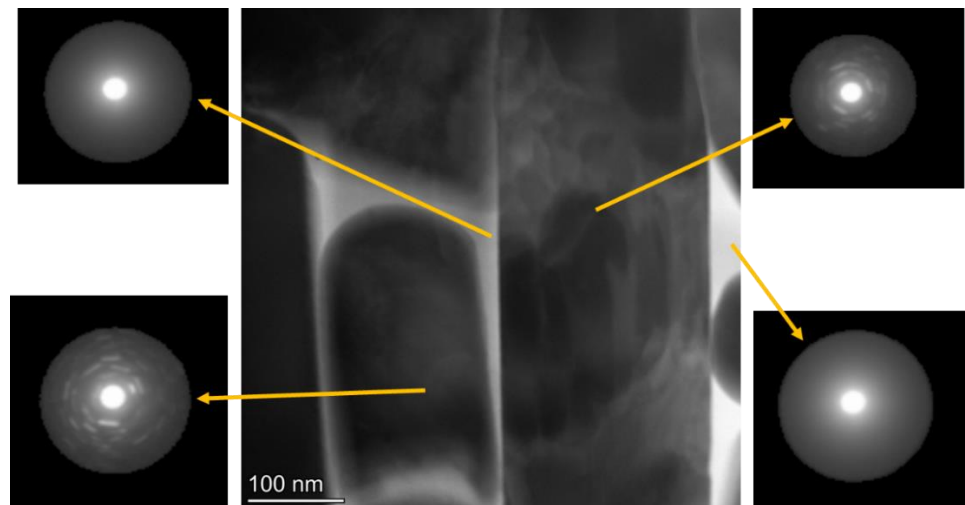


**Figure 40.** Transmission electron micrograph of the grain boundary region of boron-rich SiAlON B3. Accompanying convergent beam electron diffraction (CBED) patterns indicate that grain interiors (dark regions) are crystalline while the intergranular phase (lighter region) is amorphous.

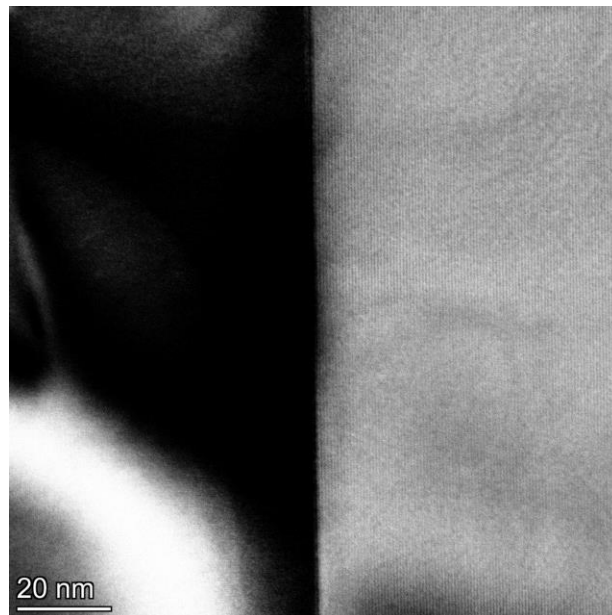


**Figure 41.** High-magnification STEM image of the grain boundary region of boron-rich SiAlON B3, wherein the lighter region is the matrix crystal phase and the darker region is the glass phase near the grain boundary. The micrograph indicates that the crystal phase is well-ordered throughout, and an amorphous-to-crystalline transitional region is not present between the matrix crystals and the grain boundary.

The hardness of the SiAlONs in this study decreases somewhat linearly with increasing boron concentration from 16.3 to 14.5 GPa. This is consistent with XRD and Raman analyses since it is well known that the equiaxed  $\alpha$  phase of silicon nitride exhibits higher hardness than the  $\beta$  phase, so decreasing  $\alpha$  content would logically lead to lower hardness. Investigation of indentation crack resistance did not yield any strong trends, although the boron-free B0 seemed to exhibit slightly higher resistance to crack propagation. These results are summarized in Figure 42. Overall, the hardness and crack resistance results are consistent with the grain size distributions observed in these SiAlONs. The large, needle-like grains that contribute toughness and the small, equiaxed grains that contribute hardness are both moderated by the addition of boron.

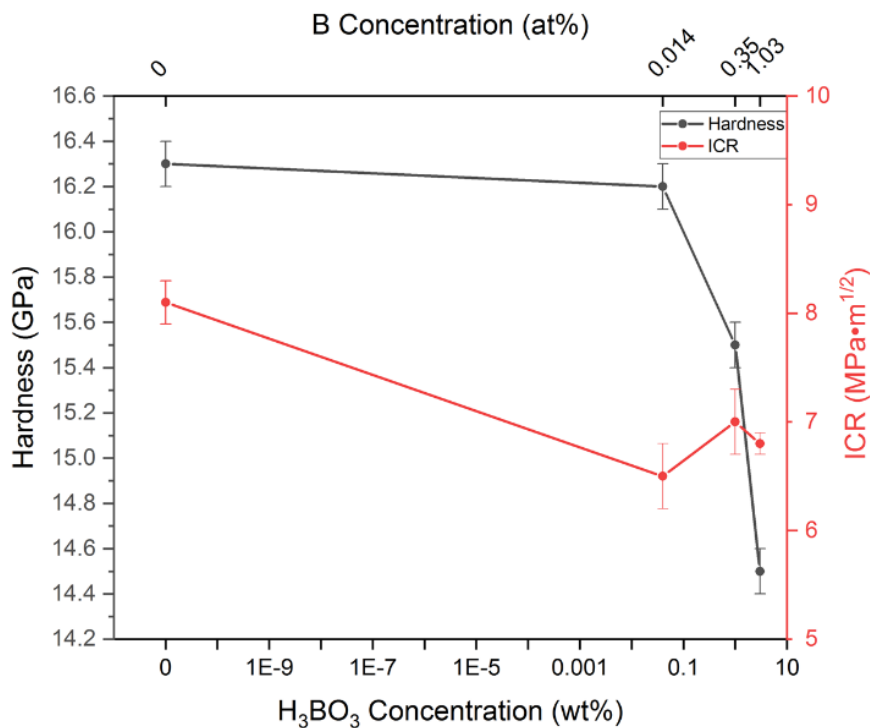


**Figure 42.** Hardness and indentation crack resistance of SiAlONs as a function of boron concentration. Hardness decreases linearly with increasing boron content. ICR does not show any strong trend, but B0 appears to exhibit a slightly higher value. Hardness error bars indicate the statistical uncertainty of the measurement technique. ICR error bars indicate standard deviation of the measurements.

These results are interpreted from the standpoint of atomic diffusion. It is hypothesized that the presence of t-BN in the SiAlON grain boundary glass inhibits the diffusion which would i) facilitate the crystallization of second phases, and ii) allow for exaggerated grain growth via dissolution-reprecipitation. Turbostratic BN is believed to act as a diffusion barrier to carbon in the SiBCN polymer-derived ceramic system, and has been shown to increase the activation energy for  $\text{Si}_3\text{N}_4$  crystallization in this system as well.<sup>98</sup> In this work, SiAlONs with a more uniform, homogeneous, and phase-pure microstructure were synthesized by the incorporation of boron at the atomic level via precursor boric acid ( $\text{H}_3\text{BO}_3$ ).

These results ultimately point toward a method for controlling mass transport through the grain boundary phase of SiAlONs and thus, controlling their microstructures and consequent structural properties.

#### D. Conclusions

This work demonstrates the effects on microstructure and structural properties of SiAlONs doped with varying concentrations of boron via precursor boric acid ( $\text{H}_3\text{BO}_3$ ). It was previously reported that no effect on flexure strength was observed for  $\text{H}_3\text{BO}_3$  concentrations of 0, 0.04, and 1 wt% on top of the base blend. However, 3 wt%  $\text{H}_3\text{BO}_3$  yielded SiAlONs with average strength of 1016 MPa, 23% higher than the undoped SiAlON B0. The reverse trend was observed in density measurements, in which B0, B1, and B2 all exhibited comparable and high densities, whereas B3 showed a sharp decrease in density. XRD analysis revealed that the SiAlON with the highest boron dopant concentration was a phase-pure  $\beta'$ -SiAlON, whereas lower dopant concentrations all resulted in  $\alpha\text{-Si}_3\text{N}_4$  and/or other second phase peaks. Correspondingly, the turbostratic boron nitride structure was detected by Raman spectroscopy and  $^{11}\text{B}$  SS MAS-NMR, indicating that the boron exists in threefold coordination with nitrogen in a layered ring motif. This t-BN structure is present in SiBCN polymer-derived ceramics and forestalls their thermal decomposition by confining carbon to its layered graphitic structure. The BN can be thought of as a diffusion barrier in this material. Its presence in boron-doped SiAlONs, coupled with the reduction in second phase crystallization, higher strength, lack of inclusions as fracture origins, and narrowing of grain size distribution all indicate that

the presence of t-BN in SiAlONs may reduce the diffusion through the grain boundary glass. This technique offers a possible chemical route to the control of SiAlON microstructures, suppression of flaw populations, and improvement of their ultimate structural properties.

## **IV. FRACTOGRAPHY OF SILICON NITRIDE BASED CERAMICS TO GUIDE PROCESS IMPROVEMENTS**

The work detailed in this chapter is based on concepts and results published by McGarrity, *et al.* (2020).<sup>42</sup> Some text is taken verbatim from the publication.

### **A. Introduction**

As structural ceramics of interest for high-risk applications,  $\text{Si}_3\text{N}_4$ , SiAlONs, and their composites have been the subject of many fracture studies. Through controlled microstructural development, fracture stresses of  $\sim 1100$  MPa and fracture toughness ( $K_{IC}$ ) values of between 6 and 12  $\text{MPa}\cdot\text{m}^{1/2}$  can be achieved for these materials.<sup>25</sup> The present work describes an in-depth fractographic analysis of the boron-containing SiAlONs discussed in Chapter III, as well as traditional  $\text{Al}_2\text{O}_3$ -containing samples modified with boron, with the aims of building the growing fracture mechanics database for SiAlONs and providing guidance for future processing of these materials.

The field of fractography encompasses a spectrum of utility, from a practical technique for the failure analysis of components in use to a fundamental fracture mechanics discipline with the goal of understanding the mechanisms of strain energy absorption and liberation during fracture.<sup>7</sup> The measurement of characteristic fracture markings can help the fractographer apply theoretical models proposed over the years to experimental fracture specimens in order to determine various properties of the specimen *post-mortem*. Further, various parameters for materials can be calculated and tabulated from laboratory experiments and applied to the fracture of components in use, where the loading conditions are less well-defined.

#### **1. Mathematical treatment of fracture**

In flexure, both compressive and tensile stresses develop in the specimen. In a typical flexure experiment, where the specimen is supported at its ends from below and load is being applied toward the center from above, the top surface will be subjected to maximum compression, and the bottom surface will experience maximum tension. These stresses vary linearly throughout the specimen from compression to tension, and as such,

stress in the central plane of the specimen is zero. This plane is known as the neutral axis, as represented by the beam cross section in Figure 43.

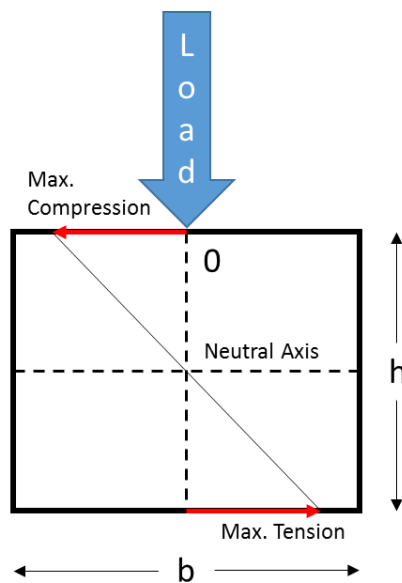


**Figure 43.** Schematic representation of the stresses developed throughout the cross section of a bar in flexure. Maximum compressive stress is located on top, maximum tensile stress on the bottom, and zero stress develops in the center, or neutral axis.

The stresses developed in the specimen can be described by Equation 18, where  $\sigma$  is the stress in the flexure sample at a given load (MPa),  $F$  is the load (N),  $L$  is the support span length (mm),  $y$  is the distance from the neutral axis,  $b$  is the width of the sample (mm), and  $h$  is the height of the sample (mm). Equation 19 is found by substituting the maximum possible distance from the neutral axis,  $\frac{1}{2} h$ , for  $y$ . Equation 20 describes the maximum strain developed in the outermost surface of the specimen in bending, where  $\epsilon$  is the axial strain induced in the sample at a given crosshead displacement, and  $w$  is the measured crosshead displacement. The derivations for these expressions can be found in Appendix B.

$$\sigma = \frac{3FLy}{2bh^3} \quad (18)$$

$$\sigma_{max} = \frac{3FL}{4bh^2} \quad (19)$$

$$\epsilon_{max} = \frac{432wh}{77L^2} \quad (20)$$

Note that Equation 19 may be used to calculate fracture stress if and only if the critical flaw is at the surface of the specimen. If it is in the interior of the specimen, it will be subjected to lower stresses than the outermost surface, or “extreme fiber”, of the specimen, so Equation 18 must be applied. It is therefore important to measure the location of internal origins so that an accurate value for the stress experienced *at the critical flaw* may be calculated.

The critical stress intensity factor,  $K_{IC}$ , is a measure of the stress state around a stress concentrator required to induce crack extension. It is a rather elusive parameter for which many experimental techniques and mathematical treatments have been developed and critically reviewed. Quinn<sup>7</sup> presents a simple relation using fractographic measurements for the calculation of  $K_{IC}$ , detailed in Equation 21

$$K_{IC} = Y\sigma_f\sqrt{c} \quad (21)$$

where  $Y$  is a geometric factor accounting for the shape of the critical flaw, ( $1 < Y < 2$ ),  $\sigma_f$  is the fracture stress at the origin, and  $c$  is the size of the flaw parallel to the neutral axis. This relation was first used by Leighton Orr of the Pittsburgh Plate Glass (PPG) Company as early as 1945.<sup>7</sup> Another parameter accessible through fractographic analysis is the fracture mirror constant. This parameter,  $A$ , is defined in Equation 22:

$$A = \sigma_f\sqrt{r} \quad (22)$$

where  $r$  is the fracture mirror radius. This constant is usually given as a range since it is quite difficult, particularly in polycrystalline ceramics, to measure the radius of the fracture mirror with sufficient precision to confidently yield a single value for  $A$ . Regardless, Equation 22 illustrates that if  $A$  is constant, then  $\sigma_f$  is proportional to  $r^{-1/2}$ . That is to say that the stronger the material is, the smaller the mirror can be expected to be. Equation 22 is useful because in a laboratory experiment, the stress is known, the mirror radius can be measured, and  $A$  can be calculated. However, the fracture stresses for components in use may not be readily known. Fractographic investigation may be undertaken to determine the

mirror radius for a fractured component, and if a database of mirror constants ( $A$ ) exists for the material, the stress at failure may be estimated. This is one example of the utility of a tabulated collection of calculated material parameters from laboratory experiments.

It is common for four point flexure experiments to yield lower fracture stress values than three-point experiments. This phenomenon has to do with the volume of specimen being subjected to the maximum stress at a given load. In three-point geometry, the maximum stress developed in a specimen is concentrated at a point directly below the loading point. However, in four point geometry, maximum stress is generated throughout the entire region between the two loading points. The results of an example finite element analysis found in Figure 44 illustrate this difference. The consequence of different volumes of the specimen being subjected to the maximum stress is rooted in weakest link theory. A greater volume of specimen under maximum stress yields a greater probability of activating the most severe flaw. Therefore, a four point flexure experiment is likelier to subject this critical flaw to the maximum stress developed in the specimen than a three-point experiment. Similarly, a uniaxial tensile experiment typically yields the lowest values for tensile strength as the entire specimen volume is being interrogated by a uniform maximum stresses field.

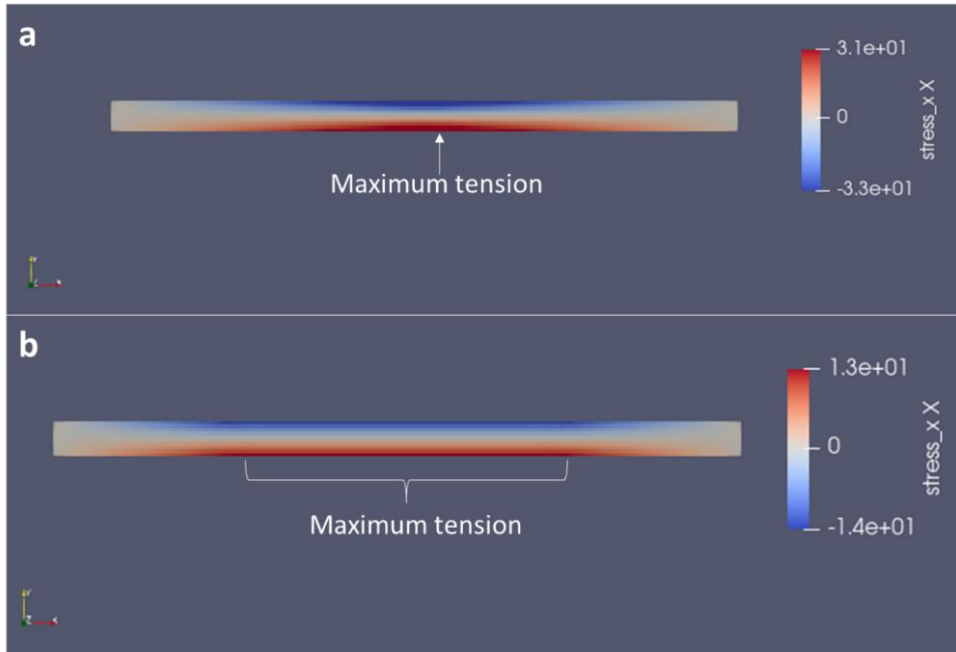


**Figure 44.** Finite element analysis of a bar in a) three-point bending geometry and b) four point bending geometry. In three-point bending, maximum stress is concentrated at a single point directly below the loading point. In four point bending, a uniform maximum stress region is evolved between the loading points. FEA performed in MOOSE software (Idaho National Laboratory, USA), results visualized in ParaView (Kitware, USA).

## 2. Fracture markings

Fracture initiates at the critical flaw. This is known as the fracture origin, and it might take the form of an inclusion, a pore, a surface crack, a microstructural inhomogeneity such as an abnormally large grain, or a host of other stress concentrators in a brittle specimen. Theoretically, fracture begins in a direction perpendicular to the neutral axis. When the crack enters the compressive region of the flexure specimen, it very often deflects to one side or another, leaving one fragment with a large piece missing from its compressive surface and the other with a large overhanging protrusion. This is called a “compression curl” or “cantilever curl”, and it is the result of the crack following the path of least resistance to its propagation. This ubiquitous feature informs the fractographer as to the orientation of the specimen during the experiment, as it indicates which surface was the compressive surface. Some common fracture paths are found in Figure 45.

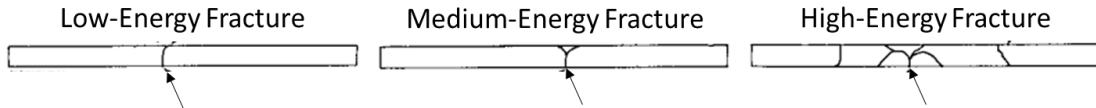


**Figure 45. Schematics of low-, medium-, and high-energy fracture paths. Arrows indicate fracture origins.** Adapted from “Fractography of Ceramics and Glasses”, by George Quinn, Third Edition.<sup>7</sup> Republished courtesy of the National Institute for Standards and Technology.

As the crack propagates, the rate of elastic strain energy liberation increases. In the early stages of crack propagation, the rate of energy release is relatively low, and the strain energy is absorbed by the creation of two smooth surfaces. The smooth region of the fracture surface surrounding the origin is known as the fracture mirror. The mirror is subsequently surrounded by slightly rougher region known as the “mist” region, named so for its appearance. Mist is more difficult to observe in polycrystalline ceramics than it is in glasses since the microstructure of polycrystalline materials can obscure the fine mist features.

The next region after mist is the hackle region, which contains features similar in appearance to large wires which point toward the fracture origin. In glasses, the edge of the fracture mirror is often defined by the onset of mist, but in polycrystalline materials it is commonly defined as the onset of hackle. Parameters calculated using the different mirror radii are also usually designated by which boundary was used to calculate them.

Equation 22 is in line with the current understandings of mist. Mist arises when the rate of elastic energy being released during fracture exceeds that necessary to generate two smooth mirror surfaces. At this velocity, secondary cracks ahead of the primary crack are induced by the stress field in this “process zone”. When the primary crack overtakes the secondary cracks, the interaction of the two leaves remnants on the fracture surfaces known as mist.<sup>2</sup> When the secondary cracks achieve such a velocity that the primary crack can no longer overtake them, hackle ensues. Therefore, it logically follows that a very fast crack releases elastic strain energy very quickly, generates secondary cracks at an earlier stage than a slow crack, exhibits earlier onset of mist, and has a smaller fracture mirror.

Other fracture markings such as scarpes, Wallner lines, twist hackle, and arrest lines have important implications and uses as well, but they are not addressed in this work. For

more information, we direct the reader to George Quinn's "Fractography of Ceramics and Glasses", Third Edition, a guide published by the National Institute for Standard and Technology (NIST) and available free of charge online. A schematic representation of some common fracture markings can be found in Figure 46.

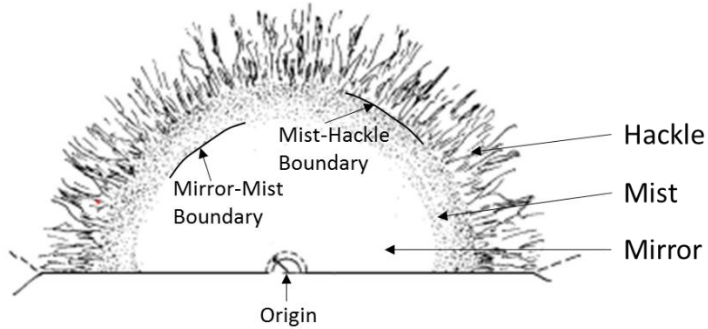


**Figure 46. Some common fracture markings from a brittle fracture.** Adapted from "Fractography of Ceramics and Glasses", Third Edition, by George Quinn.<sup>7</sup> Republished courtesy of the National Institute for Standards and Technology.

In this chapter, flaw sizes and mirror radii are measured, and  $A$  and  $K_{IC}$  are calculated using the available fracture mechanics relations previously discussed. The tabulation of these parameters is valuable to the field of fracture mechanics as the models proposed for the creation of various fracture features should be compared with experimental data in order to verify their practical applicability.

## B. Materials and Methods

SiAlON powder blends containing either aluminum tri *sec*-butoxide (ASB) or Al<sub>2</sub>O<sub>3</sub> powder were generated by methods similar to those outlined in Chapter III. For ASB blends, the organometallic precursor aluminum tri *sec*-butoxide (ASB, 97%, Sigma Aldrich, USA) was extracted in a glovebox under continuously purified high-purity N<sub>2</sub>, sealed, and removed from the glovebox. Directly before incorporating the powder components into suspension, the ASB was unsealed and immediately dissolved in an anhydrous isopropanol suspension medium (99.5%, Sigma Aldrich, USA). Then, powder constituents H<sub>3</sub>BO<sub>3</sub> (technical grade, Rose Mill Co., USA), Y<sub>2</sub>O<sub>3</sub> (38 nm, Nanografi

Nanotechnology, Turkey), AlN ( $D_{50} = 8 \mu\text{m}$ , Alfa Aesar, USA), and  $\text{Si}_3\text{N}_4$  (UBE SNE-10, >95 wt%  $\alpha$  phase, UBE, Japan) were incorporated into suspension. For  $\text{Al}_2\text{O}_3$  blends, which do not contain ASB, the  $\text{Al}_2\text{O}_3$  powder (A16 Grade, Almatis GmbH, Germany) was incorporated along with all other powder constituents. Suspensions were ball milled for 24 hours in high-density polyethylene jars charged with approximately 1.5 kg of  $\text{ZrO}_2$  spheres (YTZ, 10 mm diameter, Tosoh, Japan). Milled suspensions were dried in a rotovap equipped with a water bath held at 80 °C. See Table I in Chapter II for further raw material information.

The experimental design of this work involves six SiAlON blends: four ASB-containing blends and two  $\text{Al}_2\text{O}_3$ -containing blends. The four ASB blends are modified with varying concentrations of  $\text{H}_3\text{BO}_3$  and will be denoted ASB-B0, ASB-B1, ASB-B2, and ASB-B3. These are the SiAlON blends characterized in Chapter III of this thesis. The  $\text{Al}_2\text{O}_3$  blends will be denoted  $\text{Al}_2\text{O}_3$ -B0 and  $\text{Al}_2\text{O}_3$ -B2, where  $\text{Al}_2\text{O}_3$ -B2 has the same concentration of  $\text{H}_3\text{BO}_3$  as ASB-B2. Their compositions can be found in Table IV.

**Table IV. SiAlON Powder Blend Compositions for Fractographic Studies with Raw Materials in wt%**

		Base Composition				Additives		
		Sample						
		Designation	$\text{Si}_3\text{N}_4$	AlN	ASB	$\text{Al}_2\text{O}_3$	$\text{Y}_2\text{O}_3$	$\text{H}_3\text{BO}_3$
<b>ASB</b>	<b>ASB-B0</b>	81.03	3.49	15.48	0	4.10	0.00	
	<b>ASB-B1</b>	81.03	3.49	15.48	0	4.10	0.04	
	<b>Blends</b>	<b>ASB-B2</b>	81.03	3.49	15.48	0	4.10	1.00
		<b>ASB-B3</b>	81.03	3.49	15.48	0	4.10	3.00
<b><math>\text{Al}_2\text{O}_3</math></b>	<b><math>\text{Al}_2\text{O}_3</math>-B0</b>	92.73	3.79	0	3.48	4.45	0.00	
<b>Blends</b>	<b><math>\text{Al}_2\text{O}_3</math>-B2</b>	92.73	3.79	0	3.48	4.45	1.00	

SiAlON powder blends were hot pressed in 1.5 x 2-inch rectangular graphite dies lined with boron nitride following the sintering profiles presented in Figure 29. Sintering was carried out under vacuum until 1400 °C, at which point ~800 torr of UHP N<sub>2</sub> was introduced into the chamber. Sintered SiAlONs were machined into ASTM “B” type flexure specimens with a final surface finish of 500 grit (~35  $\mu\text{m}$ ).<sup>143</sup> Densities of as-

machined flexure specimens were calculated via the immersion technique in room-temperature (23 °C) deionized water. Five specimens from each composition were fractured using an Instron 5566 loading frame (Instron, USA) and fully articulating four point ¼-pt flexure fixtures (Wyoming Test Fixtures, USA) at a crosshead speed of 0.5 mm/min. Load vs. displacement curves were generated and converted to stress strain curves using Equations 19 and 20.

These formulas are specific to the situation of four point ¼-pt bending of a rectangular rod and are derived from classical beam theory. Note that any deflection of the fixtures or loading frame during the experiment were subtracted by applying loads up to 1000 N to a large bar of high-purity Al<sub>2</sub>O<sub>3</sub> and measuring the displacement during the experiment. It is assumed that the Al<sub>2</sub>O<sub>3</sub> bar does not deflect, and any displacement measured is therefore erroneous. This procedure is referred to as correcting for “machine compliance”, and can be found in Appendix C.

The pulse echo technique was also performed to assess elastic modulus. It involves the calculation of elastic modulus by measuring the time it takes for transverse and longitudinal ultrasonic pulses to propagate through the thickness of a specimen. The shorter the time, the greater the speed of sound is in a material, and the greater the elastic modulus is. First, Poisson's ratio is calculated by Equation 23

$$\nu = \frac{1-2\left(\frac{V_T}{V_L}\right)^2}{2-2\left(\frac{V_T}{V_L}\right)^2} \quad (23)$$

where  $\nu$  is Poisson's ratio,  $V_T$  is the velocity of the transverse wave (sample thickness ÷ ½ round trip time), and  $V_L$  is the velocity of the longitudinal wave. Then, elastic modulus ( $E$ ) can be calculated by Equation 24:

$$E = V_L^2 \rho \frac{(1+\nu)(1-2\nu)}{1-\nu} \quad (24)$$

where  $\rho$  is the specimen density. A brief comment on the consistency of the two techniques for calculating elastic modulus (stress-strain curve and pulse echo) is made.

## 1. Fractographic procedure

Fractographic analysis was performed on every specimen fractured in this study. A small piece of Scotch tape was placed on the compressive (top) surface of the specimen in order to retain as many fragments as possible. A layer of cushion material was placed

directly below the specimen so as to prevent secondary fractures induced by the specimen striking the bottom of the fixtures after fracture. The experimental setup for flexure experiments is given in Figure 47.



**Figure 47. Experimental setup for four point ¼-pt flexure experiments.**

Loads were applied at a constant rate until fracture. The instrument recorded the load and corresponding travel of the crosshead at a rate of 10 data points per second. Fragments were collected and carefully packaged to prevent abrasion of the fracture surfaces. Each specimen in turn was reassembled in order to observe the crack path, and each fragment was indexed. Fractures typically exhibit characteristic paths which can inform the fractographer about the point along the specimen at which the fracture began. Once this location was determined, the fracture surfaces of fragments on either side of the fracture origin were inspected optically using the naked eye, a Bausch and Lomb 7X magnification jeweler's loupe, and a stereo optical microscope with normal incidence illumination. The fragment containing the most information concerning the fracture origin was selected and viewed under a Wild M3Z stereo optical microscope at 40X magnification using grazing incidence illumination. Optical images of fracture origins were collected using a SPOT Insight 2 color digital camera and SPOT Basic software.

Scanning electron microscopy (SEM) and energy dispersive spectroscopy (EDS) were performed using an FEI Quanta 200 Environmental Scanning Electron Microscope (ESEM) (Thermo Fisher Scientific, USA) to collect images for measurement of various

fracture surface markings. These include the flaw size and fracture mirror size, as well as the flaw location. While stereo optical microscopy is generally more powerful for the observation of fracture markings, the high strength and consequently small fracture mirrors of the present specimens rendered SEM more applicable for accurate measurement. Critical flaw sizes were taken as  $\frac{1}{2}$  the radii of the flaws parallel to the tensile surface for internal flaws and flaw depths for surface flaws. Fracture mirror sizes were taken as a radii of the mirrors from the flaw edges to mirror-hackle boundaries parallel to the tensile surfaces.

### C. Results and Discussion

The immersion densities of the flexure specimens are detailed in Figure 48. It was found that all SiAlONs exhibited comparable and high densities ( $\sim 3.250\text{-}3.260 \text{ g/cm}^3$ ) except the most boron-rich ASB-containing blend, ASB-B3, which had a density of  $3.228 \pm 0.001 \text{ g/cm}^3$ . Also notable is that all ASB-containing SiAlONs exhibited higher densities than their  $\text{Al}_2\text{O}_3$ -containing counterparts.

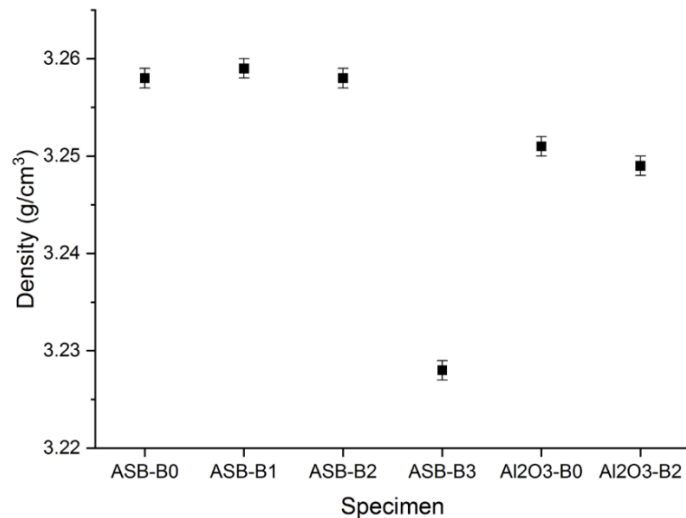


**Figure 48.** Immersion densities of ASB- and  $\text{Al}_2\text{O}_3$ -containing SiAlONs with varying boron concentrations. All SiAlONs exhibited high densities, but the lowest density SiAlON was ASB-B3, the most boron-rich ASB-route SiAlON. Error bars represent the statistical uncertainty of the measurement technique.

The average flexural strengths of the SiAlONs can be found in Figure 49. All SiAlONs exhibited comparable strengths on the order of 800-900 MPa except ASB-B3, which exhibited an average flexural strength of  $1016 \pm 107$  MPa, with the strongest specimen having a strength of 1164 MPa, despite its comparatively low density.

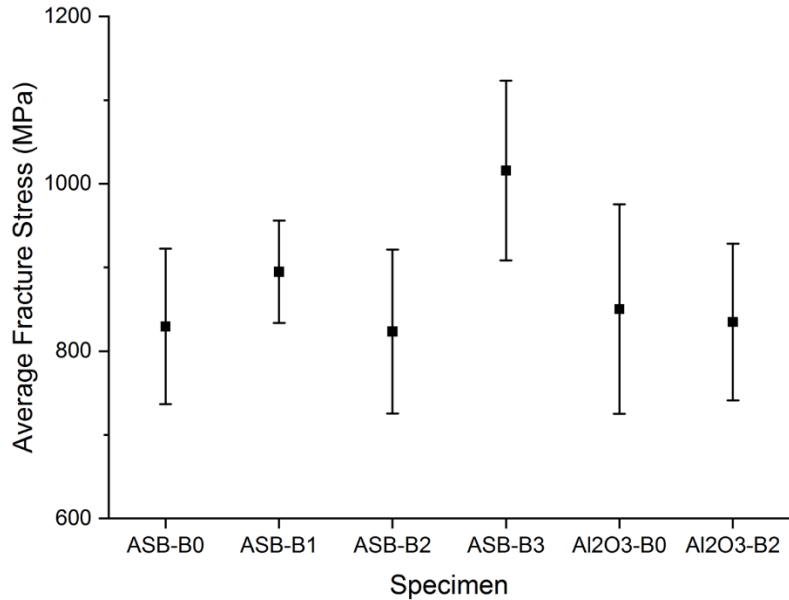


**Figure 49. Flexural strengths of SiAlONs fabricated using both ASB and  $\text{Al}_2\text{O}_3$ . ASB-B3, the most boron-rich SiAlON, exhibited superior flexural strengths to the other SiAlONs fractured. Error bars represent one standard deviation of fracture stress.**

The stress strain curves for all six SiAlONs are found in Figure 50. It is clear that ASB-B3 exhibited both greater fracture stresses as well as greater fracture strains. The slope of the linear region of the stress strain curve is the elastic modulus, as per Hooke's law (Equation 25), where  $\varepsilon$  is axial strain and  $E$  is elastic modulus.

$$\sigma = E\varepsilon \quad (25)$$

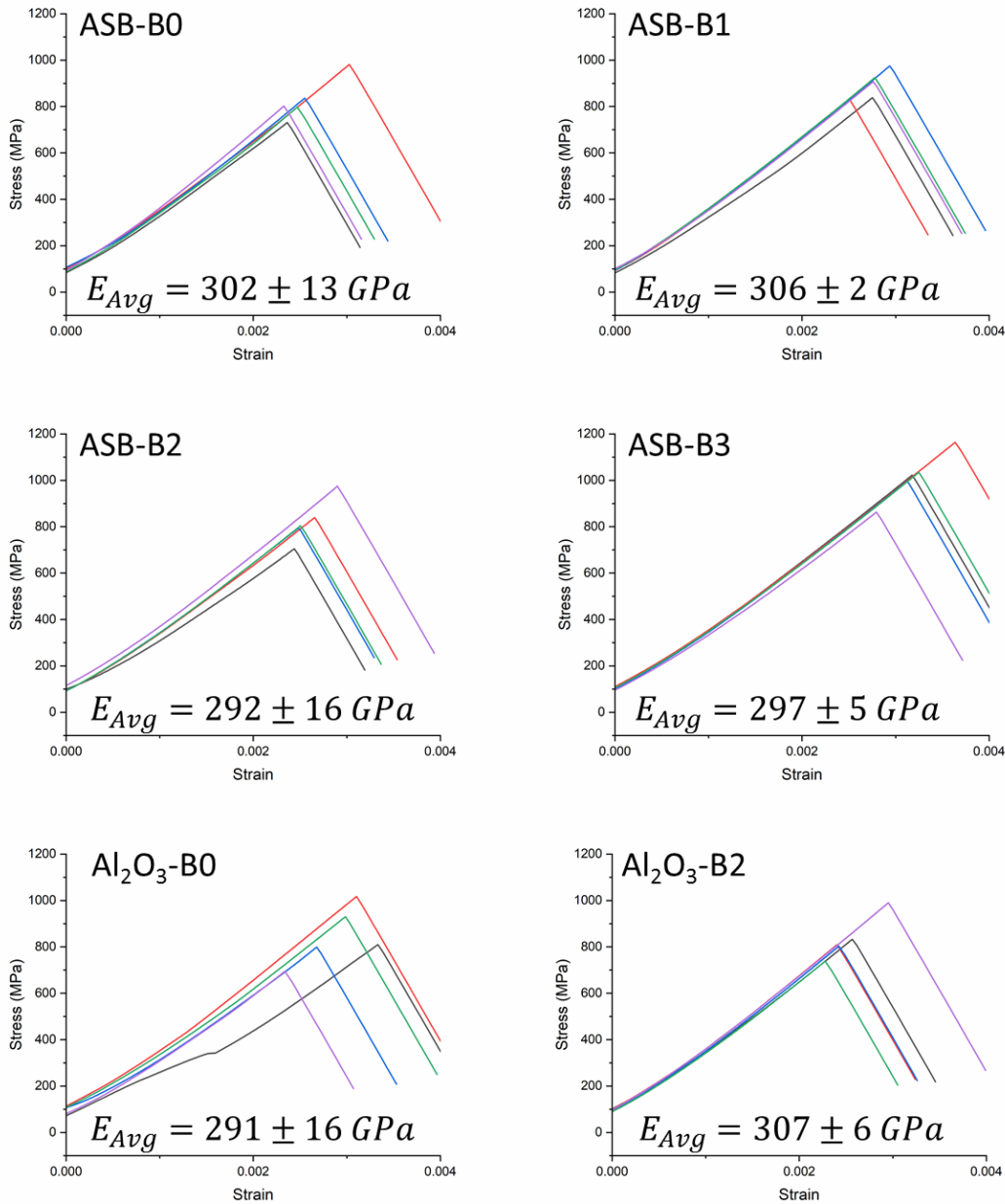


**Figure 50.** Stress-strain curves for SiAlONs synthesized by either ASB or  $\text{Al}_2\text{O}_3$  powder and containing various amounts of boron; a) ASB-B0, b) ASB-B1, c) ASB-B2, d) ASB-B3, e)  $\text{Al}_2\text{O}_3$ -B0, and f)  $\text{Al}_2\text{O}_3$ -B2. Elastic modulus values are the average of the slopes of the five curves,  $\pm 1$  standard deviation.

While the slopes of the linear portions of the stress-strain curves are taken as the “true” elastic moduli in this work, the pulse echo technique was also employed to calculate elastic modulus. The correlation between the two measurements is found in Figure 51. The

dotted lines represent an interval of  $\pm 5\%$ . The pulse echo technique appears to yield slightly higher E values for these SiAlONs. Pulse echo experiments enable the calculation of what is known as “zero-strain” elastic modulus, while the stress-strain curve techniques yield “finite-strain” elastic moduli. There appears to be limited comparison between the two.<sup>158</sup>

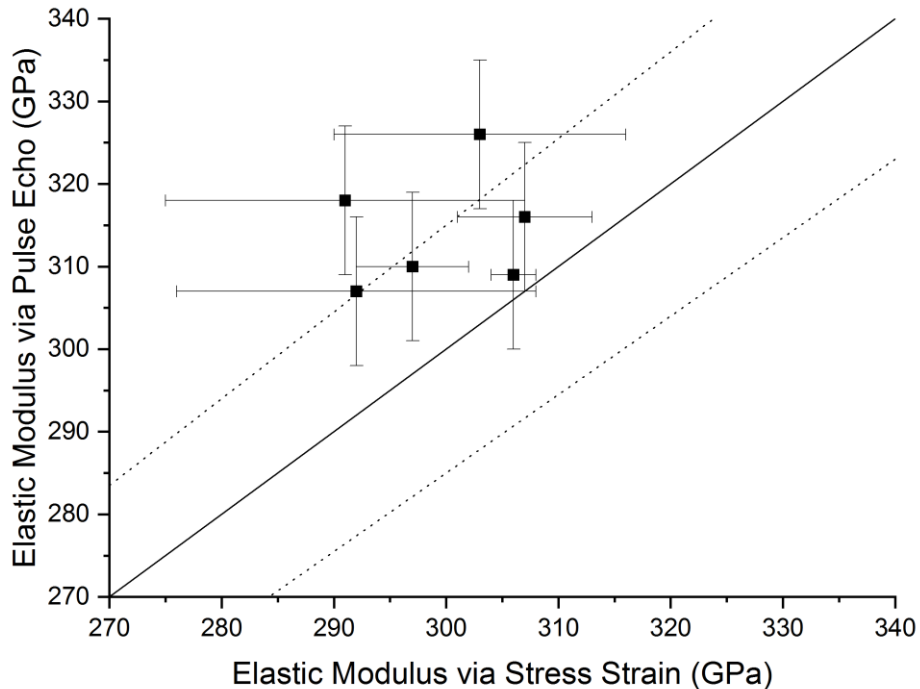


**Figure 51.** Correlation between elastic moduli calculated by the stress-strain curve and pulse echo techniques. Dotted lines represent an interval of  $\pm 5\%$ . The pulse echo technique appears to yield slightly higher values for E.

Fractographic analysis was performed according to the procedures outlined by NIST for all SiAlONs. Visual observation of fracture patterns from specimen reassembly of corresponding fragments revealed primary cracks at the tensile surfaces along with secondary cracks indicating medium to high energy fracture for most of the samples. Figure 52 shows representative fracture patterns and the associated fracture stresses for those particular specimens. Primary cracks travelled perpendicularly to the surface tensile stress while secondary cracks deviated from the perpendicular direction of stress, as commonly observed in flexural testing. Another important feature is the presence of compression

curls, as can be seen in Figure 52, in which the tensile surfaces of the specimens is on the bottom. Compression curls typically originate by branching of the primary crack, forming a ‘T’ shaped piece on the opposite face of the crack origin due to the crack encountering the compressive region. Note the reasonably repeatable characteristic crack paths, and the degree of branching that occurs with increasing fracture stress.

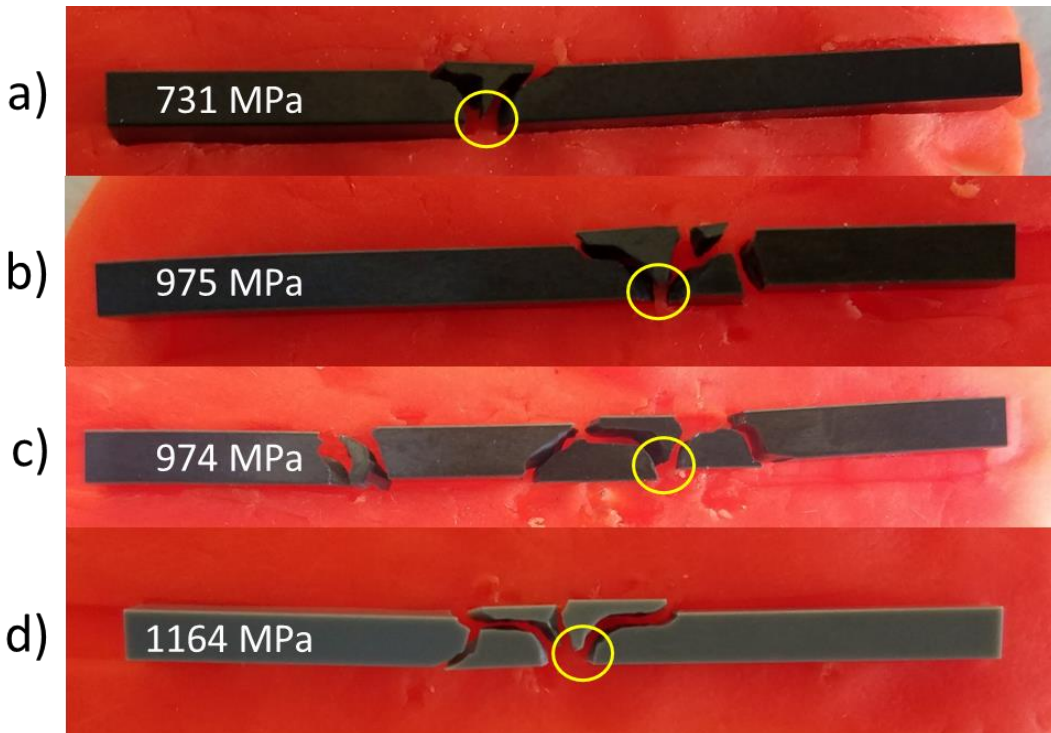


**Figure 52.** Selected fractured specimens of a) zero-boron SiAlON ASB-B0 (low energy fracture), b) low-boron SiAlON ASB-B1 (medium energy fracture), c) medium-boron SiAlON ASB-B2 (medium-high energy fracture), and c) boron-rich SiAlON ASB-B3 (medium-high energy fracture). Yellow circles indicate the region of crack initiation. Fracture stresses for these particular specimens is included for reference.

Fracture surfaces were examined in order to identify and measure the critical flaws as well as to measure the fracture mirror radii. Some examples of fracture origins can be found in Figures 53, 54, 55, 56, 57, and 58. These figures include the observed fracture mirror boundary with yellow borders, and where applicable, EDS spectra elucidating any chemical variation of the fracture origins.

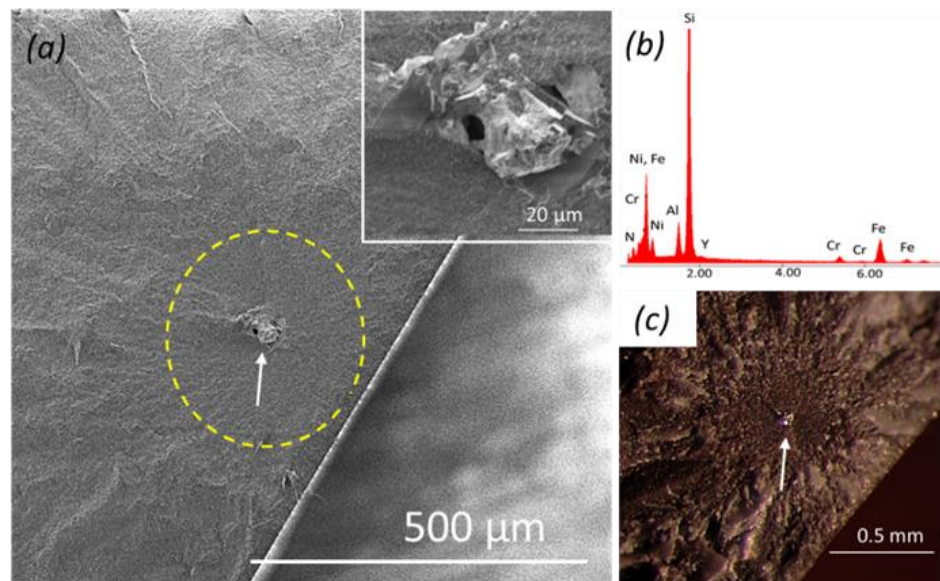


**Figure 53.** (a) SEM micrograph indicating the fracture origin and mirror boundary (dotted line) for a zero-boron SiAlON ASB-B0 specimen. (b) EDS showed that the critical flaw was a (Fe, Cr, Ni)-rich inclusion. (c) Fracture origin can also be clearly seen from the optical micrograph.

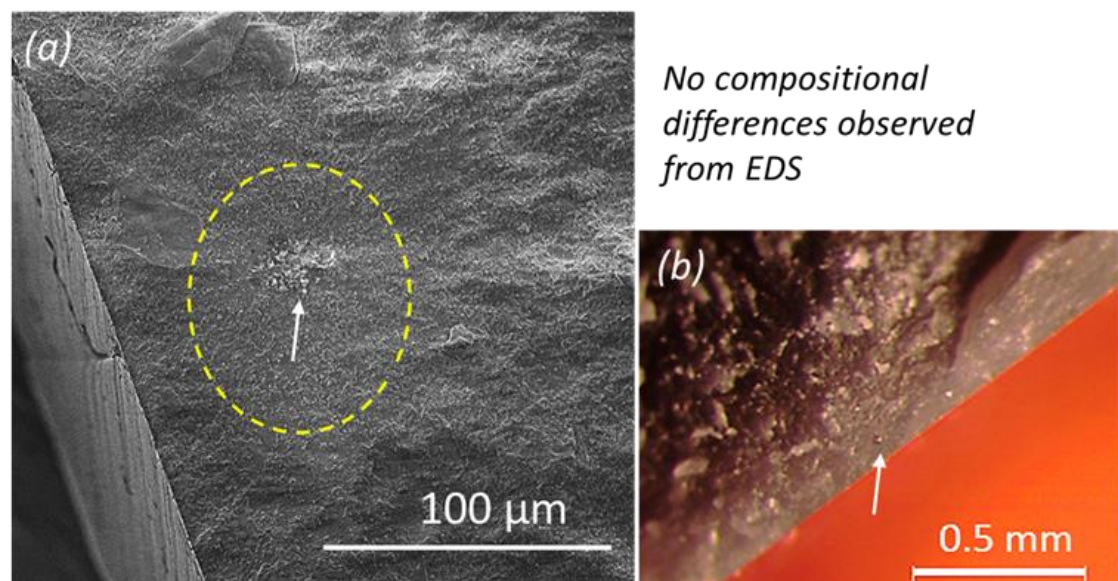


**Figure 54.** Fracture origin and mirror boundary region for a zero-boron SiAlON Al<sub>2</sub>O<sub>3</sub>-B0 specimen indicated on (a) SEM and (b) optical micrographs.

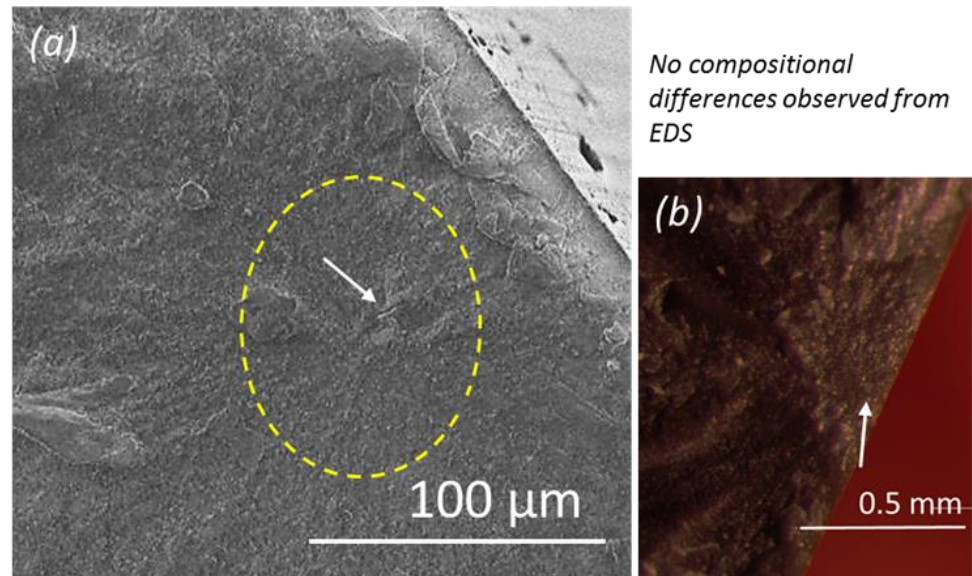


**Figure 55.** Fracture origin for a low-boron SiAlON ASB-B1 specimen indicated by (a) SEM and (b) optical micrographs. Mirror (dotted circle) region is relatively unclear compared to the cases with foreign inclusions as fracture origins.

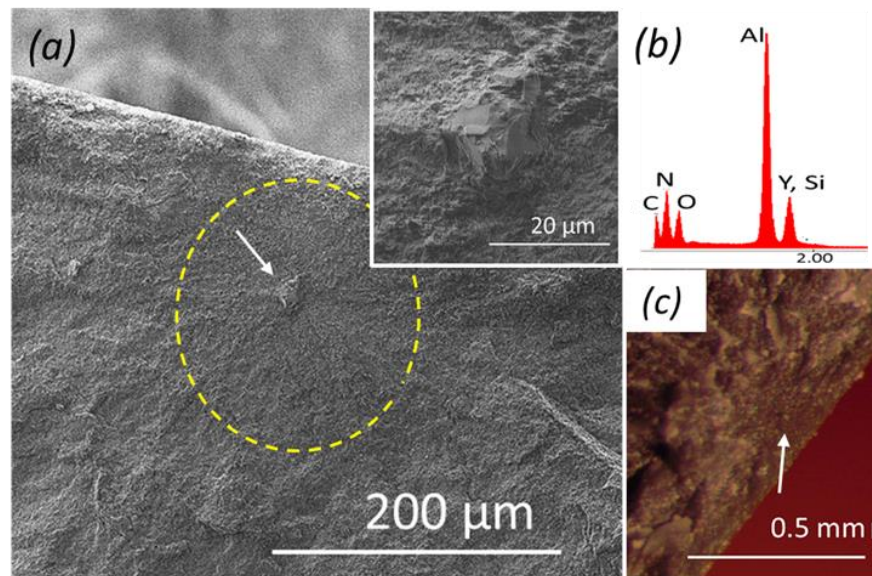


**Figure 56.** (a) SEM micrograph indicating fracture origin and mirror boundary (dotted line) for a medium-boron SiAlON ASB-B2 specimen. (b) EDS showed that the flaw at fracture origin was an Al-rich inclusion. (c) The fracture origin can also be seen from optical microscopy.

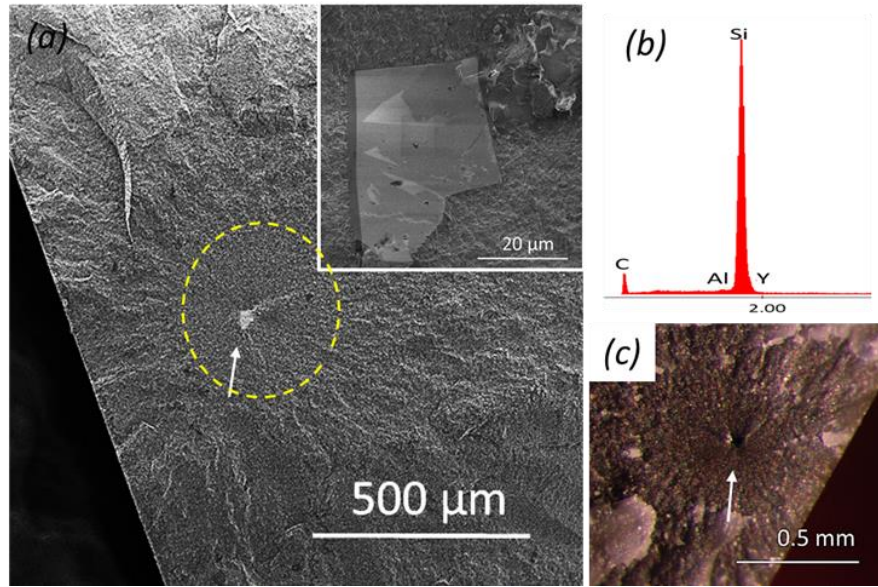


**Figure 57.** (a) SEM micrograph indicating fracture origin and mirror boundary (dotted line) for a medium-boron SiAlON Al<sub>2</sub>O<sub>3</sub>-B<sub>2</sub> specimen. (b) EDS showed that the flaw at fracture origin was Si-rich inclusion also containing carbon, possibly indicating a SiC grain. (c) Fracture origin clearly identified from optical micrograph.

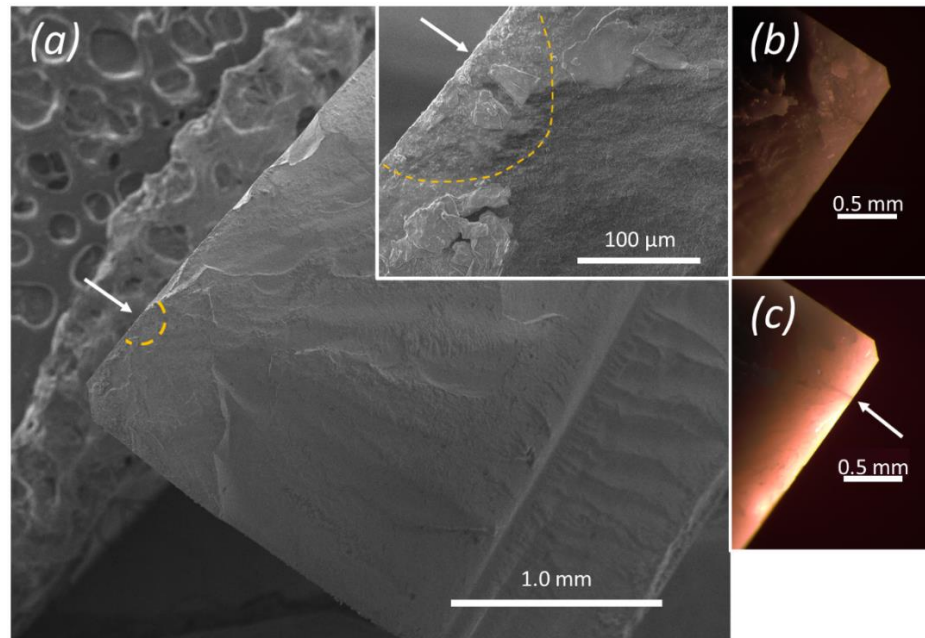


**Figure 58.** (a) Fracture origin (surface flaw) for a high-boron SiAlON ASB-B3 specimen indicated on SEM. (b) Optical micrograph has a subtle surface crack as indicated. (c) Transillumination reveals the crack prominently.

As evidenced by the preceding figures, fracture mirrors were readily observable for the majority of SiAlONs in this study. The important exception to this was boron-rich ASB-B3. This SiAlON was lighter in color than the rest and seemed to exhibit some slight optical translucency when illuminated at a grazing angle. Additionally, the fracture of these specimens seemed to originate at subtle surface flaws such as machining cracks rather than at inclusions as in the majority of other SiAlONs in the study. Consequently, 4 of the 5 ASB-B3 specimens account for 4 of the 5 strongest SiAlONs of the 30 specimens fractured in this study.

The fracture surface contains a bounty of qualitative and quantitative information. Mirror constants and  $K_{IC}$  values were calculated from measurements of mirror radius and flaw size, respectively. The general procedure for making these measurements can be found in Figure 59, and the results of this analysis are summarized in Table V.

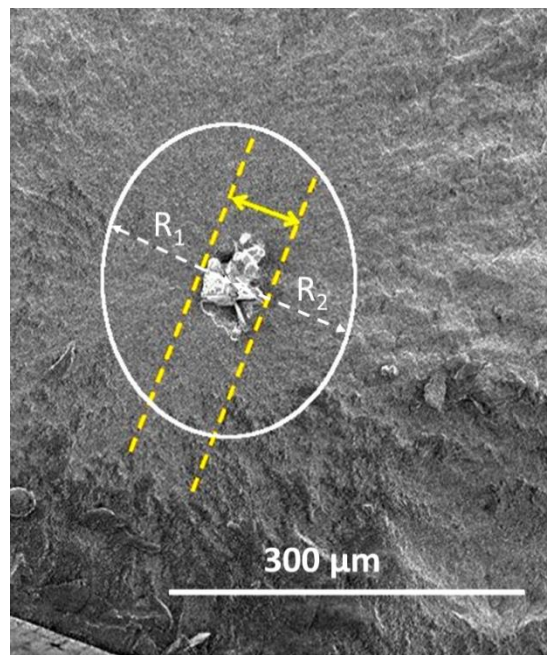


**Figure 59.** Example showing measurement of fracture mirror sizes and flaw sizes for a SiAlON synthesized by the ASB route containing zero boron (ASB-B0, Sample 3). Mirror size was taken as the average of radii ( $R_1$  and  $R_2$ ) along the direction of approximately equivalent tensile stress. Flaw size was taken as one-half the axis length of the flaw parallel to the tensile surface for internal flaws, and flaw depth for surface flaws.

**Table V. Maximum failure stresses ( $\sigma$ ), stresses at fracture origins ( $\sigma_f$ ), measured mirror radii (r), calculated mirror constants (A), flaw sizes (c), geometric constants (Y), and toughness ( $K_{IC}$ ) values for samples, wherever possible, from different compositional blends. (NI: Not identifiable)**

Sample	#	$\sigma$	$\sigma_f$	r	A	c	Y	$K_{IC}$
Designation		(MPa)	(MPa)	(mm)	(MPa $\cdot$ m $^{1/2}$ )	(mm)		(MPa $\cdot$ m $^{1/2}$ )
<b>ASB-B0</b>	1	731	657	0.11	6.9	0.0165	1.47	3.92
	3	836	683	0.08	6.1	0.0275	1.30	4.66
	4	798	650	0.12	7.2	0.0365	1.47	5.78
	5	801	631	0.11	6.7	0.0315	1.47	5.21
<b>ASB-B1</b>	4	924	924	0.08	8.1	0.0490	1.17	7.57
<b>ASB-B2</b>	1	705	688	0.11	7.2	0.0205	1.13	3.52
	2	839	750	0.21	10.8	0.0130	1.77	4.79
	3	794	733	0.07	6.2	0.0150	1.30	3.69
	4	804	804	0.15	9.7	NI	NI	NI
	5	974	922	0.04	6.0	0.0090	1.30	3.60
<b>ASB-B3</b>	4	1034	1034	0.04	6.7	0.0040	1.51	3.12
<b>Al<sub>2</sub>O<sub>3</sub>-B0</b>	1	810	810	0.20	11.5	NI	NI	NI
	2	1017	982	0.02	4.7	0.0210	1.30	5.85
<b>Al<sub>2</sub>O<sub>3</sub>-B2</b>	1	833	700	0.19	9.7	0.0505	1.47	7.31
	2	809	609	0.13	7.0	0.0235	1.30	3.84
	3	803	793	0.18	10.6	NI	NI	NI
	4	738	738	0.10	7.4	NI	NI	NI
	5	990	646	0.10	6.5	0.0150	1.30	3.25

To assess the validity of these measurements and the calculations performed with the current models (Equations 21 and 22), all data from this study were plotted alongside curves representing reasonable values for these materials. These plots can be found in Figure 60 and Figure 61. For the analysis of fracture stress relative to flaw size, data resemble a decreasing power law trend and fall inside bounds defined by  $K_{IC}$ :Y ratios of 1.69 and 5.31 MPa $\cdot$ m $^{1/2}$ . These ratios correspond to  $K_{IC}$  values of 3 and 6 MPa $\cdot$ m $^{1/2}$  and Y values of 1.77 and 1.13, respectively. These  $K_{IC}$  values were chosen because they are reasonable fracture toughness values for SiAlONs, and these Y values are the most extreme

used in this study. While a power law is exhibited for this relationship, the exponent found by fitting all data is  $-0.16 \pm 0.09$ , as opposed to the  $-0.5$  expected from fracture mechanics.

The relationship between fracture stress and fracture mirror radius exhibits similar characteristics. As expected, mirror radius decreases with increasing fracture strength. Measured data can all be found within an interval defined by  $A$  values of 6 and 12  $\text{MPa} \cdot \text{m}^{1/2}$ . Data obey a power law similar to the strength vs. flaw size relationship. However, similarly to the strength vs. flaw size data, fitting of this data yields an exponent of  $-0.18 \pm 0.07$ .

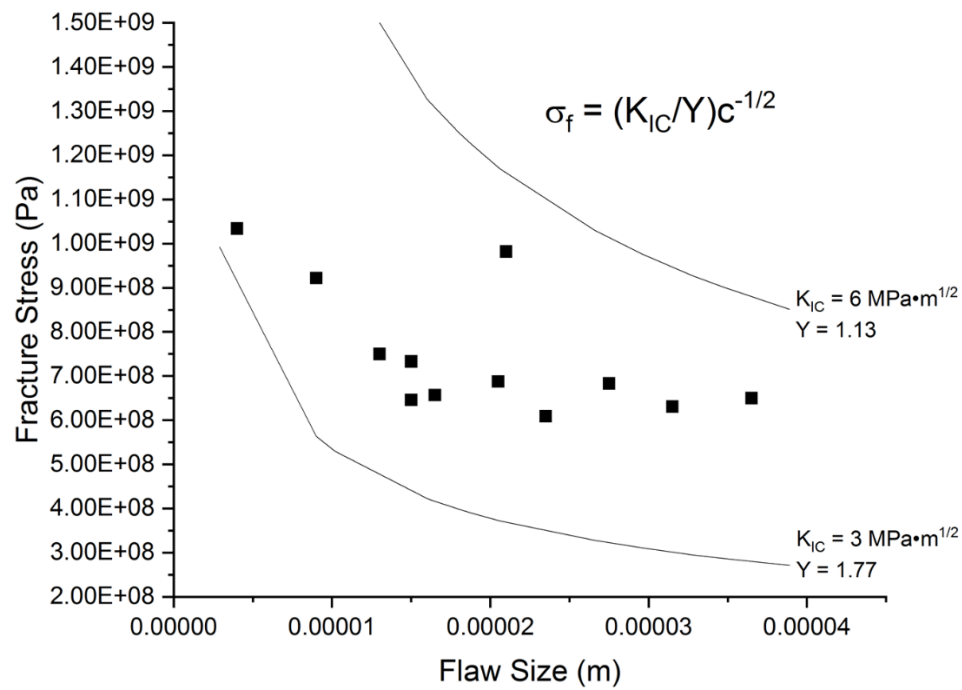


**Figure 60.** Fracture stress as a function of flaw size for all samples which exhibited measurable critical flaws. All data fall between within a range defined by  $1.69 < K_{IC}/Y < 5.31 \text{ MPa} \cdot \text{m}^{1/2}$ .

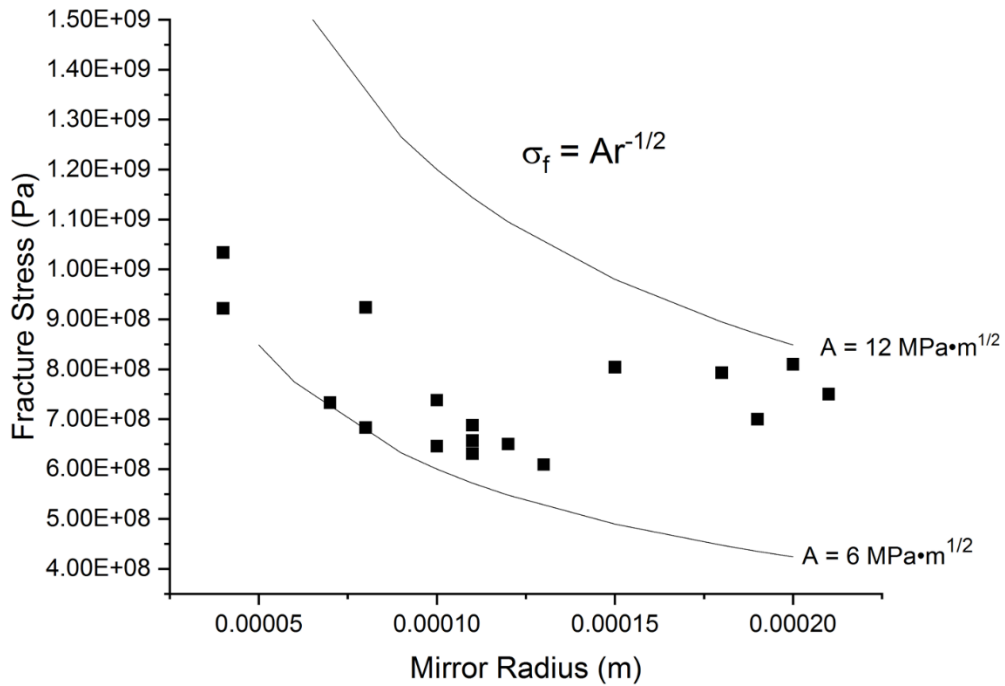


**Figure 61.** Fracture stress as a function of mirror radius for all samples which exhibited measurable fracture mirrors. All data fall within a range defined by  $6 < A < 12 \text{ MPa}\cdot\text{m}^{1/2}$ .

#### D. Conclusions

SiAlON specimens were synthesized via both an aluminum-containing organometallic precursor, aluminum tri *sec*-butoxide (ASB), and  $\text{Al}_2\text{O}_3$  powder. Additionally, SiAlONs containing varying concentrations of boron-containing precursor boric acid ( $\text{H}_3\text{BO}_3$ ) were synthesized. Four point  $\frac{1}{4}$ -pt flexure experiments were performed, and full fractographic analysis was carried out. It was found at all SiAlONs exhibited comparable and high fracture stresses in the realm of 850 MPa except the most boron-rich ASB-route SiAlON (ASB-B3), which had an average flexural strength of  $1016 \pm 107$  MPa. Two types of fracture origins were identified: internal inclusions and surface flaws such as machining cracks. Most specimens failed from inclusions, but the strongest sample set ASB-B3 exhibited subtle and elusive surface flaws, hence its higher strength. Measurements of critical flaw size enabled the calculation of fracture toughness ( $K_{\text{IC}}$ ), and

measurements of fracture mirror radius allowed for the calculation of fracture mirror constant (A).  $K_{IC}$  ranged from 3.12 to 7.57 MPa•m<sup>1/2</sup>, and A ranged from 4.7 to 11.5 MPa•m<sup>1/2</sup>. When all data are plotted together, both  $K_{IC}$  vs critical flaw size and A vs mirror radius seem to generally follow a power law, as expected from the fracture mechanics relations available, and fall within reasonable bounds. Ultimately, the tabulation of more enigmatic material properties like  $K_{IC}$  and A from laboratory data is useful to fractographers in industry. Components in use may break under unknown loads, but if the critical flaw or mirror radius can be measured, the stress at the fracture origin may be estimated through fracture mechanics.

## V. SUMMARY AND CONCLUSIONS

In this work, the roles of two soluble molecular precursors were investigated for the densification, bonding, microstructural development, and ultimate structural properties of SiAlON ceramics. The liquid organometallic precursor aluminum tri *sec*-butoxide (ASB) was incorporated in replacement of conventional Al<sub>2</sub>O<sub>3</sub> powder to introduce Al and O into the Si<sub>3</sub>N<sub>4</sub> lattice. The soluble powder H<sub>3</sub>BO<sub>3</sub> was incorporated in order to investigate the potential for a powder-route silicon-based ceramic containing boron. The focus of the Al-organometallic portion of this work is on the synthesis of a SiAlON ceramic from Si<sub>3</sub>N<sub>4</sub> powder and a molecular precursor. The focus of the boron aspect of this work is on the characterization and resultant structural properties of the boron-containing SiAlONs.

The purpose of the organic precursor was to make a fine, homogeneous distribution of solute atoms available to the Si<sub>3</sub>N<sub>4</sub> powder particle surfaces. A homogeneous distribution of Al was achieved in SiAlON powder blends containing ASB, while those with Al<sub>2</sub>O<sub>3</sub> powder exhibited regions of high Al concentration which are attributed to Al<sub>2</sub>O<sub>3</sub> particles or agglomerates. The homogeneity of the Al contributed by ASB persisted even after heating to 1000 °C. No evidence of Al<sub>2</sub>O<sub>3</sub> crystallization was observed via EDS mapping, XRD, DTA, or HT-SEM in ASB-SiAlON blends heated to various temperatures. The β' phase unit cell volumes of ASB-route SiAlONs were higher for low sintering times and for low liquid phase concentrations, indicating enhanced solid solution of Al and O in the Si<sub>3</sub>N<sub>4</sub> lattice. Sintered ASB-route SiAlONs exhibited higher density than their Al<sub>2</sub>O<sub>3</sub>-route counterparts at very low liquid phase sintering additive concentrations. Ultimately, the ASB route may enable liquid phase volumes which were previously inaccessible to SiAlONs, extending their use temperature and decreasing dependence on rare earth oxides.

Inspired by ultra-high temperature polymer-derived ceramic SiBCN, molecular precursor boric acid (H<sub>3</sub>BO<sub>3</sub>) was also investigated in order to understand the role of boron in a powder-route Si-based ceramic. Reasonably high densities were achieved for all B-SiAlONs. XRD revealed that with increasing boron concentration, the populations of second phases and residual α-Si<sub>3</sub>N<sub>4</sub> both decreased, until a single-phase β'-SiAlON was achieved at 3 wt% H<sub>3</sub>BO<sub>3</sub> (~1.03 at% B). Raman spectroscopy indicated that B exists in threefold coordination with N in the turbostratic structure (t-BN), reminiscent of the boron

coordination in SiBCN. No other boron coordinations were detected via  $^{11}\text{B}$  SS MAS-NMR. The incorporation of boron resulted in a gradual narrowing of the grain size distributions of SiAlONs, whose microstructures are typically characterized by a population of large, rod-like grains embedded in a fine-grained matrix. A nearly monomodal grain size distribution was achieved for the most boron-rich SiAlON. These analyses cumulatively indicate that t-BN induced by the  $\text{H}_3\text{BO}_3$  precursor inhibits the crystallization of second phases in the SiAlON grain boundary and narrows the grain size distribution.

Fractographic analysis of SiAlON flexure specimens with various concentrations of boron were performed to elucidate the failure mechanisms of these materials. It was found that the most boron-rich SiAlON, which was also processed via the ASB route, exhibited superior average flexural strengths ( $1016 \pm 107$  MPa) and primarily subtle surface flaws as fracture origins. SiAlONs with lower B content most often exhibited inclusions as fracture origins, either of foreign or native material. This is consistent with grain size and XRD analysis, which illustrated that abnormal grain growth and crystallization of second phases were suppressed by the incorporation of B.

Measurements of critical flaw size enabled the calculation of critical stress intensity factors ( $K_{\text{IC}}$ ), which ranged from 3.3 to 7.6  $\text{MPa}\cdot\text{m}^{1/2}$ . Fracture mirror radius measurements were used to calculate mirror constants (A) for these SiAlONs, which ranged from 4.7 to 11.5  $\text{MPa}\cdot\text{m}^{1/2}$ . When all data are plotted together, it appears that the fit for fracture stress vs both mirror radius and critical flaw size generally obeys a power law, as expected from fracture mechanics. A database of material parameters such as  $K_{\text{IC}}$  and A is important as it can be used to estimate fracture stresses of components in use for which the loading conditions at failure may be unknown. If a flaw size and/or mirror radius can be measured using fractographic techniques, then a fracture stress may be estimated using literature values.

In summary, the incorporation of molecular-level additives for SiAlON synthesis and properties was studied in depth. This investigation may lead to SiAlONs with extended use temperatures and greater reliability. It was found that molecular precursors to ceramics may be used as additives in powder-route SiAlONs, taking advantage of the unique opportunities these precursors present.

## VI. RECOMMENDATIONS FOR FUTURE WORK

While this thesis demonstrates the effective formation of a SiAlON through the use of aluminum-containing organometallic precursor aluminum tri *sec*-butoxide (ASB), the full scope of this precursor's potential has yet to be explored. The present work does not investigate the effect of dwelling temperature or pressure on final density or degree of solid solution. Decreasing these parameters would benefit the cost of manufacture of SiAlONs and render the strength of the graphite dies less critical.

This thesis uses final bulk density as a metric for the effectiveness of densification of ASB-route SiAlONs. However, greater insight may be obtained by calculating density throughout the sintering cycle by measuring the hot press ram position as a function of time or temperature. A digital data logger with sufficient recording rate coupled with a linear variable differential transformer (LVDT) position sensor would allow for *in-situ* density measurement. Densification as a function of time is important for the ASB portion of this work. Further, existing models for intermediate-stage densification in the presence of a liquid phase proposed by Kingery, *et al.* may be applied to assess whether the rate limiting process for densification is dissolution/reprecipitation of solid matrix phase in the liquid or diffusion through this grain boundary phase.<sup>159-160</sup> This determination, in addition to the calculation of grain boundary diffusion coefficients<sup>161</sup>, is very important for the portion of this work related to boron-containing SiAlONs.

Further, the specific decomposition mechanisms of the organometallic precursor ASB remain elusive. Mass spectrometry should be performed in conjunction with thermogravimetry in order to identify and quantify the volatile species evolved during pyrolytic decomposition. It remains unclear whether any carbon from the alkyl groups in the polymeric structure remains in the SiAlON system, or if it is all volatilized.

Finally, high-temperature structural properties of boron-containing SiAlONs should be investigated. It is suggested that either of the following measurements would provide valuable insight: i) strain as a function of time at constant temperature and load, or ii) strain as a function of temperature at constant load.

## VII. REFERENCES

1. Helms, H. E., Ceramic Applications in Turbine Engines. In *Ceramics for High-Performance Applications III*, Lenoe, E. M.; Katz, R. N.; Burke, J. J., Eds. Springer: Boston, MA, 1983; Vol. 1.
2. Rabinovitch, A.; Belizovsky, G.; Bahat, D., Origin of mist and hackle patterns in brittle fracture. *Phys. Rev. B* **2000**, *61* (22), 14968-74.
3. Kattimani, V. S.; Kondaka, S.; Lingamaneni, K. P., Hydroxyapatite—Past, Present, and Future in Bone Regeneration. *Bone Tissue Regener. Insights* **2016**, *7*, 9-19.
4. Münstermann, S.; Lian, J.; Bleck, W., Design of damage tolerance in high-strength steels. *Int. J. Mat. Res.* **2012**, *103*, 755-64.
5. Danzer, R.; Lube, T.; Supancic, P.; Damani, R., Fracture of Ceramics. *Adv. Eng. Mater.* **2008**, *10* (4), 275-98.
6. Kirchner, H. P.; Gruver, R. M.; Sotter, W. A., Characteristics of flaws at fracture origins and fracture stress-flaw size relations in various ceramics. *Mater. Sci. Eng.* **1976**, *22*, 147-156.
7. Quinn, G. D. (2020), NIST Recommended Practice Guide: Fractography of Glasses and Ceramics (National Institute for Standards and Technology, Gaithersburg, MD) NIST Special Publication (SP) 960-16, 3<sup>rd</sup> edition. <https://doi.org/10.6028/NIST.SP.960-16e3> Republished courtesy of the National Institute of Standards and Technology.
8. Myagkov, L. L.; Mahkamov, K.; Chainov, N. D.; Makhkamova, I., Advanced and conventional internal combustion engine materials. In *Alternative Fuels and Advanced Vehicle Technologies for Improved Environmental Performance*, Folkson, R., Ed. Woodhead Publishing: 2014.
9. Pollock, T. M.; Tin, S., Nickel-Based Superalloys for Advanced Turbine Engines: Chemistry, Microstructure and Properties. *J. Propuls. Power* **2006**, *22* (2), 361-374.
10. Donald, I. W.; McMillan, P. W., Review: Ceramic matrix composites. *J. Mater. Sci.* **1976**, *11*, 949-72.
11. Marshall, D. B.; Ritter, J. E., Reliability of advanced structural ceramics and ceramic matrix composites - A review. *Am. Ceram. Soc. Bull.* **1987**, *66* (2).
12. Basutkar, A. G.; Kolekar, A., A Review on Properties and Applications of Ceramic Matrix Composites. *IJRST* **2015**, *II* (XII), 28-30.
13. DiCarlo, J. A.; Yun, H.-M.; Morscher, G. N.; Bhatt, R. T., SiC/SiC Composites for 1200°C and Above. In *Handbook of Ceramic Composites*, Bansal, N. P., Ed. Kluwer Academic Publishers: New York, USA, 2005; pp 77-98.
14. Volkmann, E.; Tushev, K.; Koch, D.; Wilhelmi, C.; Göring, J.; Rezwan, K., Assessment of three oxide/oxide ceramic matrix composites: Mechanical performance and effects of heat treatments. *Compos. Part A Appl.* **2015**, *68*, 19-28.
15. Abraham, C. M., A Brief Historical Perspective on Dental Implants, Their Surface Coatings and Treatments. *Open Dent. J.* **2014**, *8*, 50-55.
16. Tomlins, P., Material types for tissue scaffolds. In *Characterisation and Design of Tissue Scaffolds*, Woodhead Publishing: 2016; pp 1-21.
17. Dubruille, J.-H.; Viguer, E.; Naour, G. L.; Dubruille, M.-T.; Auriol, M.; Charpentier, Y. L., Evaluation of Combinations of Titanium, Zirconia, and Alumina Implants with 2 Bone Fillers in the Dog. *Int. J. Oral Maxillofac. Implants* **1999**, *14* (2), 271-7.
18. Bränemark, P.-I.; Adell, R.; Albrektsson, T.; Lekholm, U.; Lundkvist, S.; Rockler, B., Osseointegrated titanium fixtures in the treatment of edentulousness. *Biomaterials* **1981**, *4* (1), 25-8.
19. Habibah, T. U.; Amlani, D. V.; Brizuela, M. Hydroxyapatite Dental Material. <https://www.ncbi.nlm.nih.gov/books/NBK513314/> (accessed January 14, 2022).

20. Hanifi, A.; Fathi, M. H., Bioresorbability Evaluation of Hydroxyapatite Nanopowders in a Stimulated Body Fluid Medium. *Iran. J. Pharm. Sci.* **2008**, *4* (2), 141-8.
21. Özkurt, Z.; Kazazoglu, E., Zirconia Dental Implants: A Literature Review. *J. Oral. Implantology* **2011**, *37* (3), 367-76.
22. Porter, D. L.; Evans, A. G.; Heuer, A. H., Transformation toughening in partially-stabilized zirconia (PSZ). *Acta Metallurgica* **1979**, *27*, 1649-54.
23. He, G.; Hirschfeld, D. A.; Cesarano, J., Processing and Mechanical Properties of Silicon Nitride Formed by Robocasting Aqueous Slurries. In *24th Annual Conference on Composites, Advanced Ceramics, Materials, and Structures: B: Ceramic Engineering and Science Proceedings, Volume 21, Issue 4*, 2000; pp 607-614.
24. Shao, H.; Liu, A.; Ke, X.; Sun, M.; He, Y.; Yang, X.; Fu, J.; Zhang, L.; Yang, G.; Liu, Y.; Xu, S.; Gou, Z., 3D robocasting magnesium-doped wollastonite/TCP bioceramic scaffolds with improved bone regeneration capacity in critical sized calvarial defects. *J. Mater. Chem. B* **2017**, *5* (16), 2941-2951.
25. Riley, F. L., Silicon Nitride and Related Materials. *J. Amer. Ceram. Soc.* **2004**, *83* (2), 245-265.
26. Hampshire, S., Silicon nitride ceramics – review of structure, processing and properties. *J. Achiev. Mater. Manuf. Eng.* **2007**, *24* (1), 43-50.
27. Klemm, H., Silicon Nitride for High Temperature Applications. *J. Amer. Ceram. Soc.* **2010**, *93* (6), 1501-22.
28. Jankoviak, A.; Valle, R.; Parlier, M., Potential of innovative ceramics for turbine applications. *HAL Archives* **2014**.
29. Silicon Nitride Market Research Report by Type, by End-use Industry, by Region - Global Forecast to 2027 - Cumulative Impact of COVID-19.  
[https://www.reportlinker.com/p06178455/Silicon-Nitride-Market-Research-Report-by-Type-by-End-use-Industry-by-Region-Global-Forecast-to-Cumulative-Impact-of-COVID-19.html?utm\\_source=GNW](https://www.reportlinker.com/p06178455/Silicon-Nitride-Market-Research-Report-by-Type-by-End-use-Industry-by-Region-Global-Forecast-to-Cumulative-Impact-of-COVID-19.html?utm_source=GNW) (accessed 1/12/2022).
30. Becher, P. F.; Sun, E. Y.; Plucknett, K. P.; Alexander, K. B.; Hsueh, C.-H.; Lin, H.-T.; Waters, S. B.; Westmoreland, C. G.; Kang, E.-S.; Hirao, K.; Brito, M. E., Microstructural Design of Silicon Nitride with Improved Fracture Toughness: I, Effects of Grain Shape and Size. *J. Amer. Ceram. Soc.* **2005**, *81* (11), 2821-2830.
31. Sun, E. Y.; Becher, P. F.; Plucknett, K. P.; Hsueh, C.-H.; Alexander, K. B.; Waters, S. B.; Hirao, K.; Brito, M. E., Microstructural Design of Silicon Nitride with Improved Fracture Toughness: II, Effects of Yttria and Alumina Additives. *J. Amer. Ceram. Soc.* **2005**, *81* (11), 2831-2840.
32. Pezzotti, G., Silicon Nitride: A Bioceramic with a Gift. *ACS Appl. Mater. Interfaces* **2019**, *11*, 26619-36.
33. Akin, S. R. K.; Garcia, C. B.; Webster, T. J., A comparative study of silicon nitride and SiAlON ceramics against *E. coli*. *Ceram. Int.* **2020**, *47* (2), 1837-43.
34. Fünfschilling, S.; Fett, T.; Hoffmann, M. J.; Oberacker, R.; Schwind, T.; Wippler, J.; Böhlke, T.; Özcoban, H.; Schneider, G. A.; Becher, P. F.; Krusic, J. J., Mechanisms of toughening in silicon nitrides: The roles of crack bridging and microstructure. *Acta Materialia* **2011**, *59* (10), 3978-3989.
35. Hirosaki, N.; Akimune, Y.; Mitomo, M., Effect of Grain Growth of beta-Silicon Nitride on Strength, Weibull Modulus, and Fracture Toughness. *J. Amer. Ceram. Soc.* **1993**, *76* (7), 1892-1894.
36. Hoffmann, M. J., Relationship between microstructure and mechanical properties of silicon nitride ceramics. *Pure Appl. Chem.* **1995**, *67* (6), 939-946.
37. Li, C.-W.; Lee, D.-J.; Lui, S.-C., R-Curve Behavior and Strength for In-Situ Reinforced Silicon Nitrides with Different Microstructures. *J. Am. Ceram. Soc.* **1992**, *75* (7), 1777-85.

38. Greg Hilmas, W. F., Jeremy Watts Method for toughening via the production of spiral architectures through powder loaded polymeric extrusion and toughened materials formed thereby. US20090075062A1, 2012.
39. Jack, K. H., Sialons and related nitrogen ceramics. *J. Mater. Sci.* **1976**, *11*, 1135-58.
40. Jack, K. H.; Wilson, W. I., Ceramics Based in the Si-Al-O-N and Related Systems. *Nat. Phys. Sci.* **1972**, *238*, 28-29.
41. Shen, Z.; Zhao, Z.; Peng, H.; Nygren, M., Formation of tough interlocking microstructures in silicon nitride ceramics by dynamic ripening. *Nature* **2002**, *417* (6886), 266-269.
42. McGarrity, K.; Tumurugoti, P.; Ning, K.; Shulman, H., Fractography of silicon nitride based ceramics to guide process improvements. *J. Eur. Ceram. Soc.* **2020**, *40* (14), 4746-4752.
43. Bando, Y., Weak Asymmetry in  $\beta$ -Si<sub>3</sub>N<sub>4</sub> as Revealed by Convergent-Beam Electron Diffraction. *Acta Cryst.* **1983**, *B39*, 185-89.
44. Wang, C.-M.; Pan, X.; Rühle, M., Silicon nitride crystal structure and observations of lattice defects. *J. Mater. Sci.* **1996**, *31*, 5281-98.
45. Ekström, T.; Nygren, M., SiAlON Ceramics. *J. Am. Ceram. Soc.* **1992**, *75* (2), 259-76.
46. Kato, K.; Inoue, Z.; Kijima, K.; Kawada, I.; Tanaka, H.; Yamane, T., Structural Approach to the Problem of Oxygen Content in Alpha Silicon Nitride. *J. Am. Ceram. Soc.* **1975**, *58* (3-4), 90-91.
47. Hampshire, S., Silicon Nitride Ceramics. *Mater. Sci. Forum* **2009**, *606*, 27-41.
48. Thompson, D. P., The Crystal Chemistry of Nitrogen Ceramics. *Mater. Sci. Forum* **1989**, *47*, 21-42.
49. Dressler, W.; Kleebe, H.-J.; Hoffmann, M. J.; Rühle, M.; Petzow, G., Model Experiments Concerning Abnormal Grain Growth in Silicon Nitride. *J. Eur. Ceram. Soc.* **1996**, *16*, 3-14.
50. Stuart Hampshire, M. J. P., Grain boundary glasses in silicon nitride: A review of chemistry, properties and crystallisation. *J. Eur. Ceram. Soc.* **2012**, *32*, 1925-32.
51. Toropov, N. A.; Bondar, I. A.; Galadgov, F. Y.; Nikogosyan, K. S.; Vinogradova, N. V., Phase Equilibria in the Yttrium Oxide-Alumina System. *Phys. Chem.* **1964**, 1158-64.
52. Kolitsch, U.; Seifert, H. J.; Ludwig, T.; Aldinger, F., Phase equilibria and crystal chemistry in the Y<sub>2</sub>O<sub>3</sub>-Al<sub>2</sub>O<sub>3</sub>-SiO<sub>2</sub> system. *J. Mater. Res.* **1999**, *14* (2), 447-55.
53. Kolitsch, U.; Seifert, H. J.; Aldinger, F., Phase Relationships in the Systems RE<sub>2</sub>O<sub>3</sub>-Al<sub>2</sub>O<sub>3</sub>-SiO<sub>2</sub> (RE = Rare Earth Element, Y, and Sc). *J. Phase Equilib.* **1998**, *19* (5), 426-33.
54. Aramaki, S.; Roy, R., Revised Phase Diagram for the System Al<sub>2</sub>O<sub>3</sub>-SiO<sub>2</sub>. *J. Am. Ceram. Soc.* **1961**, *45* (5), 229-42.
55. Drummond III, C. H.; Lee, W. E., Crystallization and Characterization of Y<sub>2</sub>O<sub>3</sub>-SiO<sub>2</sub> Glasses. *Ceram. Eng. Sci. Proc.* **1988**, *9* (9-10), 1343-54.
56. Fabrichnaya, O.; Pavlyuchkov, D.; Neher, R.; Herrmann, M.; Seifert, H. J., Liquid phase formation in the system Al<sub>2</sub>O<sub>3</sub>-Y<sub>2</sub>O<sub>3</sub>-AlN: Part II.Thermodynamic assessment. *J. Eur. Ceram. Soc.* **2013**, *33*, 2457-63.
57. Cozzan, C.; Griffith, K. J.; Laurita, G.; Hu, J. G.; Grey, C. P.; Seshadri, R., Structural Evolution and Atom Clustering in  $\beta$ -SiAlON:  $\beta$ -Si<sub>6-z</sub>Al<sub>z</sub>O<sub>2</sub>N<sub>8-z</sub>. *Inorg. Chem.* **2017**, *56*, 2153-58.
58. Trigg, M. B.; Jack, K. H., The fabrication of O'-sialon ceramics by pressureless sintering. *J. Mater. Sci.* **1988**, *23*, 481-87.
59. Fang, C. M.; Metselaar, R., Site preferences in  $\beta$ -sialon from first-principles calculations. *J. Mater. Chem.* **2003**, *13*, 335-37.

60. Yeh, H. C.; Sanders, W. A.; Fiyalko, J. L. *Silicon Nitride-Aluminum Oxide Solid Solution (SiAlON) Formation and Densification by Pressure Sintering*; National Aeronautics and Space Administration: Cleveland, OH, 1975.
61. Gauckler, L. J.; Lukas, H. L.; Petzow, G., Contribution to the Phase Diagram Si<sub>3</sub>N<sub>4</sub>-AlN-Al<sub>2</sub>O<sub>3</sub>-SiO<sub>2</sub>. *J. Am. Ceram. Soc.* **1975**, 58 (7-8), 346-47.
62. Bowen, L. J.; Weston, R. J.; Carruthers, T. G.; Brook, R. J., Hot-pressing and the  $\alpha$ - $\beta$  phase transformation in silicon nitride. *J. Mater. Sci.* **1978**, 13, 341-50.
63. Chen, I.-W.; Hwang, S.-L., Superplastic SiAlON-A Bird's Eye View of Silicon Nitride Ceramics. *Mat. Res. Soc. Symp.* **1993**, 287, 209-22.
64. Drew, P.; Lewis, M. H., The microstructures of silicon nitride ceramics during hot-pressing transformations. *J. Mater. Sci.* **1974**, 9, 261-69.
65. Bergman, B.; Ekström, T.; Micski, A., The Si-Al-O-N System at Temperatures of 1700-1750°C. *J. Eur. Ceram. Soc.* **1991**, 8, 141-51.
66. Sun, W.-Y.; Tien, T.-Y.; Yen, T.-S., Subsolidus Phase Relationships in Part of the System Si, Al, Y/N, O: The System Si<sub>3</sub>N<sub>4</sub>-AIN-YN-Al<sub>2</sub>O<sub>3</sub>-Y<sub>2</sub>O<sub>3</sub>. *J. Am. Ceram. Soc.* **1991**, 74 (11), 2753-58.
67. Izhevskiy, V. A.; Genova, L. A.; Bressiani, J. C.; Aldinger, F., Progress in SiAlON ceramics. *J. Eur. Ceram. Soc.* **2000**, 20, 2275-95.
68. Huang, Z.-K.; Chen, I.-W., Rare Earth Melilite Solid Solution and Its Phase Relations with Neighboring Phases. *J. Am. Ceram. Soc.* **1996**, 79 (8), 2091-97.
69. Ekström, T.; Käll, P. O.; Nygren, M.; Olsson, P. O., Dense single-phase  $\beta$ -sialon ceramics by glass-encapsulated hot isostatic pressing. *J. Mater. Sci.* **1989**, 24, 1853-61.
70. Thompson, D. P.; Korgul, P.; Hendry, A., The Structural Characterisation of Sialon Polytypoids. In *Progress in Nitrogen Ceramics*, Riley, F. L., Ed. Martinus Nijhoff Publishers: Boston/The Hague/Dordrecht/Lancaster, 1983; Vol. 61-74.
71. Ijevskii, V. A.; Kolitsch, U.; Seifert, H. J.; Wiedmann, I.; Aldinger, F., Aluminum-Containing Ytterbium Nitrogen Woehlerite Solid Solutions. Synthesis, Structure, and some Properties. *J. Eur. Ceram. Soc.* **1998**, 18, 543-52.
72. Chee, K. S.; Cheng, Y.-B.; Smith, M. E., The Solubility of Aluminium in Rare Earth Nitrogen Melilite Phases. *J. Eur. Ceram. Soc.* **1995**, 15, 1213-20.
73. Cheng, Y.-B.; Thompson, D. P., Aluminum-Containing Nitrogen Melilite Phases. *J. Am. Ceram. Soc.* **1994**, 77 (1), 143-48.
74. Shannon, R. D., Revised effective ionic radii and systematic studies of interatomic distances in halides and chalcogenides. *Acta Cryst. A* **1976**, 32, 751-67.
75. Wang, C.-M.; Pan, X.; Rühle, M.; Riley, F. L.; Mitomo, M., Review: Silicon nitride crystal structure and observations of lattice defects. *J. Mater. Sci.* **1996**, 31, 5281-98.
76. Chee, K. S.; Cheng, Y.-B.; Smith, M. E., NMR Investigation of the Structure of Aluminum-Containing Nitrogen Melilite (M'<sub>ss</sub>). *Chem. Mater.* **1995**, 7, 982-88.
77. P. L. Wang; Tu, H. Y.; Yan, W. Y. S. S.; Nygren, M.; Ekström, T., Study on the Solid Solubility of Al in the Melilite Systems R<sub>2</sub>Si<sub>3-x</sub>Al<sub>x</sub>O<sub>3+x</sub>N<sub>4-x</sub> with R = Nd, Sm, Gd, Dy and Y. *J. Eur. Ceram. Soc.* **1995**, 15, 689-95.
78. Thompson, D. P. In *New Grain-Boundary Phases for Nitrogen Ceramics*, Mat. Res. Soc. Symp. Proc., Boston, MA, Chen, I.-W.; Becher, P. F.; Mitomo, M.; Petzow, G.; Yen, T.-S., Eds. Materials Research Society: Boston, MA, 1993; pp 79-92.
79. Kusunose, T.; Sekino, T.; Mogan, P. E. D.; Nihara, K., Effect of Oxynitride Grain Boundary Phase on Toughening of Silicon Nitride Ceramics. *Key Eng. Mater.* **2006**, 317-318, 649-652.
80. Lewis, M. H., Sialons and Silion Nitrides ; Microstructural Design and Performance. *Mat. Res. Soc. Symp.* **1993**, 287, 159-172.
81. Gajum, N. R. Rare-Earth Doped ( $\alpha$ / $\beta'$ ) SiAlON Ceramics. University of Warwick, 2001.

82. Huang, Z.-K.; Liu, S.-Y.; Rosenflanz, A.; Chen, I.-W., SiAlON Composites Containing Rare-Earth Melilite and Neighboring Phases. *J. Am. Ceram. Soc.* **1996**, *79* (8), 2081-90.
83. Baldus, H.-P.; Jansen, M., Novel High-Performance Ceramics—Amorphous Inorganic Networks from Molecular Precursors. *Angew. Chem. Int. Ed.* **1997**, *36* (4), 328-343.
84. Colombo, P.; Mera, G.; Riedel, R.; Soraru, G. D., Polymer-Derived Ceramics: 40 Years of Research and Innovation in Advanced Ceramics. *J. Am. Ceram. Soc.* **2010**, *93* (7), 1805-37.
85. Bernardo, E.; Fiocco, L.; Parcianello, G.; Storti, E.; Colombo, P., Advanced Ceramics from Preceramic Polymers Modified at the Nano-Scale: A Review. *Materials* **2014**, *7* (3), 1927-1956.
86. Schönfelder, H.; Aldinger, F.; Riedel, R., Silicon carbonitrides - A novel class of materials. *J. Phys., IV* **1993**, *3*, 1293-98.
87. Haug, R.; Weinmann, M.; Bill, J.; Aldinger, F., Plastic Forming of Preceramic Polymers. *J. Eur. Ceram. Soc.* **1998**, *19*, 1-6.
88. Kroke, E.; Li, Y.-L.; Konetschny, C.; Lecomte, E.; Fasel, C.; Riedel, R., Silazane derived ceramics and related materials. *Mater. Sci. Eng. R Rep.* **2000**, *26*, 97-199.
89. Livage, J., Sol-gel processes. *Curr. Opin. Solid. State Mater. Sci.* **1997**, *2*, 132-8.
90. Rahman, I. A.; Padavattan, V., Synthesis of Silica Nanoparticles by Sol-Gel: Size-Dependent Properties, Surface Modification, and Applications in Silica-Polymer Nanocomposites—A Review. *J. Nanomater.* **2012**, *2012*, 1-15.
91. Cihlář, J., Hydrolysis and polycondensation of ethyl silicates. 1. Effect of pH and catalyst on the hydrolysis and polycondensation of tetraethoxysilane (TEOS). *Colloid Surf. A-Physiochem. Eng. Asp.* **1992**, *70*, 239-51.
92. Ji, L.; Lin, J.; Tan, K. L.; Zeng, H. C., Synthesis of High-Surface-Area Alumina Using Aluminum Tri-sec-butoxide-2,4-Pentanedione-2-Propanol-Nitric Acid Precursors. *Chem. Mater.* **2000**, *12*, 931-39.
93. Riedel, R.; Kienzle, A.; Dressler, W.; Ruwisch, L.; Bill, J.; Aldinger, F., A siliconboron carbonitride ceramic stable to 2,000°C. *Nature* **1996**, *382* (6594), 796-798.
94. Riedel, R.; Mera, G.; Hauser, R.; Klonczynski, A., Silicon-Based Polymer-Derived Ceramics: Synthesis Properties and Applications-A Review. *J. Ceram. Soc. Jpn.* **2006**, *114* (1330), 425-444.
95. Störmer, H.; Kleebe, H. -J.; Ziegler, G., Metastable SiCN glass matrices studied by energy-filtered electron diffraction pattern analysis. *J. Non. Cryst. Solids* **2007**, *352*, 2867-77.
96. Jansen, M., Highly stable ceramics through single source precursors. *Solid State Ion.* **1997**, *101-103*, 1-7.
97. Zern, A.; Mayer, J.; Janakiraman, N.; Weinmann, M.; Bill, J.; Rühle, M., Quantitative EFTEM study of precursor-derived Si–B–C–N ceramics. *J. Eur. Ceram. Soc.* **2002**, *22*, 1621-9.
98. Tavakoli, A. H.; Gerstel, P.; Golczewski, J. A.; Bill, J., Kinetic effect of boron on the crystallization of Si<sub>3</sub>N<sub>4</sub> in Si–B–C–N polymer-derived ceramics. *J. Mater. Res.* **2010**, *26* (4), 600-608.
99. Widgeon, S.; Mera, G.; Gao, Y.; Stoyanov, E.; Sen, S.; Navrotsky, A.; Riedel, R., Nanostructure and Energetics of Carbon-Rich SiCN Ceramics Derived from Polysilylcarbodiimides: Role of the Nanodomain Interfaces. *Chem. Mater.* **2012**, *24*, 1181-91.
100. Widgeon, S.; Mera, G.; Gao, Y.; Sen, S.; Navrotsky, A.; Riedel, R., Effect of Precursor on Speciation and Nanostructure of SiBCN Polymer-Derived Ceramics. *J. Am. Ceram. Soc.* **2013**, *96* (5), 1651-9.

101. Tavakoli, A. H.; Gerstel, P.; Golczewski, J. A.; Bill, J., Effect of boron on the crystallization of amorphous Si–(B–)C–N polymer-derived ceramics. *J. Non. Cryst. Solids* **2009**, *355* (2381-2389), 2381.
102. Iwamoto, Y.; Völger, W.; Kroke, E.; Riedel, R.; Saitou, T.; Matsunaga, K., Crystallization Behavior of Amorphous Silicon Carbonitride Ceramics Derived from Organometallic Precursors. *J. Am. Ceram. Soc.* **2001**, *84* (10), 2170-78.
103. Alkoy, S.; Toy, C.; Gönül, T.; Tekin, A., Crystallization Behavior and Characterization of Turbostratic Boron Nitride. *J. Eur. Ceram. Soc.* **1997**, *17*, 1415-22.
104. Toyofuku, N.; Yamasaki, N.; Kodera, Y.; Ohyanagi, M.; Munir, Z. A., Turbostratic boron nitride consolidated by SPS. *J. Ceram. Soc. Jpn.* **2009**, *117* (2), 189-93.
105. Weinmann, M.; Schuhmacher, J.; Kummer, H.; Prinz, S.; Peng, J.; Seifert, H. J.; Christ, M.; Müller, K.; Bill, J.; Aldinger, F., Synthesis and Thermal Behavior of Novel Si-B-C-N Ceramic Precursors. *Chem. Mater.* **2000**, *2000* (I2), 623-32.
106. Matsunaga, K.; Iwamoto, Y., Molecular Dynamics Study of Atomic Structure and Diffusion Behavior in Amorphous Silicon Nitride Containing Boron. *J. Am. Ceram. Soc.* **2001**, *84* (10), 2213-19.
107. Mera, G.; Gallei, M.; Bernard, S.; Ionescu, E., Ceramic Nanocomposites from Tailor-Made Preceramic Polymers. *Nanomaterials* **2015**, *(5)*, 468-540.
108. Wolf, S. F. Barrier Layers and Metal Fill for Back End of Line Processing. University of California San Diego, San Diego, CA, 2019.
109. Ahmed, M.; Li, Y.; Chen, W.; Li, E.-P., Diffusion Barrier Prediction of Graphene and Boron Nitride for Copper Interconnects by Deep Learning. *IEEE Access* **2020**, *8*, 210542-9.
110. Amato, I.; Martorana, D.; Silengo, B., Some Considerations on the Kinetics of Hot-pressing Alpha-Silicon Nitride Powder. *Mater. Sci. Eng.* **1977**, *28* (2), 215-20.
111. Ting, C.-J.; Lu, H.-Y., Hot-Pressing of Magnesium Aluminate Spinel- I. Kinetics and Densification Mechanisms. *Acta. Mater.* **1999**, *47* (3), 817-30.
112. Kusunose, T.; Sekino, T.; Choa, Y. H.; Niihara, K., Fabrication and Microstructure of Silicon Nitride/Boron Nitride Nanocomposites. *J. Am. Ceram. Soc.* **2002**, *85* (11), 2648-88.
113. Li, Y.; Yu, H.; Shi, Z.; Jin, H.; Qiao, G.; Jin, Z., Synthesis of  $\beta$ -SiAlON/h-BN nanocomposite by a precursor infiltration and pyrolysis (PIP) route. *Mater. Lett.* **2015**, *139*, 303-6.
114. Kusunose, T.; Sekino, T.; Choa, Y. H.; Niihara, K., Fabrication and Microstructure of Silicon Nitride/Boron Nitride Nanocomposites. *J. Am. Ceram. Soc.* **2002**, *85* (11), 2678-88.
115. Lee, B.; Lee, D.; Lee, J. H.; Ryu, H. J.; Hong, S. H., Enhancement of toughness and wear resistance in boron nitride nanoplatelet (BNNP) reinforced  $\text{Si}_3\text{N}_4$  nanocomposites. *Nature* **2016**, *6*, 1-12.
116. ASTM International, *Standard Practice for Fractography and Characterization of Fracture Origins in Advanced Ceramics*. ASTM C1322-15; West Conshohocken, PA, 2015.
117. Kokcharov, I. File:HoleForceLines.gif.  
<https://commons.wikimedia.org/wiki/File:HoleForceLines.gif> (accessed Jauary 19, 2022).
118. Hibbeler, R. C., *Mechanics of Materials*. 10 ed.; PearsonEducation, Inc.: Hoboken, NJ, 2017.
119. Inglis, C. E., Stresses in a plate due to the presence of cracks and sharp corners. *Trans. Inst. Naval Archit.* **1913**, *55*, 219-241.
120. Zok, F., On weakest link theory and Weibull statistics. *J. Am. Ceram. Soc.* **2017**, *100* (4), 1265-1268.

121. Mecholsky, J. J.; Rice, R. W.; Freeman, S. W., Prediction of Fracture Energy and Flaw Size in Glasses from Measurements of Mirror Size. *J. Amer. Ceram. Soc.* **1974**, 57 (10), 440-43.
122. Mecholsky, J. J.; Freimam, S. W.; Rice, R. W., Fracture surface analysis of ceramics. *J. Mater Sci.* **1976**, 11 (7), 1310-1319.
123. Simpson, L. A.; Hsu, T. R.; Merrett, G., The Application of the Single-Edge Notched Beam to Fracture Toughness Testing of Ceramics. *ASTM Int.* **1974**, 2 (6).
124. Nindhia, T. G. T., Comparison of fracture toughness testing by the single edge v-notch beam and the surface crack in flexure method on silicon nitride. *IOP Conf. Ser.: Mater. Sci. Eng.* **2020**, 852.
125. Quinn, G. D.; Swab, J. J., Fracture toughness of glasses as measured by the SCF and SEPB methods. *J. Eur. Ceram. Soc.* **2017**, 37, 4243-57.
126. Quinn, G. D. In *Fracture toughness of ceramics by the Vickers indentation crack length method: A critical review*, Ceramic Engineering and Science, Cocoa Beach, FL, George D. Quinn: Cocoa Beach, FL, 2006.
127. Niihara, K.; Morena, R.; Hasselman, D. P. H., Evaluation of  $K_{IC}$  of brittle solids by the indentation method with low crack-to-indent ratios. *J. Mater. Sci. Lett.* **1982**, 1, 13-16.
128. Ekström, T., Sialon Ceramics Sintered with Yttria and Rare Earth Oxides. *Mat. Res. Soc. Symp. Proc.* **1992**, 287, 121-32.
129. Ivicheva, S. N.; Ovsyannikov, N. A.; Lysenkov, A. S.; Klimashin, A. A.; Kargin, Y. F., Sol-Gel Synthesis of Oxonitridoaluminosilicates (SiAlON). *Russ. J. Inorg.* **2020**, 65 (12), 1820-30.
130. Xu, L.; Liang, H.-W.; Yang, Y.; Yu, S.-H., Stability and Reactivity: Positive and Negative Aspects for Nanoparticle Processing. *Chem. Rev.* **2018**, 118, 3209-50.
131. Nenoff, T. M.; Jacobs, B. W.; Robinson, D. B.; Provencio, P. P.; Huang, J.; Ferreira, S.; Hanson, D. J., Synthesis and Low Temperature In Situ Sintering of Uranium Oxide Nanoparticles. *Chem. Mater.* **2011**, 23, 5185-90.
132. Brooks, H. S. Sol-gel coating of silicon nitride powder, SiAlON formation, and selected properties. University of Pittsburgh, Pittsburgh, PA, 1992.
133. Tripp, W. C.; Graham, H. C., Oxidation of  $\text{Si}_3\text{N}_4$  in the Range 1300° to 1500°C. *J. Am. Ceram. Soc.* **1976**, 59 (9-10), 399-403.
134. Lin, C.-Y.; Lu, F.-H., Oxidation behavior of AlN films at high temperature under controlled atmosphere. *J. Eur. Ceram. Soc.* **2007**, 28, 691-98.
135. ASTM International. *Standard Test Methods for Apparent Porosity, Liquid Absorption, Apparent Specific Gravity, and Bulk Density of Refractory Shapes by Vacuum Pressure.*; ASTM C830-00(2016); West Conshohocken, PA, 2016.
136. Lord, J. D.; Morrell, R. *Elastic Modulus Measurement*; National Physical Laboratory: Middlesex, 2006.
137. Shulman, G. P.; Trusty, M.; Vickers, J. H., Thermal Decomposition of Aluminum Alkoxides. *J. Org. Chem.* **1963**, 28 (4), 907-10.
138. Inoue, M.; Kominami, H.; Inui, T., Thermal Transformation of  $\gamma$ -Alumina Formed by Thermal Decomposition of Aluminum Alkoxide in Organic Media. *J. Amer. Ceram. Soc.* **1992**, 75 (9), 2597-98.
139. Haanappel, V. A. C.; Corbach, H. D. v.; Fransen, T.; Gellings, P. J., The pyrolytic decomposition of aluminium-tri-sec-butoxide during chemical vapour deposition of thin alumina films. *Thermochim. Acta* **1994**, 240, 67-77.
140. Tatsumi, K.; Mizoguchi, T.; Yoshioka, S.; Yamamoto, T.; Suga, T.; Sekine, T.; Tanaka, I., Distribution of solute atoms in  $\beta$ - and spinel  $\text{Si}_{6-z}\text{Al}_z\text{O}_z\text{N}_{8-z}$  by Al K-edge x-ray absorption near-edge structure. *Phys. Rev. B* **2005**, 71 (3), 1-4.

141. Tavakoli, A. H.; Gerstel, P.; Golczewski, J. A.; Bill, J., Quantitative X-ray Diffraction Analysis and Modeling of the Crystallization Process in Amorphous Si–B–C–N Polymer-Derived Ceramics. *J. Am. Ceram. Soc.* **2010**, 93 (5), 1470-1478.
142. McGarry, K. In *On the Thermal Decomposition Mechanisms of a Si-Based Polymer-Derived Ceramic*, International Conference on Advanced Ceramics and Composites, Daytona Beach, Fl, USA, Daytona Beach, Fl, USA, 2020.
143. ASTM International. *Standard Test Method for Flexural Strength of Advanced Ceramics at Ambient Temperature*; ASTM C1161-13; West Conshohocken, PA, 2018.
144. ASTM International. *Standard Test Methods for Determining Average Grain Size*; ASTM E112-13; West Conshohocken, PA, 2013.
145. Chinn, R. E., *Ceramography: Preparation and Analysis of Ceramic Microstructures*. ASM International: Materials Park, OH, USA, 2002.
146. Gorbachev, R. V.; Riaz, I.; Nair, R. R.; Jalil, R.; Britnell, L.; Belle, B. D.; Hill, E. W.; Novoselov, K. S.; Watanabe, K.; Taniguchi, T.; Geim, A. K.; Blake, P., Hunting for Monolayer Boron Nitride: Optical and Raman Signatures. *Small* **2011**, 7 (4), 465-68.
147. Saha, S.; Muthu, D. V. S.; Goldberg, D.; Tang, C.; Zhi, C.; Bando, Y.; Sood, A. K., Comparative high pressure Raman study of boron nitride nanotubes and hexagonal boron nitride. *Chem. Phys. Lett.* **2006**, 421, 86-90.
148. Konijnendijk, W. L.; Stevels, J. M., The Structure of Borate Glasses Studied by Raman Scattering. *J. Non. Cryst. Solids* **1975**, 18, 307-331.
149. Takase, A.; Tani, E., Raman spectroscopic study of  $\beta$ -sialons in the system  $\text{Si}_3\text{N}_4\text{-Al}_2\text{O}_3\text{-AlN}$ . *J. Mater. Sci. Let.* **1984**, 3, 1058-60.
150. Kuzuba, T.; Kijima, K.; Bando, Y., Raman-active modes of alpha silicon nitride. *J. Chem. Phys.* **1978**, 69 (1).
151. Gervais, C.; Framery, E.; Duriez, C.; Maquet, J.; Vaultier, M.; Babonneau, F.,  $^{11}\text{B}$  and  $^{15}\text{N}$  solid state NMR investigation of a boron nitride preceramic polymer prepared by ammonolysis of borazine. *J. Eur. Ceram. Soc.* **2005**, 25, 129-35.
152. Gervais, C.; Maquet, J.; Babonneau, F.; Duriez, C.; Framery, E.; Vaultier, M.; Florian, P.; Massiot, D., Chemically Derived BN Ceramics: Extensive  $^{11}\text{B}$  and  $^{15}\text{N}$  Solid-State NMR Study of a Preceramic Polyborazilene. *Chem. Mater.* **2001**, 13, 1700-07.
153. Gervais, C.; Babonneau, F.; Ruwisch, L.; Hauser, R.; Riedel, R., Solid-state NMR investigations of the polymer route to SiBCN ceramics. *Can. J. Chem.* **2003**, 81, 1359-69.
154. Schuhmacher, J.; Berger, F.; Weinmann, M.; Bill, J.; Aldinger, F.; Müller, K., Solid-state and FT IR studies of the preparation of Si-B-C-N ceramics from boron-modified polysilazanes. *Appl. Organomet. Chem.* **2001**, 15, 809-19.
155. Du, L.-S.; Stebbins, J. F., Nature of Silicon-Boron Mixing in Sodium Borosilicate Glasses: A High-Resolution  $^{11}\text{B}$  and  $^{17}\text{O}$  NMR Study. *J. Phys. Chem. B.* **2003**, 107, 10063-76.
156. Coupling Constants Identify Coupled Protons.  
<https://chem.libretexts.org/@go/page/13944> (accessed Jan 13, 2022).
157. END, B. B., AVANCE Beginners Guide User Guide Version 006. Corporation, B., Ed. 2014.
158. Gueli, D. C.; Hughes, R. D. Measurement of elastic modulus : acoustic emission versus direct strain measurements. Alfred University, Alfred, NY, 2016.
159. Kingery, W. D., Densification during Sintering in the Presence of a Liquid Phase. I. Theory. *J. Appl. Phys.* **1959**, 30, 301-06.
160. Kingery, W. D.; Narasimhan, M. D., Densification during Sintering in the Presence of a Liquid Phase. II. Experimental. *J. Appl. Phys.* **1959**, 30, 307-10.
161. Bowen, L. J.; Weston, R. J.; Carruthers, T. G.; Brook, R. J., Mechanisms of Densification During the Pressure Sintering of Alpha-Silicon Nitride. *Ceramurgica Int.* **1976**, 2 (4), 173-76.

162. Roylance, D. 3.11 Mechanics of Materials. <https://ocw.mit.edu>.
163. Timoshenko, S., *Strength of Materials Part I: Elementary Theory and Problems*. 2 ed.; D. Van Nostrand Company: New York, 1940.

## VIII.APPENDICES

### A. Rietveld Refinement Results

The following parameters were established for all Rietveld refinements in this work. The order in which they are presented is the same as the order in which they were refined. Note that many of these parameters are specific to the Bruker D2 Phaser Benchtop diffractometer used in this work.

1. Background: 5<sup>th</sup> order Chebychev (refine)
2. Instrument Parameters
  - a. Goniometer radii: 141 mm
  - b. Linear PSD 
    - 2θ angular range = 4° (fix)
    - Fixed divergence slit (FDS) angle = 0.8° (fix)
    - Beam spill = 20 mm (fix)
  - c. Tube tails 
    - Source width = 0.04 mm (fix)
    - Z1 (refine)
    - Z2 (refine)
    - Fraction (refine)
  - d. Sample displacement  (refine)
  - e. Lorentz polarization (LP) factor  (fix)
3. Phase Refinement (for each CIF uploaded in sequence)
  - a. Peak type: PV\_Mod
  - b. Scale  (refine)
  - c. Lattice Parameters  (refine)
  - d. Preferred orientation: (2 1 0)  (1 0 0) 
    - Refine one at a time for all atoms with non-special positions, e.g.  
0.25)
  - e. Atomic positions
- f. Atomic displacement (B) = 7/10 Å<sup>2</sup> for all atoms

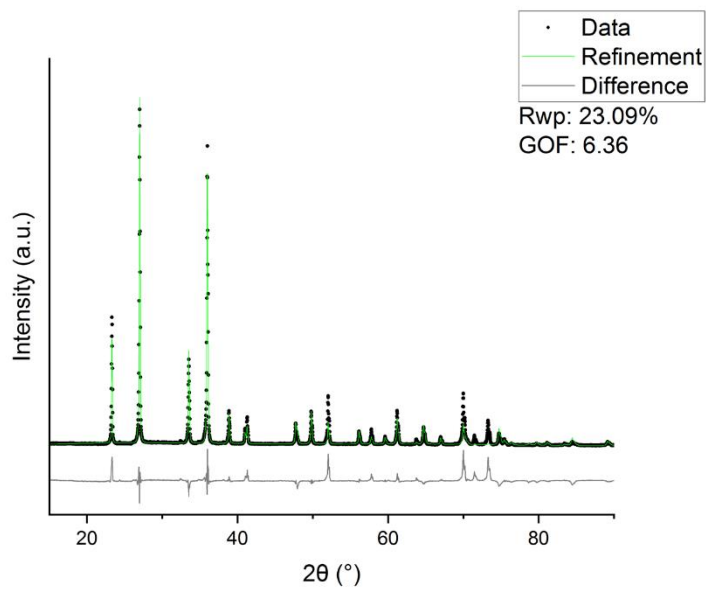


Figure 62. Rietveld refinement result for 4YAl<sub>2</sub>O<sub>3</sub> sintered for 60 minutes.

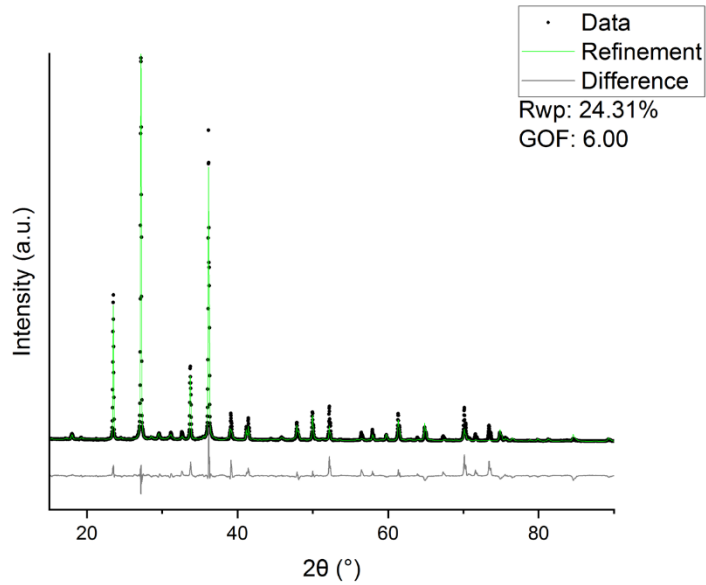


Figure 63. Rietveld refinement result for 4YAl<sub>2</sub>O<sub>3</sub> sintered for 10 minutes.

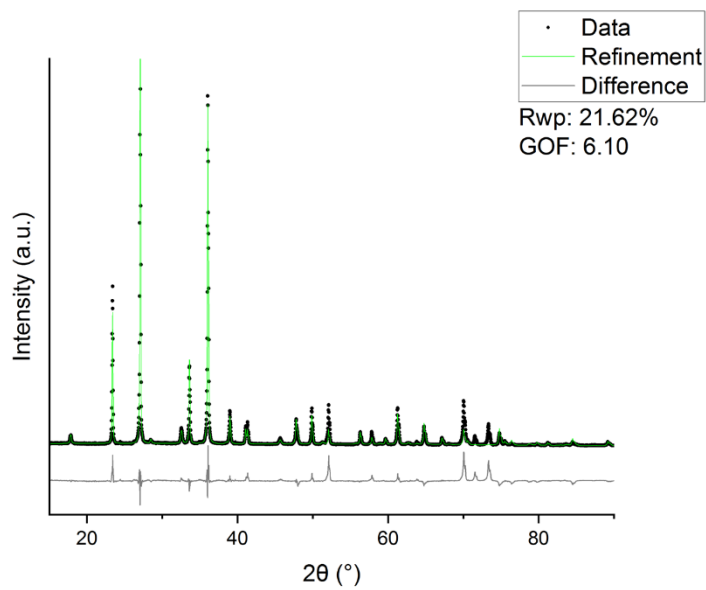


Figure 64. Rietveld refinement result for  $\text{4YAl}_2\text{O}_3$  sintered for 1 minute.

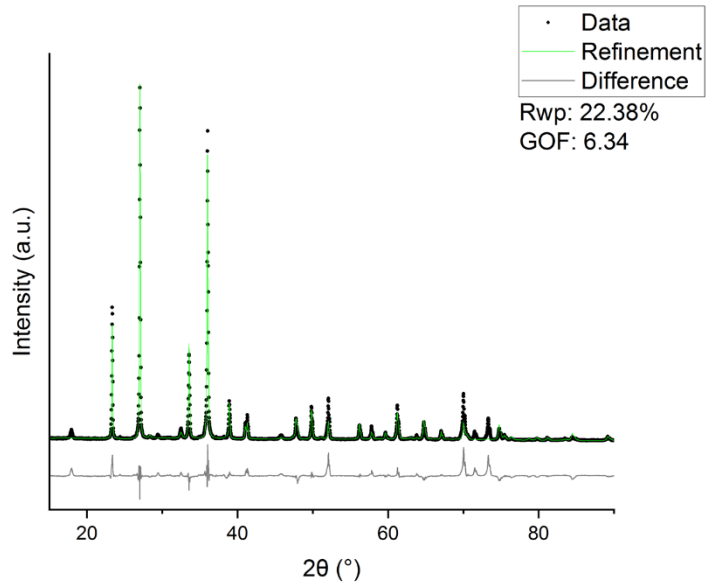


Figure 65. Rietveld refinement result for  $\text{4YASB}$  sintered for 60 minutes.

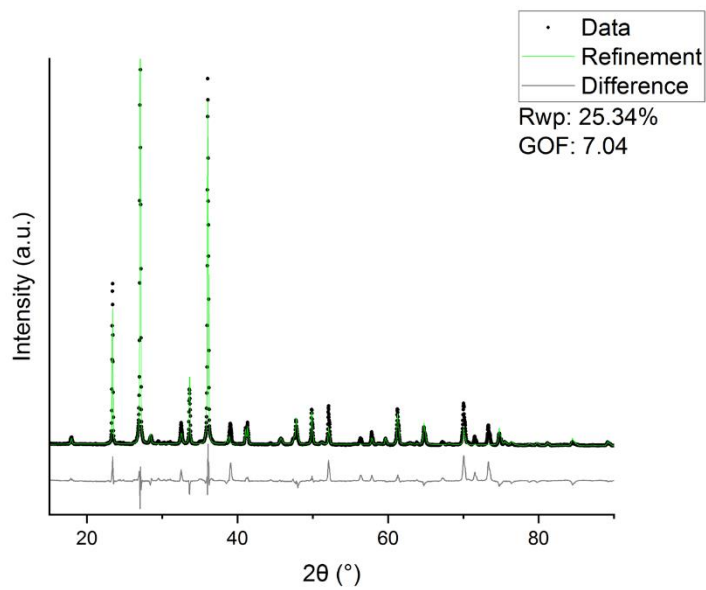


Figure 66. Rietveld refinement result for 4YASB sintered for 3 minutes.

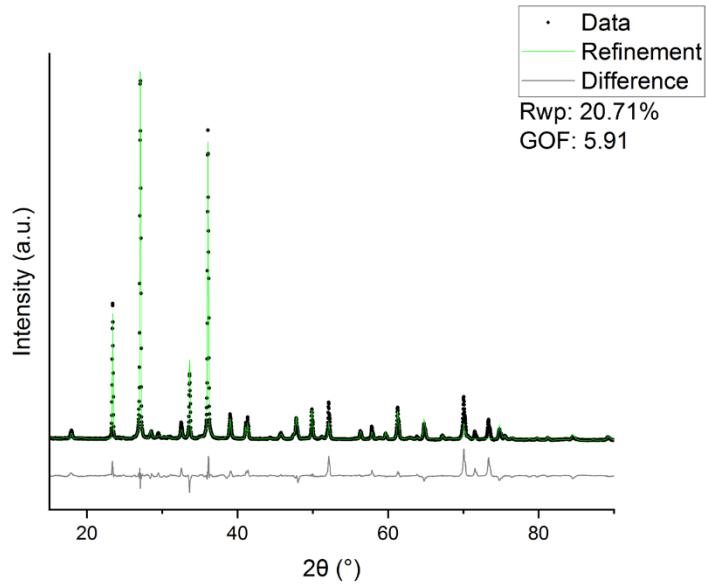


Figure 67. Rietveld refinement result for 4YASB sintered for 1 minute.

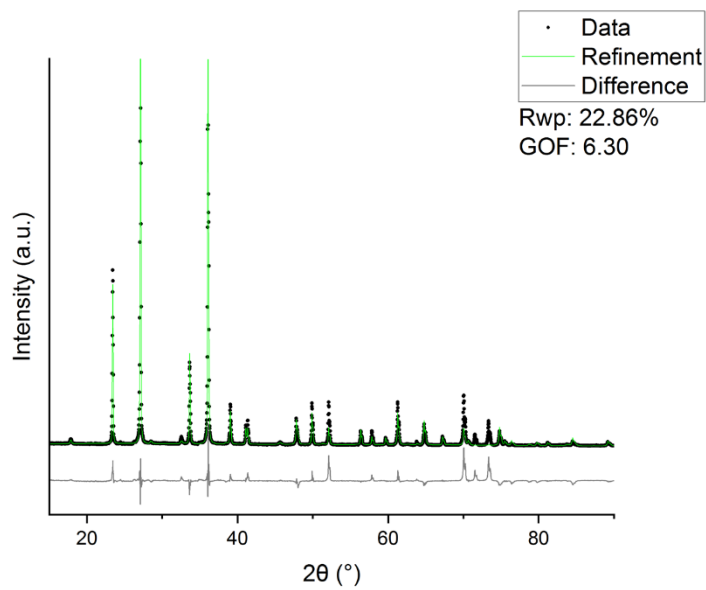


Figure 68. Rietveld refinement result for  $\text{2YAl}_2\text{O}_3$  sintered for 60 minutes.

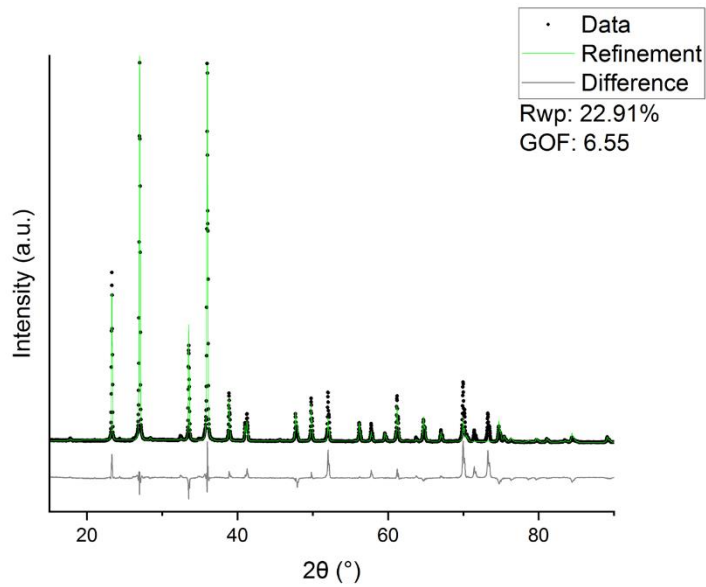


Figure 69. Rietveld refinement result for  $\text{2YASB}$  sintered for 60 minutes.

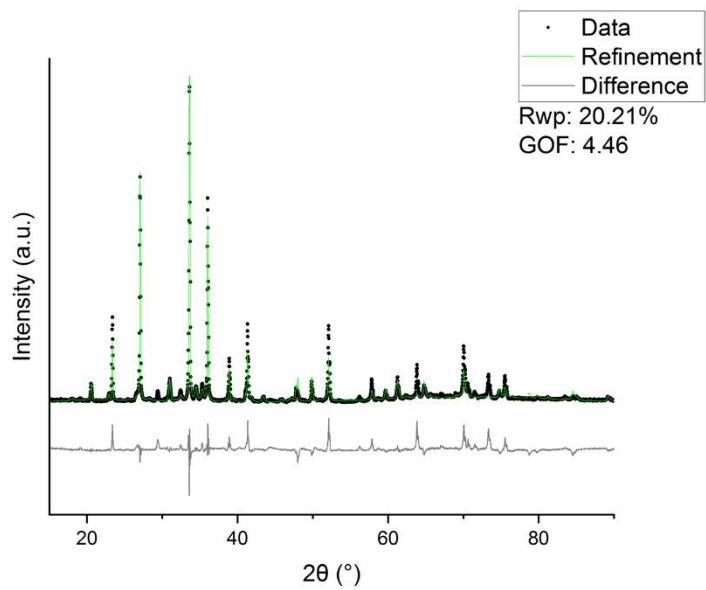


Figure 70. Rietveld refinement result for SiAlON B0.

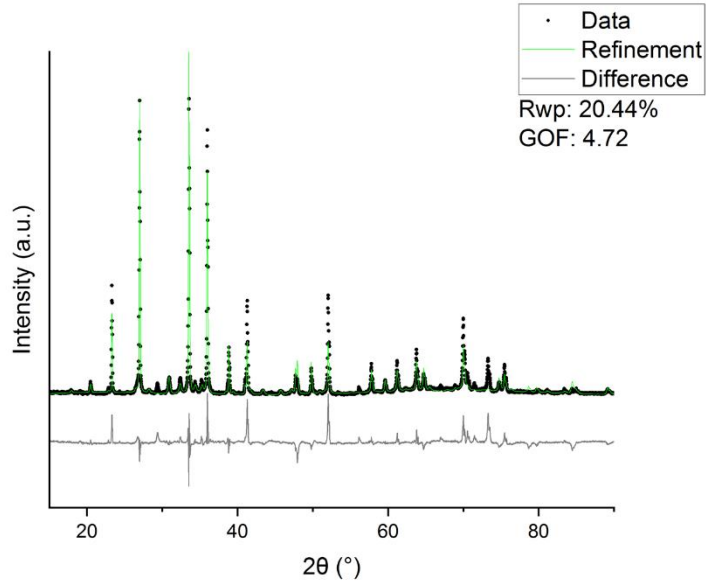


Figure 71. Rietveld refinement result for SiAlON B1.

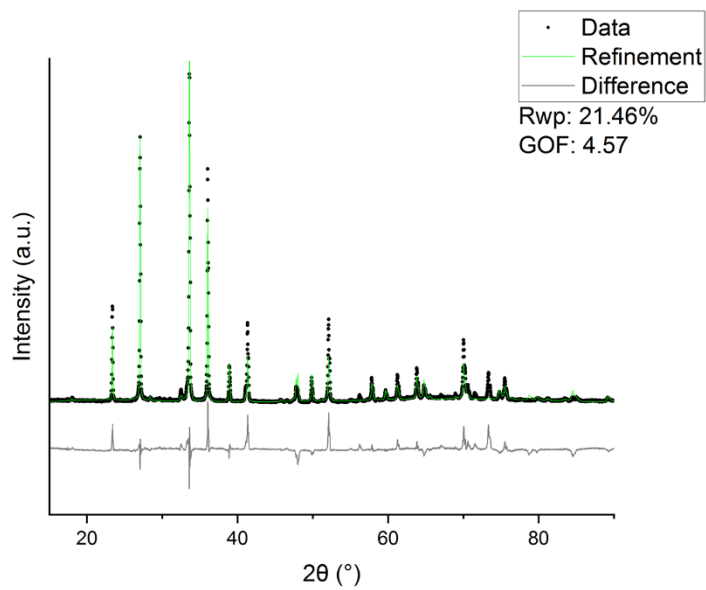


Figure 72. Rietveld refinement result for SiAlON B2.

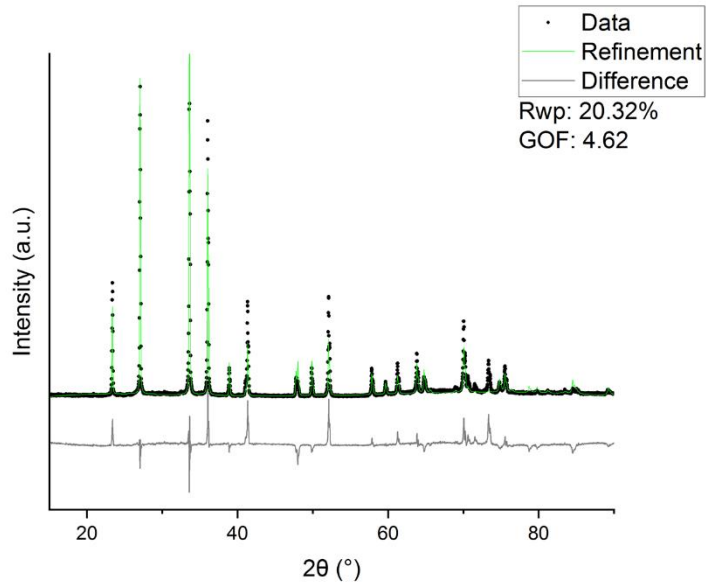
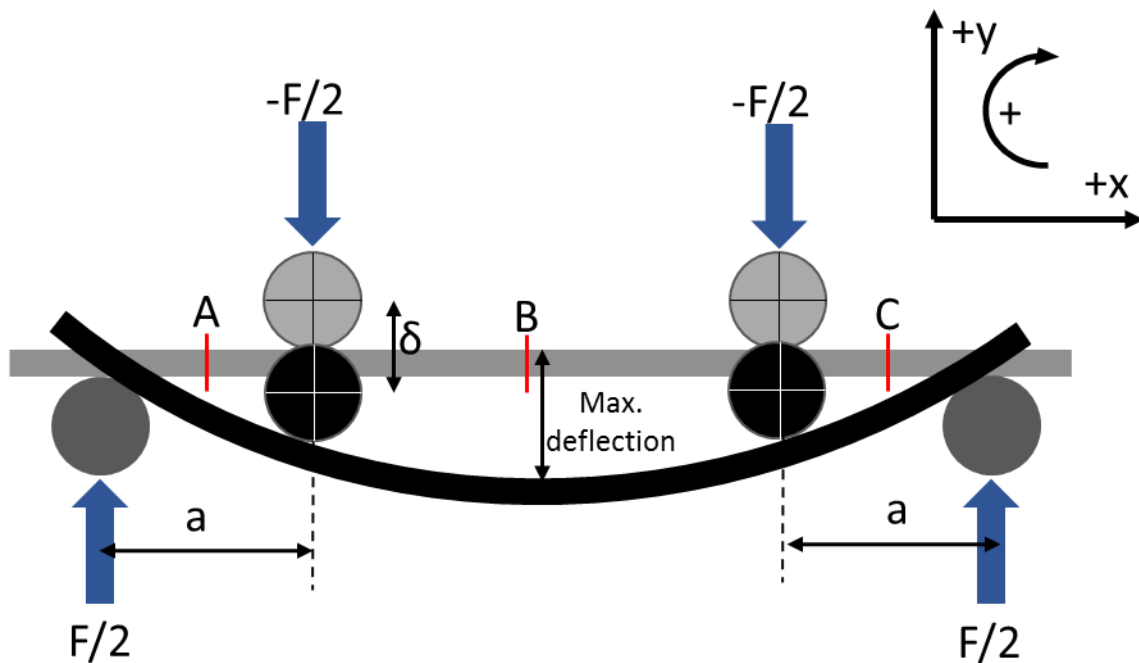


Figure 73. Rietveld refinement result for SiAlON B3.

## B. Beam Theory Approach to Stress and Strain

The following derivations were informed by open course materials provided by Massachusetts Institute of Technology<sup>162</sup>, S. Timoshenko's Strength of Materials text<sup>163</sup>, and R. C. Hibbeler's Mechanics of Materials text.<sup>118</sup>

Beam theory can be applied to assess the stresses and strains developed in a flexure specimen at every stage of an experiment by converting raw data of load and displacement to stress and strain. A schematic illustrating a four point ¼-pt flexure experiment is presented in Figure 74, where  $F$  is the applied force. Note that the deflection of the bar is greatly exaggerated relative to typical deflections of ceramics, and that the deflection measured by the crosshead of the instrument,  $\delta$ , is actually less than the maximum deflection experienced by the beam. For this analysis, the rightward and upward directions will be considered to be the positive x and y directions, respectively, and clockwise will likewise be considered positive.



**Figure 74.** Schematic of a beam in four point ¼-pt flexure.  $\delta$  is the travel measured by the instrument, but the maximum deflection occurring at the center of the beam is greater than this distance.

In order to assess the shear stress and bending moments throughout the beam, free body diagrams of both must be constructed at “cuts” made in each of the three regions of the beam: between the left support point and the left loading point, between the two loading points, and between the right loading point and the right support point. These cuts are denoted by red lines in Figure 74. The free body diagram for cut A is found in Figure 75.

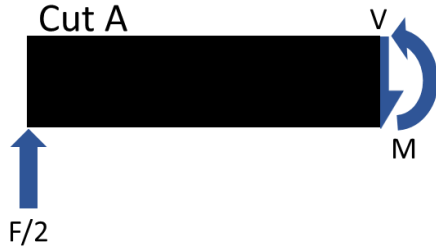


**Figure 75. Free body diagram for the leftmost region of the four point  $\frac{1}{4}$ -pt flexure specimen.**

Equations of equilibrium must now be written to determine the shear force and bending moment in this region. These equations establish the requirement for static equilibrium. In other words, all forces and moments must equal zero. They are detailed in Equations 26 and 27.

$$\sum F = 0 = \left(\frac{F}{2}\right) + V \quad (26)$$

$$\sum M = 0 = \left(\frac{F}{2}\right)x + M \quad (27)$$

From these equilibrium equations, it is found that  $V$  in this region is equal to  $-F/2$ , and  $M$  equals  $-(F/2)x$ .

The free body diagram for cut B is found in Figure 76 and its equilibrium equations in Equations 28 and 29.

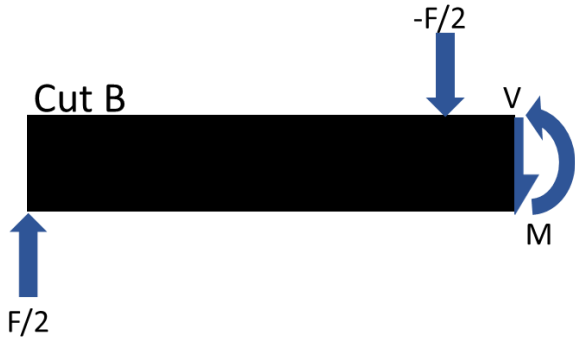


**Figure 76.** Free body diagram for the region between the two loading points.

$$\sum F = 0 = \left(\frac{F}{2}\right) + \left(-\frac{F}{2}\right) + V \quad (28)$$

$$\sum M = 0 = \left(\frac{F}{2}\right)x + \left(-\frac{F}{2}\right)\left(x - \frac{1}{4L}\right) + M \quad (29)$$

These equilibrium equations reveal that  $V$  is equal to 0 and  $M$  is equal to  $-(1/8)FL$ . The lack of shear force in the region of maximum tensile (and compressive) stress is one of the advantages of the four point flexure experiment.

The same treatment is adopted for the final region, summarized by Figure 77 and Equations 30 and 31.

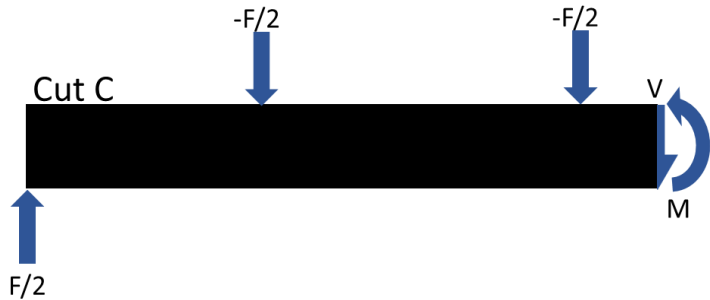


**Figure 77.** Free body diagram for the region between the rightmost loading point and support point.

$$\sum F = 0 = \left(\frac{F}{2}\right) + \left(-\frac{F}{2}\right) + \left(-\frac{F}{2}\right) + V \quad (30)$$

$$\sum M = 0 = \left(\frac{F}{2}\right)x + \left(-\frac{F}{2}\right)\left(x - \frac{L}{4}\right) + \left(-\frac{F}{2}\right)\left(x - \frac{3L}{4}\right) + M \quad (31)$$

Here,  $V$  is equal to  $F/2$ , and  $M$  is equal to  $-(F/2)(L-x)$ . From these three regions, the shear and moment diagrams can be constructed as shown in Figure 78 and Figure 79.

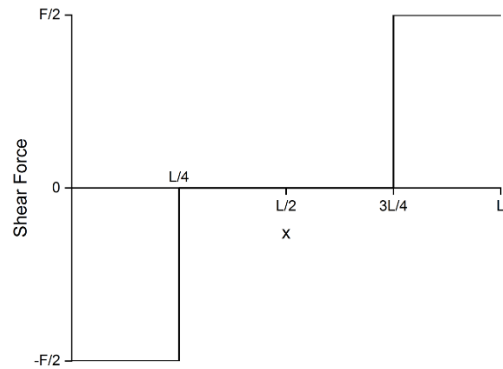


**Figure 78. Shear diagram for four point 1/4-pt flexure specimens.**

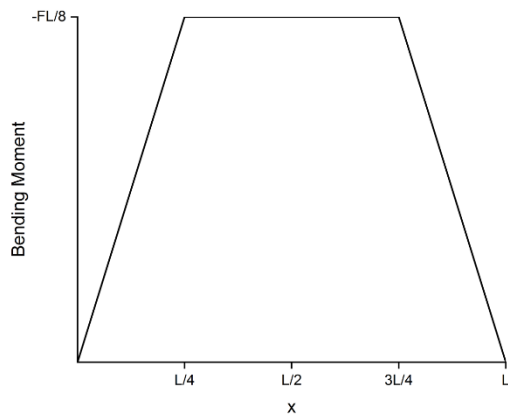


**Figure 79. Moment diagram for four point 1/4-pt flexure specimens.**

The geometry of beam bending is found in Figure 80. This figure illustrates the change in location of a point above the neutral axis (NA) as a beam is bent through an angle  $\theta$  in radians. The point's distance from the neutral axis,  $y$ , is constant, and  $\theta$  is approximated by the slope of the deflection function  $v(x)$ , i.e.  $\partial v / \partial x$ , for small  $\theta$ . This is known as the Bernoulli-Euler interpretation. Based on the geometry outlined in Figure 80,  $\tan(\theta) = -u/y$ . For small  $\theta$ ,  $\tan(\theta) = \theta$ . Therefore, Equation 32 can be written.

$$u = -y \frac{\partial v}{\partial x} \quad (32)$$

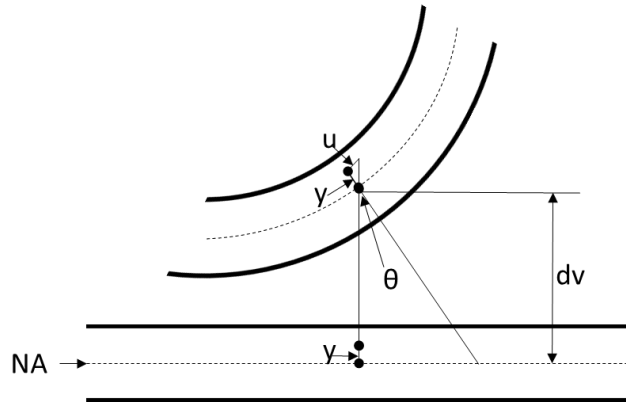


**Figure 80. Geometry of beam bending.**

Strain is defined by the gradient of the displacement of the point, i.e.  $\partial u / \partial x$ , as in Equation 33. Incorporating strain into Hooke's law yields Equation 34.

$$\varepsilon_x = \frac{\partial u}{\partial x} = -y \frac{\partial^2 v}{\partial x^2} \quad (33)$$

$$\sigma_x = E \varepsilon_x = -y E \frac{\partial^2 v}{\partial x^2} \quad (34)$$

Now consider a small area of the bar in question, with a moment operating on the left hand side which is counteracted by the moment induced by axial forces, as shown in Figure 81.

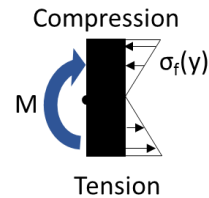


**Figure 81. Small area of a beam in flexure, showing how axial forces induced by bending balance bending moment.**

The moment induced by the axial stress  $\sigma_x(y)$  is expressed by  $M = \sigma_x \cdot y$ , where  $y$  is the distance from the neutral axis. Static equilibrium requires the sum of moments to be zero, so the equilibrium equation is found in Equation 35.

$$\sum M = 0 = M + \int_A \sigma_x(y) dA \quad (35)$$

Substituting for  $\sigma_x$  gives Equations 36 and 37.

$$M = - \int_A -y E \frac{\partial^2 v}{\partial x^2}(y) dA \quad (36)$$

$$M = E \frac{\partial^2 v}{\partial x^2} \int_A y^2 dA \quad (37)$$

The term composed of the integral of  $y^2$  with respect to area is defined as the second moment of inertia, or area moment of inertia, of the beam ( $I$ ).  $I$  is evaluated for a rectangular beam in Equations 38, 39, and 40.

$$I = \int_{-h/2}^{h/2} y^2 b dy \quad (38)$$

$$I = b \int_{-h/2}^{h/2} y^2 dy \quad (39)$$

$$I = b \left( \frac{1}{3} \left( \frac{h}{2} \right)^3 - \frac{1}{3} \left( -\frac{h}{2} \right)^3 \right) = \frac{bh^3}{12} \quad (40)$$

This area moment of inertia can now be used in further analysis. Recalling Equation 37,  $M$  can be written in terms of  $I$ ,  $E$ , and the curvature of the beam, as in Equation 41.

$$M = E \frac{\partial^2 v}{\partial x^2} I \quad (41)$$

Combining this result with Hooke's law and Equation 33, Equation 42 can be written.

$$\sigma = - \frac{y M}{I} \quad (42)$$

From previous analysis it is known that the bending moment is constant and maximum in the region between  $L/4$  and  $3L/4$ , and it equal to  $(-FL)/8$ . The plane of maximum stress in the cross section of the specimen will be furthest from the neutral axis, i.e.  $\pm (1/2)y$ . Therefore, the practical expression for maximum stress can be written as in Equation 43.

$$\sigma_{max} = \pm \frac{\left(\frac{y}{2}\right)\left(\frac{-FL}{8}\right)}{\frac{bh^3}{12}} \quad (43)$$

Simplifying yields Equation 44.

$$\sigma_{max} = \pm \frac{3FL}{4bh^2} \quad (44)$$

Note that when  $y/2$  is positive (above the neutral axis),  $\sigma_{max}$  is negative (compressive), and vice versa.

Axial strain may be calculated by incorporating into Hooke's law this stress equation and an expression for elastic modulus in terms of deflection and load. Elastic

modulus may be found by performing two integrations of a generalized form of Equation 41 and evaluating the boundary conditions. These are that the slope of the beam must be continuous at the loading point and the deflection must be zero at each support point. By this method, Equation 45 is obtained.

$$v = \frac{Fx}{6EI} (3aL - 3a^2 - x^2) \quad (45)$$

For the situation of four point ¼-pt bend, this simplifies to Equation 46.

$$v = \frac{FL^3}{96EI} \quad (46)$$

Solving for E and combining with Equation 44 in Hooke's law, an expression for strain at given loads can be written as in Equation 47.

$$\varepsilon = \frac{6vh}{L^2} \quad (47)$$

Equations 44 and 47 may be used to convert raw load and displacement data to stress and strain.

### C. Procedure for Conversion of Load/Displacement Raw Data to a Stress/Strain Curve

The strain measured during strength testing involves a few sources of error, namely erroneous crosshead displacement measurements due to i) the distance the crosshead has to travel in order for the fixtures to make contact with the specimen and ii) deformation of the fixtures and testing instrument during the experiment. To extract accurate strain values, these errors must be subtracted by a procedure known as machine compliance correction. The following procedure was employed in the present work to convert raw load and displacement (or extension) data to accurate stress and strain values.

Before a flexure experiment, the crosshead of the testing instrument is lowered so that the loading points are very close to the top surface of the specimen. However, they should not be in contact with the specimen because even slight contact will result in a small load, which would be zeroed before the procedure of the experiment. Therefore, at the beginning of the experiment, some crosshead displacement is measured without an increase in load while the fixtures travel downward to meet the specimen. This erroneous displacement manifests itself as a region of zero slope at the beginning of the load vs displacement curve. Once the load point makes contact with the specimen, the fixtures articulate slightly to settle into their final positions. This also results in some small displacement which is not truly “strain”. All of these errors in displacement are referred to as “slack” in the system. This flat region must be subtracted before transforming displacement to strain.

Further, during the experiment, the instrument applies a load to the specimen, and as such, the specimen applied an equal and opposite load to the instrument. This may elastically deform the fixtures or testing instrument as well, which manifests itself as erroneous displacement. The magnitude of this particular displacement is a function of the load being applied. This nonconstant deformation can be measured by applying a moderate load to a very large specimen which is assumed to resist all deflection and recording the load vs displacement curve which results. This curve is strictly specific to the particular instrument and fixtures used, and may not be applied to a different testing frame or set of fixtures. The procedure for machine compliance correction employed in this work can be summarized by the following steps:

1. A load of 1000 N was applied to a bar of high-purity Al<sub>2</sub>O<sub>3</sub> with dimensions 9 x 34 x 45 mm. The load vs extension curve was measured, an equation for the linear elastic region was generated by a least-squares fit, and extension was expressed as a function of the load for every data point. The x-intercept of the linear elastic region was found and subtracted from each extension value in the curve. This step is summarized by Figure 82. The linear region of the curve is described by  $y = 9572.1x - 175.3$ . Alternatively, erroneous displacement at each given load can be expressed by Equation 48.

$$x = \frac{y+175.3}{9572.1} \quad (48)$$

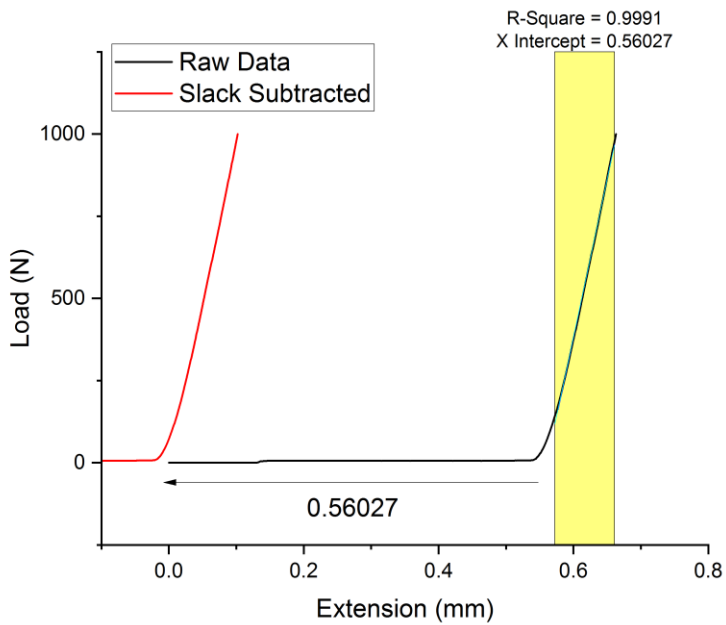


**Figure 82.** Machine compliance curve for the testing frame/fixtures combination used in this work. The yellow region is the region over which the least-squares fit was performed.

2. Linear least-squares fits were performed for the linear elastic regions of each experimental load vs displacement curve generated. The x-intercepts were determined and subtracted from their respective curves, shifting the plots to the left. Then, instrument and fixture deformation was corrected for by calculating the

displacement expected at each load using Equation 48 and subtracting it from the x value of that respective data point. This procedure is summarized by the example data in Figure 83.

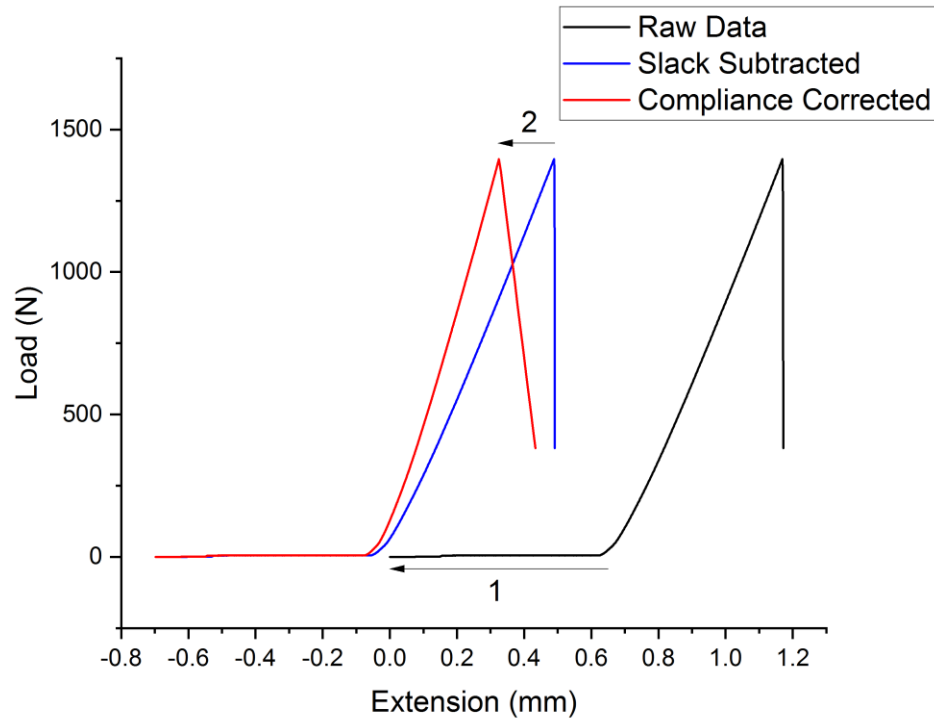


**Figure 83.** 1) Slack subtraction (2) and machine compliance correction for experimental load vs displacement data. Note that the curves begin almost at the origin after slack subtraction, and the extension at fracture decreases after correction for machine compliance.

Once machine compliance has been corrected for, raw load data may be converted to stress using Equation 44, and displacement or extension can be converted to strain using Equation 47. As per Hooke's law, the slope of the linear elastic region of the stress-strain curve is elastic modulus, E.